Oxygen transfer in cell-free and simulated alkane-based bioprocesses: Computational Fluid Dynamics (CFD) simulations and predictive modelling

by

Godfrey Kabungo Gakingo

Dissertation presented for the Degree

of

DOCTOR OF PHILOSOPHY
(CHEMICAL ENGINEERING)

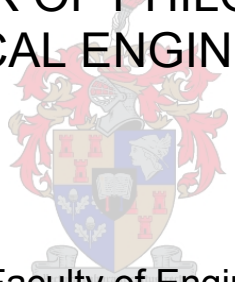

in the Faculty of Engineering
at Stellenbosch University

Supervisor

Dr. Tobias Muller Louw

Co-Supervisor

Prof. Kim Gail Clarke

December 2020

Declaration

By submitting this thesis electronically, I declare that the entirety of the work contained therein is my own, original work, that I am the sole author thereof (save to the extent explicitly otherwise stated), that reproduction and publication thereof by Stellenbosch University will not infringe any third party rights and that I have not previously in its entirety or in part submitted it for obtaining any qualification.

Date: December 2020

Abstract

Alkane activation using whole-cell biocatalysts is an attractive technology that can be employed in alkane valorisation. However, since metabolically active cells involved in this process require oxygen, a failure to effectively supply the same can limit the process. This recognition has created a need for a fundamental understanding of oxygen transfer in such systems. Additionally, there has been a need for predictive tools that can be used in bioreactor design and scale up.

This study proposes a fundamental predictive model of oxygen transfer based on Computational Fluid Dynamics that is applicable to alkane-based bioreactors. The model was built using a step-wise approach that considered an increasing number of phases – aqueous, air-aqueous, air-aqueous-alkane and air-aqueous-alkane-yeast. Model validation was also done using flow and oxygen transfer parameters. For the latter, overall volumetric mass transfer coefficients were predicted using a framework proposed to incorporate effects of the alkane phase such as possible enhancement from new mass transfer pathways and longer saturation times of the aqueous-alkane mixture.

For the aqueous and air-aqueous stirred tank reactor, model-predicted power and pumping numbers were observed to agree with established literature values. Additionally, predicted gas hold up values were accurate to within 22%. Transient variation in the mean flow (macro-instabilities) was also observed, this being a first in literature for simulations using the multiple reference frame technique. This finding implied that the latter technique can be employed in studies on macro-instabilities instead of the computationally intensive sliding mesh technique typically used.

For the air-aqueous-alkane system, it was illustrated that the alkane phase influences the hydrodynamics through turbulence modification rather than through the effective fluid properties. An increase in turbulence due to interactions by the alkane droplets led to higher turbulence viscosity values and these served to dampen the mean flow velocities. Consequently, the gas phase experienced reduced drag/dispersion and it escaped the reactor quicker as evidenced by decreasing gas hold up values with increasing alkane concentration. This trend was similar to that observed experimentally (about 30% accurate) and was consistent irrespective of boundary condition treatment of the reactor's top surface (velocity or pressure outlet boundary condition).

Oxygen transfer was investigated using two models representing possible mass transfer pathways introduced by the alkane phase – series mass transfer with and without shuttling. Minimal differences were, however, observed for these models. The mass transfer coefficients were more sensitive to changes in the gas hold up and turbulence levels. Furthermore, the predicted values were accurate to within 11% at low agitation rates and alkane concentrations. Poor predictions at other conditions suggested that the model needed improvement through, for example, the incorporation of population balance modelling.

For the air-aqueous-alkane-yeast system, the Computational Fluid Dynamics model provided a reasonable first approximation with gas hold up values predicted to within 40%. Possible mechanisms by which the yeast phase influences the hydrodynamics were highlighted. These included coalescence hindrance and the promotion of cluster formation. Oxygen transfer was poorly predicted and several factors were suggested to account for this observation. Nevertheless, further experimental investigations are required.

Opsomming

Alkaanaktivering deur heel-sel biokatalise is ’n aantreklike tegnologie wat gebruik kan word in alkaan valorisasie. Maar, siende dat die metaboliese aktiewe selle wat by die proses betrokke is, suurstof benodig, kan oneffektiewe voorsiening daarvan die proses beperk. Hierdie erkenning het ’n behoefte geskep vir ’n fundamentele verstaan van suurstofoordrag in sulke stelsels. Boonop is daar ’n behoefte vir voorspellende gereedskap wat gebruik kan word in bioreaktorontwerp en skaal vergroting.

In hierdie studie is ’n fundamentele voorspellende model van suurstofoordrag toepaslik op alkaan-gebaseerde bioreaktors ontwikkel deur berekeningsvloeidinamika te gebruik. Die model is gebou deur ’n stap-gewyse benadering wat ’n toenemende aantal fases beskou – waterig, lug-waterig, lug-waterig-alkaan en lug-waterig-alkaan-gis. Model validasie is ook gedoen deur vloei- en suurstofoordrag parameters te assesseer. Vir die laasgenoemde, was algehele volumetriese massa-oordragkoëffisiënte voorspel deur gebruik te maak van ’n raamwerk voorgestel om moontlike effekte van die alkaanfase te inkorporeer, soos verbetering deur nuwe massaoordrag meganismes en langer deurwekingstye van die waterige-alkaan mengsel.

Vir die waterige en lug-waterige stelsels het modelvoorspelde krag-en-pompsyfers ooreengestem met gevestigde literatuurwaardes. Boonop, voorgestelde gasvertragingswaardes was akkuraat tot binne 22%. Verbygaande variasie in die gemiddelde vloei (makro-onstabiliteite) is ook waargeneem, met hierdie ’n eerste in literatuur vir simulasies gebaseer op die veelvoudige verwysingsraam tegniek. Hierdie bevinding impliseer dat die laasgenoemde tegniek gebruik kan word vir toekomstige studies op makro-onstabiliteite in plaas van die berekenings intensiewe skuiwende netwerk tegniek wat gewoonlik gebruik word.

Vir die lug-waterige-alkaanstelsel, was dit gewys dat die alkaanfase die hidrodinamika deur turbulensie aanpassing eerder as deur die effektiewe vloei-eienskappe, beïnvloed. ’n Verhoging in turbulensie agv interaksies met die alkaan druppels het gelei tot groter turbulensieviskositeit waardes wat gedien het om die gemiddelde vloeisnelhede te smoor. Gevolglik het die gasfase verminderde weerstand/verspreiding ervaar en kon vinniger uit die reaktor ontsnap, soos bewys deur die verminderde gasvertragingswaardes met toenemende alkaan konsentrasie. Hierdie verloop was soortgelyk aan dit wat eksperimenteel waargeneem

is (omtrent 30% akkuraat) en was konsekwent ongeag van die grenskondisies op die reaktor se boonste oppervlakte (snelheid of drukuitlaat grenskondisie).

Suurstofoordrag was ondersoek deur twee modelle wat moontlike massaoordrag meganismes voorgestel het deur die alkaan fase – serie massaoordrag met en sonder spoeling. Minimale verskille was egter waargeneem vir die modelle. Die massaoordrag koëffisiënte was meer sensitief tot veranderinge in die gasvertragingswaardes en turbulensie vlakke. Verder, die voorspelde waardes was akkuraat binne 11% van die lae roertempos en alkaan konsentrasies. Swak voorspellings by ander toestande stel voor dat die model verbetering benodig deur, byvoorbeeld, die inkorporasie van populasie balans modelle.

Vir die lug-waterige-alkaan-gis stelsel, het die berekeningsvloeidinamika model ’n redelike eerste benadering vir die gasvertragingswaardes voorspel, binne 40%. Moontlike meganismes waardeur die gisfase die hidrodinamika kan beïnvloed is uitgelig. Hierdie sluit in samesmeltingshindernis en die vordering van groepsformasie. Suurstofoordrag was swak voorspel en verskeie faktore was voorgestel om verantwoording te doen vir die observasie. Nietemin, word verdere eksperimentele studies vereis.

Acknowledgements

Thanks be to God the Father and our Lord Jesus Christ through whom strength and endurance for this journey have been obtained.

I would like to firstly acknowledge Dr. Tobias Louw and Prof. Kim Clarke for granting me the opportunity to embark on this PhD project with them. Thank you for creating an enabling environment as well as for the constant challenge to grow and discover. Your friendship, supervision and support have been highly prized.

I would also like to acknowledge the following persons who have facilitated/brightened my stay at Stellenbosch University throughout the duration of this project:

1. The post-graduate coordinators including Mrs Lynette Bresler (now retired) and Mrs Mieke De Jager as well as all the non-academic support staff at the Department of Process Engineering.
2. My funders at the DST-NRF Centre of Excellence in Catalysis (c*change) as well as the co-ordinators of the DAAD-AIM In-Region Scholarship Programme.
3. My research colleagues including Dr. Mundike, Mr. Clyde, Mr. Ayman, Mr. Bovinille, Mr. George and Ms. Sefakor just to mention a few.
4. My fellow Kenyans at Stellenbosch including Dr. Stanley & family, Dr. Agnes, Mr. Waswa, Mr. Olepere, Ms. Simotwo and Ms. Davina just to mention a few.
5. My brothers and sisters at the Stellenbosch University Seventh-Day Adventist Student Movement including Pst. Kofo, Br. Clive, Br. Richmore, Br. Thabo, Br. Nkosi, Sis. Tendai, Sis. Thabisile and Sis. Vanessa just to mention a few.
6. My friends from all walks of life including Dr. Malusi, Dr. Munya, Mr. Chitwa, Mr. Rajah, Mr. Dinoh, Ms. Moirah just to mention a few.

Thank you all for the individual roles you have played.

Lastly, my heartfelt gratitude goes out to my family. You have been a continuous source of inspiration and refreshment throughout this journey. May God richly reward you.

List of publications

G.K. Gakingo, T.M. Louw, K.G. Clarke, Modelling of the overall volumetric mass transfer coefficient measured by the dynamic method in gas-liquid-liquid systems, in: 13th Int. Conf. Heat Transf. Fluid Mech. Thermodyn., Portoroz, 2017: pp. 662–666.

G.K. Gakingo, K.G. Clarke, T.M. Louw, A numerical investigation of the hydrodynamics and mass transfer in a three-phase gas-liquid-liquid stirred tank reactor, Biochem. Eng. J. 157 (2020). doi:10.1016/j.bej.2020.107522.

Table of contents

List of tables

List of figures

List of abbreviations

BCR	Bubble column reactor.
BND	Bubble number density model.
BSD	Bubble size distribution.
CFD	Computational Fluid Dynamics.
DNS	Direct numerical simulations.
EEE	Euler-Euler-Euler modelling approach.
LES	Large eddy simulations.
MC	Method of classes.
MI	Macro-instabilities.
MRF	Multiple reference frame technique.
MUSIG	Multiple size group method.
OTR	Oxygen transfer rate.
PBM	Population balance model.
PC-SIMPLE	Phase-coupled semi-implicit method for pressure-linked equations.
PH-EE	Pseudo-homogenous Euler-Euler modelling approach.
QMOM	Quadrature method of moments.
RANS	Reynolds-averaged Navier-Stokes equations.
RSM	Reynolds stress model.
SIMPLE	Semi-implicit method for pressure-linked equations.
STR	Stirred tank reactor.
SM	Sliding mesh technique.
TKE	Turbulent kinetic energy.

List of symbols

a	Interfacial area per unit volume (m^2/m^3).
d_{32}	Sauter mean diameter (m).
d_i	Diameter of phase i (m).
$\bar{g}$	Gravitational acceleration vector (m/s^2).
h	Thickness of interfacial film/concentration boundary layer in aqueous phase. Axial extent of impeller (m).
k_i	Turbulent kinetic energy in phase i (m^2/s^2).
k_{jw}	Covariance of fluctuating velocities (between aqueous phase and phase j).
m	ratio of oxygen adsorbed on solid particle (or dissolved in alkane phase) to that dissolved in aqueous phase at equilibrium.
p_o	Partial pressure of oxygen in gas phase (Pa).
r	Radial extent of impeller (m).
s	Fractional rate of surface renewal in Danckwert's theory.
t_e	Surface exposure time of fluid elements in Higbie's theory (s).
v_s	Superficial gas velocity (m/s).
x	Volume fraction of solid (or alkane) phase based on total volume of un-gassed reactor.
y_g^o	Mole fraction of oxygen in gas phase.
C_D	Drag coefficient.
$C_{D,\infty}$	Drag coefficient in stagnant liquid.
C_j^i	Interfacial oxygen concentration in phase j (mol/m^3).
C_j	Dissolved oxygen concentration in phase j (mol/m^3).
C_j^*	Dissolved oxygen saturation concentration in phase j (mol/m^3).
D	Oxygen's diffusivity in the liquid phase (m^2/s).
D_r	Ratio of oxygen's diffusivity in alkane phase to that in aqueous phase.
D_{imp}	Impeller diameter (m).
$\bar{\bar{D}}_{jw}$	Fluid-particle dispersion tensor.
E, E'	Enhancement factor.
$\bar{F}_i$	Force vector (N).

$G_{k,w}$	Production term associated with velocity gradients of aqueous phase in turbulence model.
H	Henry's constant (Pa m^3/kmol).
$\bar{\bar{I}}$	Identity tensor.
$\bar{J}_i$	Total diffusive flux of oxygen in phase i.
K_{ji}	Interfacial exchange coefficient (between phases i and j).
$K_L a'$	Overall volumetric mass transfer coefficient in the presence of a 2nd liquid phase (such as the alkane phase) (s^{-1}).
$K_L a_{\alpha_o=0}$	Overall volumetric mass transfer coefficient in the absence of a 2nd liquid phase (such as the alkane phase) (s^{-1}).
K_L	Overall mass transfer coefficient (m/s).
M	Torque on impeller blades (N m).
N	Impeller speed (rps).
N_P	Power number.
N_q	Pumping number.
P_T	Total pressure of gas phase (Pa).
P	Power (W).
P_g	Gassed power (W).
Re	Reynolds number.
$\bar{R}_{ji}$	Interphase interaction force vector (N).
S	Spreading coefficient (N/m).
V	Volume (m^3).
$\overline{V}$	Velocity vector (m/s).
$\overline{V}_{slip}$	Slip velocity vector (m/s).
$\overline{V}_{dr}$	Drift velocity vector (m/s).
α_i	Volume fraction of phase i based on total volume in a gassed reactor.
ϵ_i	Turbulent kinetic energy dissipation rate in phase i (m^2/s^3).
ρ_i	Density of phase i (kg/m^3).
σ_{ij}	Interfacial tension between phases i and j (N/m).
$\bar{\bar{\tau}}$	Stress tensor (Pa).
τ_p, τ_{jw}^F	Particle's relaxation time (s).
τ_L	Integral timescale of turbulence (s).

τ_{jw}^{t}	Eddy-particle interaction time (s).
μ_i	Dynamic viscosity of phase i (Pa s).
$\mu_{t,i}$	Turbulent viscosity of phase i (Pa s).
υ_i	Kinematic viscosity of phase i (m^2/s).
Ω	Cells' concentration (g/L dry weight).
Π_{k_w}	Production term associated with dispersed phases in turbulence model.
Π_{ϵ_w}	Dissipation time-scale of turbulence energy produced by dispersed phases.
$\beta, \delta, \zeta, \xi, \varphi, \eta, \gamma$	Exponents.
Γ, Λ, ψ	Constants (general).
$C_\mu, C_{1\epsilon}, C_{2\epsilon}, C_{3\epsilon}$ $C_{AM}, \sigma_k, \sigma_\epsilon$	Constants of the turbulence model.

Subscripts/superscripts

o	Alkane phase.
w	Aqueous phase.
g	Gas phase.
i, j	Phases i, j.
ave	Average.
cap	Spherical cap.
eff	Effective.
ell	Ellipse.
rad	Radial.
sph	Spherical.

1.0 Introduction

1.1 Background

Alkanes are a part of the hydrocarbon feedstock derived from fossil fuels by industrial processes such as crude oil distillation and both gas- and solid-to-liquid fuel conversion. They are relatively inert in comparison to other derived hydrocarbon fractions and have as such been traditionally exploited for their fuel value [1]. However, greater value can be unlocked from these resources by exploring alkane valorisation processes to generate platform products such as alcohols that can be used as solvents, preservatives or reagents [1–3]. This potential has created impetus for research into alkane valorisation with the aim of introducing greater efficiency into the alkane value chain [1]. Such research has also been underpinned by the current and projected availability of alkane feedstock [1] given the place of fossil fuels and their derivatives in the world's economy for the foreseeable future [4]. This is particularly relevant within the context of South Africa where alkanes are a by-product of coal-to-fuel conversion technologies [5,6].

Alkane activation or functionalisation is a valorisation process that involves the introduction of oxygen or other functional groups into an inert alkane backbone to generate products such as alcohols [1,7]. To accomplish this, both chemical and biological routes have been explored [1,3,7]. The former entails the activation of alkane in a reactor while using metallic compounds to catalyse the process. It is often done at elevated conditions such as temperature ranges of 200 – 800 °C [1,3] so as to provide the necessary dissociation energy for the bonds in the alkane structure [3]. The biological route or biocatalysis, on the other hand, entails the activation of alkane while using catalytic enzymes. This process, unlike the former, is normally done at mild conditions (ambient temperatures and pressures) [3,7].

Biocatalysis has been viewed as the more attractive route to alkane activation due to a number of reasons. Firstly, biocatalysis is conducted at mild conditions thus demanding less energy in comparison to chemical catalysis [1,3,7]. Secondly, biocatalysis has been observed to exhibit greater selectivity, with selectivity defined as the ratio of the quantity of targeted products to the total quantity of products [3]. Finally, biocatalysis has been recognised for its versatility – a large number of organisms have been discovered that are able to assimilate a diverse pool of alkanes as substrate [3].

Biocatalysis, as previously mentioned, is achieved through the use of catalytic enzymes such as oxygenases. These enzymes can be used either in isolated form or in whole cells/organisms [3,7]. The use of whole cells has, however, been more readily adopted as it provides a stable environment for the enzymatic reaction among other reasons [3,7]. Consequently, biocatalysis setups are usually characterised as multiphasic systems whereby cells growing in an aqueous growth medium consume an (immiscible) alkane substrate to produce the desired products. As this multiphasic system is different from that obtained when chemical catalysis is employed, appropriate reactor design is required. To this end, both biocatalytic and process concerns have been identified that need to be addressed [7,8].

Biocatalytic concerns stem from the fact that native/wild-type organisms are adapted to survive in their natural environment as opposed to meeting industrial requirements [1,7]. Consequently, issues such as the biocatalysts' ability to sustain high throughputs as well as side-reactions leading to product degradation have arisen [3,7]. Such issues form the focus of ongoing research in enzyme/protein engineering [3,7].

Process concerns, on the other hand, stem from the need to address issues such as mass transfer limitations in bioreactor design [3,7,8]. Mass transfer limitations touch on the provision of both the alkane substrate [8] and oxygen [9] to the cells given that both of these have low solubility in the aqueous growth medium where cells are normally located. In the case of the alkane substrate, however, low solubility is not necessarily a disadvantage as additional mechanisms of substrate uptake by cells have been hypothesised in literature. These include the pseudo-solubilisation of the substrate by extracellular surfactants and the modification of the hydrophobicity of the cell membrane to permit for binding and uptake of substrate droplets [10,11]. It has been further suggested that substrate transport across the cell membrane is the greater bottleneck in comparison to low substrate solubility [12].

With regards to oxygen, its low solubility in the aqueous growth medium at mild conditions (ambient pressure and temperature) [13] presents a challenge as oxygen is necessary for cell growth. In addition, oxygen is required for the activation process by the oxygenase enzymes [7,8]. Thus, alkane activation processes using whole-cell biocatalysts need to be optimally designed lest they run the risk of becoming limited by oxygen transport rather than by intrinsic kinetics [9]. This realisation has informed the need for a fundamental understanding of the factors that impact oxygen transfer in such systems. Such an understanding would then lead to predictive models of oxygen transfer that can be used in the design and scale-up of

bioreactors given the expectation that oxygen transfer limitations scale with increasing reactor size [9].

To address the above need, experimental investigations have been conducted on simplified alkane activation processes seeking to link the behavioural trends of the oxygen transfer rate (OTR) to process conditions (agitation and aeration rates, alkane and cell concentrations). The OTR, characterised by the overall volumetric mass transfer coefficient ($K_L a'$), has been investigated in both cell-free systems [14,15] and those with non-viable cells (or simulated systems) [16]. Moreover, both empirical [17–19] and theoretical [20] models have been proposed, with the latter preferred for predictive purposes as they are of a more fundamental nature.

In seeking to bring the design process full circle, theoretical models can be coupled with simulation tools such as Computational Fluid Dynamics (CFD). Such a CFD-based approach to predicting oxygen transfer in alkane-based systems would offer several advantages. Firstly, CFD as a tool has been shown to be capable of providing good approximations to complex hydrodynamics in multiphase turbulent systems [21]. It is thus particularly suited to model alkane-based bioreactors wherein the hydrodynamics are expected to play an important role in determining the oxygen transfer [9]. Secondly, CFD provides spatially resolved data and thus gives a closer representation of the heterogeneous conditions within a reactor as compared to empirical models that rely on volume-averaged variables [21]. Finally, CFD can be incorporated into bioreactor design at any scale given that it is a scale-independent tool. This would allow for the rapid yet rational evaluation of new bioreactor concepts *in silico*.

The successful application of the CFD-based approach in the prediction of oxygen transfer in 2-phase gas-liquid (air-aqueous) systems has been reported in literature [22–24]. What is lacking, however, is a systematic investigation of the application of this approach to alkane-based bioreactors. This study addresses this gap by systematically developing and validating a predictive model of oxygen transfer based on CFD that is applicable to both 3-phase (cell-free) and 4-phase alkane-based bioprocesses.

1.2 Aim and objectives

The aim of this study was threefold. First was to identify the dominant mechanisms affecting the hydrodynamics and oxygen transfer in an alkane-based bioprocess. Thereafter, a CFD model of the system was to be developed and coupled to identified fundamental models of the overall volumetric mass transfer coefficient in order to predict oxygen transfer. Finally, the developed model was to be validated against existing experimental data.

To achieve the stated aim, the following objectives were proposed;

1. To identify fundamental models for $K_L a'$ applicable to alkane-based bioprocesses and that can be coupled to CFD output.
2. To set up a CFD model of a single phase stirred tank reactor and validate it based on relevant hydrodynamic parameters.
3. To extend the model above to 2 phases (gas-liquid) and validate it based on relevant hydrodynamic and mass transfer parameters.
4. To further extend the model above to 3 phases (gas-liquid-liquid) and investigate the effects of introducing the alkane phase on the hydrodynamics of the system.
5. To predict oxygen transfer in the 3-phase cell-free system by coupling identified models for $K_L a'$ to the CFD output.
6. To validate the CFD-based approach to predicting oxygen transfer against experimental data.
7. To extend the CFD model developed above to the 4-phase (gas-liquid-liquid-solid) system and investigate the effects of introducing the yeast phase on the hydrodynamics of the system.
8. To predict oxygen transfer in the 4-phase system by coupling identified models for $K_L a'$ to the CFD output.
9. To validate the CFD-based approach to predicting oxygen transfer against experimental data.

1.3 Scope

This study has been performed as part of an ongoing project on alkane biocatalysis; the project having been spurred by a need to add value to alkane feedstock available from coal-to-fuel conversion processes [5,6]. Previous work focused on providing experimental measurements of the oxygen transfer rate [14,16,25] whereas this study has focussed on the modelling aspects of the project. Given the need to validate the developed models, secondary data has been employed while cognisant of the potential limitations in various experimental methodologies. As and where necessary, the discussion presented in later chapters alludes to this.

Further limitations arising from the use of secondary data included the following:

1. Given that the focus of the project has been on oxygen transfer in 3-phase and 4-phase systems, there was a lack of experimental hydrodynamic (velocity) data to validate the simulations. To address this, validation in the single phase and 2-phase systems was done based on established hydrodynamic parameters in literature such as the power number [26] and pumping number [26,27]. Changes in these parameters were studied for the 3-phase and 4-phase systems.
2. Given that experimental data was only available for a laboratory-scale stirred tank reactor, the efficacy of the CFD model was not investigated at larger scales (pilot and industrial). This notwithstanding, CFD is a scale-independent tool [21] and the methodology developed herein can be extended to larger scales.

In terms of the model development, the CFD model was based on an Eulerian description of the simulated phases which involved treating these phases as interpenetrating continua with momentum exchange across them [24]. To keep the model tractable given the available computational resources, a number of limitations were imposed. Some of the significant limitations are listed below, with a more elaborate discussion on the same presented in Chapter 4.0.

1. Turbulence was modelled on the basis of the Reynolds-averaged Navier-Stokes equations (RANS). The Boussinesq's hypothesis was employed to approximate the Reynolds' stresses in terms of the mean velocity gradients, with the arising turbulent viscosity defined in terms of the turbulent kinetic energy (k) and the energy dissipation

rate (ϵ). In addition, it was assumed that the continuous phase dominated the turbulence according to the dispersed k–ϵ model with the influence of the dispersed phases accounted for using Tchen's theory on the dispersion of particles in turbulent flows [28–31].

2. The multiple reference frame (MRF) technique was employed to resolve the impeller-baffle interaction in the simulation of the stirred tank reactor considered. This technique has been shown to have comparable accuracy to the more involving sliding mesh technique [32].
3. Constant particle sizes were specified for the dispersed phases (air and alkane) rather than model their size distributions using a population balance model (PBM). This simplification, though in line with practice in literature [33], was supported by the observation that coalescence and breakage kernels (terms) in PBMs have been investigated for 2-phase systems (gas-liquid or liquid-liquid) [34] with little work done for 3-phase systems. Furthermore, it was expected that the assumption of constant particle sizes would be accurate in the 4-phase system due to the non-coalescing effect of the cells/micro-organisms employed.
4. In the specification of interphase interaction forces, only the drag force was considered despite the presence of other forces such as the virtual mass force and the lift force. This was based on previous research showing the drag force to be the most significant force in the bulk of a stirred tank reactor [33,35,36].

1.4 Significance

Alkane activation via whole-cell biocatalysts is an attractive route to alkane valorisation. However, the adoption of this bioprocess in industry requires that various concerns be addressed before the optimal use of this process. One such concern touches on the need to provide adequate amounts of oxygen since oxygen is necessary for both cell growth and the activation process. This underscores the need for a fundamental understanding of the factors that impact oxygen transfer in such alkane-based systems. Moreover, predictive models of oxygen transfer are needed that can be used in bioreactor design at any scale given the expectation that oxygen transfer limitations scale with increasing reactor size.

In an attempt to address this gap, previous work has focused on experimental investigations of the oxygen transfer rate in simplified systems, that is, in cell-free systems and those with non-viable cells (simulated bioprocesses). In addition, empirical and theoretical models have been

proposed in literature. This work seeks to bring the design process full circle by proposing a CFD-based approach to modelling oxygen transfer in such systems. Specifically, the novelty of this work may be enumerated as:

1. The proposal of a theoretical framework for modelling the overall volumetric mass transfer coefficient in alkane activation bioprocesses based on CFD output.
2. The identification and investigation of key changes introduced by the additional phases (alkane and yeast) on the hydrodynamics and oxygen transfer in the systems considered.
3. The incorporation of the above changes into the development of a CFD model applicable to the 3-phase and the 4-phase alkane-based systems.
4. The prediction of gas hold up and validation of the same in the 3-phase gas-liquid-liquid system.
5. The prediction of the overall volumetric mass transfer coefficient and validation of the same in the 3-phase gas-liquid-liquid system.
6. The prediction of gas hold up and validation of the same in the 4-phase gas-liquid-liquid-solid system.
7. The prediction of the overall volumetric mass transfer coefficient and validation of the same in the 4-phase gas-liquid-liquid-solid system.

Though the case studies considered in this work emerged from the field of alkane biocatalysis, the findings reported are nevertheless relevant to a wider context. They can be applied to analogous multiphase bioprocesses such as fermentation with the organic phase simply added as an oxygen carrier (or reservoir) and the biological gas stripping of volatile organic compounds.

1.5 Thesis overview

Chapter 1.0 has introduced the alkane activation process illustrating its relevance to industry based on the variety of high value products that can be obtained. It has been further illustrated that the biological route, or biocatalysis, has been more readily adopted though several concerns need to be addressed. In particular, oxygen transport has been singled out as a potentially limiting factor that needs to be studied at a fundamental level. It has been shown how this work intends to contribute to the existing body of knowledge by proposing the use of Computational Fluid Dynamics in the predictive modelling of oxygen transfer in alkane activation bioprocesses.

Chapter 2.0 presents the literature review. It begins with an introduction to mass transfer in 2-phase gas-liquid systems, with consideration given to the modelling approaches employed in such systems. Consideration is also given to cases of gas-liquid mass transfer in the presence of a solid phase as well as the use of the CFD methodology in predictive studies. Thereafter, mass transfer in 3-phase alkane-based systems is introduced. A review of previous experimental and modelling efforts has been presented. Furthermore, current gaps in the modelling of mass transfer in such systems have been highlighted.

Chapter 3.0 addresses the one of the gaps identified in Chapter 2.0 by proposing a modelling framework for the overall mass transfer coefficient in alkane-based systems. This sets the scene for the CFD-based modelling whereas Chapter 4.0 presents the actual development of the CFD model. Various aspects of the model development process have been discussed such as the generation and meshing of the domain, the specification of model equations plus their numerical implementation.

Chapters 5.0 – 7.0 present the results of the modelling investigations. Chapter 5.0 focuses on the validation of the CFD model based on single phase and 2-phase (gas-liquid) results. Chapters 6.0 and 7.0, on the other hand, focus on the 3-phase (gas-liquid-liquid) and the 4-phase (gas-liquid-liquid-solid) results respectively. In these chapters, a discussion of both the hydrodynamics and oxygen transfer has been presented.

Chapter 8.0 concludes this study by presenting a summary of the key findings that have emerged from the research. In addition, recommendations for future work have been given.

2.0 Literature review

This chapter begins with an overview of mass transfer in 2-phase gas-liquid systems with the focus being on its modelling, both empirically and theoretically. Also considered are the cases of gas-liquid mass transfer in the presence of a solid phase and the use of Computational Fluid Dynamics (CFD). Thereafter, an overview of mass transfer in alkane-based systems is given in which current gaps in modelling are highlighted.

2.1 Gas-liquid mass transfer

Gas-liquid systems in bioprocess setups can be typically characterised as air-aqueous systems in which an aqueous phase consisting of a solution of salts provides a growth medium to aerobic cells/organisms [37]. Dissolved oxygen in the aqueous phase is utilised by the cells for their metabolic functions while being replenished through mass transfer from sparged air. To quantify the oxygen transfer rate (OTR) from air, a two-film resistance model is usually employed [13] as given by equations (2.1) and (2.2).

$$\text{OTR} = \frac{dC_w}{dt} = K_L a_{\alpha_o=0}(C_w^* - C_w) \tag{2.1}$$

$$p_o = P_T y_g^o = \text{H}C_w^* \tag{2.2}$$

In the above equations, C_w represents the dissolved oxygen concentration in the aqueous phase (denoted by subscript w) whereas C_w^* represents the dissolved oxygen saturation concentration (oxygen's solubility). The difference, $(C_w^* - C_w)$, represents the driving force behind oxygen transfer from the gas to the aqueous phase. This concentration driving force largely depends on oxygen's solubility in the aqueous phase which is itself a function of the oxygen's partial pressure (p_o) and the Henry's constant (H) as shown in equation (2.2) [13]. Changes to the partial pressure can occur as a result of changes in the mole fraction of oxygen in the gas phase (y_g^o) or as a result of local differences in the total pressure (P_T) as experienced within tall (industrial-scale) bioreactors [38]. To account for such changes, the gas phase dynamics are usually approximated based on assumptions such as plug flow or perfectly mixed gas phase [39]. The latter assumption is often used for laboratory-scale

bioreactors in which the solubility is defined based on the partial pressure of oxygen at the bioreactor's outlet [40].

In equation (2.1), $K_L a_{\alpha_o=0}$ represents the overall volumetric mass transfer coefficient with the subscript $\alpha_o = 0$ used to emphasise that the volume fraction of the alkane phase (α_o) is zero. The latter is a measure of interfacial resistance to oxygen transfer and a key parameter in bioreactor design and scale-up [9,37]. It is a product of the overall mass transfer coefficient (K_L) and the gas-liquid interfacial area per unit volume (a) or interfacial area in short. The overall mass transfer coefficient (K_L) considers the resistance to oxygen transfer from both the gas' and the liquid's interfacial boundary layers (see Figure 2.1).

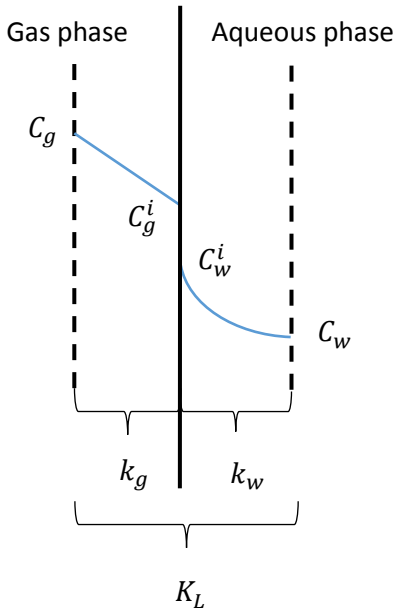

Figure 2.1: Gas-liquid concentration boundary layer illustrating bulk (C_g, C_w) and interfacial (C_g^i, C_w^i) oxygen concentrations as well as the individual (k_g, k_w) and overall (K_L) mass transfer coefficients.

2.1.1 Measurement of the overall volumetric mass transfer coefficient

Various experimental methods have been proposed for the determination of $K_L a_{\alpha_o=0}$ [37]. These include the dynamic gassing-out method [41] and the pressure step method [42] among others. The dynamic gassing-out method is commonly employed and it involves the measurement of the dissolved oxygen tension in the aqueous phase following a step change in the partial pressure of oxygen at the gas inlet while keeping the agitation and aeration rates constant [37,43]. The measurements, reported as concentration profiles, are then fitted to

models such as equation (2.1) from which $K_L a_{\alpha_o=0}$ values can be determined. Accuracy can be enhanced by considering the response time of the measurement probes and this leads to second order models from which $K_L a_{\alpha_o=0}$ is calculated by iteration [37,43].

In seeking to resolve the trends in the individual components of $K_L a_{\alpha_o=0}$, the concurrent measurement of $K_L a_{\alpha_o=0}$ and the interfacial area (a) has been proposed. Both direct and indirect methods have been proposed for the measurement of the latter [44,45]. Direct measurement of the interfacial area has been through methods such as the light attenuation technique illustrated by Calderbank (cited in [46]). On the other hand, indirect methods have involved the inference of the interfacial area from measurements of the gas hold up (α_g) and the bubble size distribution (BSD). The gas hold up has been obtained through methods such as the dispersion height technique [14] whereas the BSD has been obtained through methods such as capillary suction [47] or high-speed photography coupled with image analysis [14,48]. Appropriate equations, such as equation (2.3), have then been used to relate the interfacial area to the gas hold up and moments of the BSD such as the Sauter mean diameter (d_{32}).

$$a = \frac{6\alpha_g}{d_{32}} \tag{2.3}$$

2.1.2 Empirical models

The overall volumetric mass transfer coefficient ($K_L a_{\alpha_o=0}$) has been traditionally reported as a composite parameter. This has informed its modelling, with empirical models such as those in equation (2.4) for stirred tank reactors (STR) [49] and equation (2.5) for bubble column reactors (BCR) [9] having been proposed. Such models correlate changes in $K_L a_{\alpha_o=0}$ to changes in the power input into the system. The latter can be by either mechanical means as characterised by the power input per unit volume (P_g/V) or pneumatic means as characterised by the superficial gas velocity of the sparged gas (v_s). Changes in $K_L a_{\alpha_o=0}$ have also been correlated to factors such as the fluid properties [37,49], with differences in the systems investigated being captured through an adjustment of the constant Γ and the exponents β and δ.

$$K_L a_{\alpha_o=0} = \Gamma \cdot \left(\frac{P_g}{V}\right)^{\beta} {v_s}^{\delta} \tag{2.4}$$

$$K_L a_{\alpha_o=0} = \Gamma \cdot {v_s}^{\delta} \tag{2.5}$$

Where $K_L a_{\alpha_o=0}$ and the interfacial area have been measured concurrently, empirical correlations for the latter have been proposed as shown in equations (2.6) and (2.7) for STRs and BCRs respectively [9,50,51]. These have taken a structure similar to that of equations (2.4) and (2.5). Such equations correlate the changes in the interfacial area to measures of the power input into the system. However, other factors such as the fluid properties and the gas hold up have also been considered [52].

$$a \propto \frac{P_g}{V}, v_s \tag{2.6}$$

$$a \propto v_s \tag{2.7}$$

Empirical models, such as those highlighted above, are useful as a starting point for bioreactor design. However, the presence of constants and exponents that need to be tuned to suit the system under consideration suggests a limitation in the description of the relevant mass transfer mechanisms. Consequently, there has been a need for models of a more fundamental nature. This need has paved the way for theoretical models and these are further discussed in the next section.

2.1.3 Theoretical models

Theoretical models entail a separate treatment of the individual components of $K_L a_{\alpha_o=0}$. They relate the changes in both K_L and the interfacial area to the prevailing hydrodynamic conditions at the mass transfer interface. Considering the case of the interfacial area, the maximum stable bubble size in the presence of liquid flow has been related to the ratio of disruptive forces (inertia) to resistive forces (surface tension) [53]. Taking this a step further, BSDs have been modelled using population balance equations that take into account bubble-bubble coalescence and bubble break up phenomena [34]. Such a knowledge of the bubble sizes has then been used to compute the residence times of bubbles in reactors (or conversely

their rise velocities) [54] thus giving an estimation of the gas hold up and the interfacial area (refer to equation 2.3).

With regards to the overall mass transfer coefficient (K_L), several theories have been proposed for its prediction such as the film and penetration theories. Whitman (cited in [55]), in proposing the film theory, assumed that thin films containing stagnant fluid exist on either side of the mass transfer interface (see Figure 2.1). Furthermore, he assumed that mass transfer across these films occurs by steady state molecular diffusion [55,56]. Consequently, he obtained an equation for K_L as a function of oxygen's diffusivity in the aqueous phase (D) and the thickness of the liquid's interfacial film (h) as illustrated by equation (2.8).

$$K_L = D/h \tag{2.8}$$

The film theory has found use in systems where the time taken to establish concentration gradients is far smaller than the time available for mass transfer [55]. However, it does not provide an accurate description of mass transfer in agitated reactors due to the presence of turbulence. Consequently, other theories have been proposed such as the penetration theories. The term "penetration theories" is, in this case, used as a generic term to refer to Higbie's penetration theory and its later modification by Danckwerts that yielded the surface renewal theory [57].

Higbie, in his theory, assumed that fluid elements are brought from the bulk fluid to the interface by turbulent eddies. The fluid elements then remain at the interface for a fixed period of time during which mass transfer occurs by unsteady state molecular diffusion [56]. Thereafter, the fluid elements are removed by eddies and are returned to or mixed with the bulk fluid [55]. The resulting equation related K_L to oxygen's diffusivity raised to an exponent of 1/2 as illustrated in equation (2.9), with t_e being the constant surface exposure time for fluid elements. As a modification to this, Danckwerts proposed that fluid elements near the interface would be renewed randomly independent of their age, that is, they would have a random exposure time [55]. This resulted in equation (2.10) with s being the fractional rate of surface renewal [55,56].

$$K_L = 2\sqrt{D/\pi t_e} \tag{2.9}$$

$$K_L = \sqrt{Ds} \tag{2.10}$$

The penetration theories, similar to the film theory, contain parameters that need to be approximated [56]. These include the thickness of the liquid's interfacial film (h), the exposure time (t_e) and fractional rate of surface renewal (s). Several approaches have been proposed to model these parameters. One such approach is the use of Kolmogoroff's theory of isotropic turbulence to relate these unknown parameters to measures of turbulence [52]. As an example, the exposure time in Higbie's penetration theory has been expanded in terms of the characteristic time of small-scale turbulent eddies thus resulting in equation (2.11) [52]. In this equation, υ represents the kinematic viscosity for a Newtonian fluid whereas ϵ represents the turbulent energy dissipation rate. The constant Λ, on the other hand, represents a value of $2/\sqrt{\pi}$.

$$K_L = \Lambda \cdot \sqrt{D}\left(\frac{\epsilon}{\upsilon}\right)^{1/4} \tag{2.11}$$

The structure of equation (2.11) has also been obtained from different modelling considerations. For example, it has been proposed that the exposure time can be considered as the average time between "periodic replacement of a viscous sublayer" at the interface [58]. A value of $\Lambda = 0.301$ was obtained for Newtonian fluids. Similarly, a value of $\Lambda = 0.4$ has been obtained for an eddy cell model based on Danckwerts' surface renewal theory [59]. In this model, it was assumed that mass transfer would be governed by small and inertial scales of turbulence [59].

Besides these considerations of turbulence, the exposure time in equation (2.9) has also been defined in terms of the time taken by a bubble to rise through a distance equivalent to its diameter [58]. Equation (2.12) was obtained with d_g representing the bubble's diameter and $\overline{V}_{slip}$ the bubble's slip velocity. This equation has been typically applied to large bubbles (d_g > 2.5 mm) thus necessitating an extra model, such as that based on the boundary layer theory (see equation (2.13)), to describe the mass transfer of small bubbles (d_g < 1 mm) [60–62]. Linek et al. [60,63] have, however, argued that this differentiation of mass transfer

characteristics according to bubble size is erroneous and arises due to the use of inappropriate experimental techniques to measure $K_L a_{\alpha_o=0}$ in reactors characterised by a high level of turbulence (STRs). They have observed that an increase in the turbulence levels results in an increase in the mass transfer rate for both large and small bubbles. Consequently, they have suggested that equation (2.11) be applied to STRs with the value of the constant Λ being set to 0.523 [63].

$$K_L = \frac{2}{\sqrt{\pi}}\sqrt{D}\left(\frac{|\overline{\mathrm{V}}_{slip}|}{d_g}\right)^{1/2} \tag{2.12}$$

$$K_L = 0.6\left(\frac{|\overline{\mathrm{V}}_{slip}|}{d_g}\right)^{1/2} D^{2/3}\upsilon^{-1/6} \tag{2.13}$$

With the theoretical models in the form of equations (2.11) – (2.13), values such as the slip velocities and turbulent energy dissipation rates still need to be specified. These can be derived in an averaged sense from the operating conditions as has been done by Garcia-Ochoa & Gomez [64]. However, this introduces a degree of empiricism thus making the models semi-theoretical. An alternative route would be to specify such values based on the output of a CFD model. This proposition is further reviewed in section 2.3.

2.2 Gas-liquid mass transfer in the presence of a solid phase

In gas-liquid systems, a solid phase is often present with its nature depending on the system under consideration. As an example, cells/organisms are present in bioprocesses whereas (solid-supported) catalysts are present in chemical processes. The presence of the solid phase or particle does impact mass transfer. However, the direction (increase or decrease in $K_L a_{\alpha_o=0}$) and magnitude of impact largely depends on the characteristics of the solid phase. Such characteristics include the solid type (biological, non-biological), geometry, solid loading, physical properties as well as surface properties. Process conditions as well as the properties of the liquid phase have also been observed to moderate the impact of the solid phase [65–67]. Consequently, varying and often contradicting results have been reported in literature.

2.2.1 Mass transfer mechanisms in the presence of a solid phase

Focussing on the effects of inactive solids, it has been proposed that gas-liquid mass transfer in the presence of a solid phase can be enhanced by a shuttling mechanism (see Figure 2.2) [68,69]. The latter involves the movement of the solid phase into and out of the liquid's interfacial film while adsorbing the solute gas in the film and releasing it into the bulk liquid [68,69]. This mechanism requires that the solid phase be of a size smaller than the liquid's interfacial film thickness in addition to having a high adsorption capacity for the solute gas [65,68]. However, this mechanism has been contested based on observations of mass transfer enhancement by particles with no affinity for the solute gas and of a size larger than the interfacial film thickness [70,71].

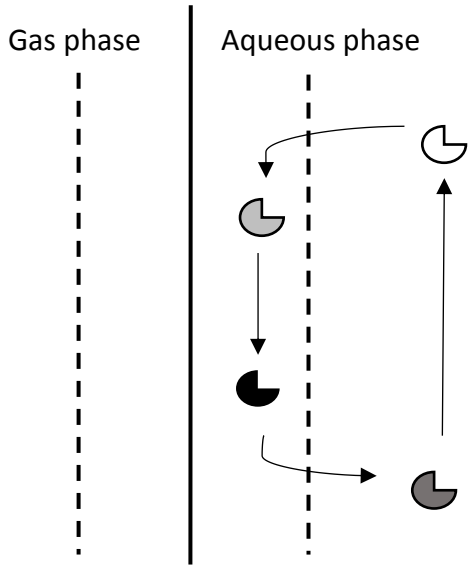

Figure 2.2: Gas-liquid concentration boundary layer illustrating shuttle mechanism. Cut circle represents the solid phase with the increasing degree of shading illustrating an increasing amount of solute gas adsorbed.

Kluytmans et al. [66] and Ruthiya et al. [65] have suggested that a solid phase can affect mass transfer through hydrodynamic effects. The latter can be through the collision of particles with the interfacial film (refer to film theory) or the enhancement of the degree of interfacial turbulence (refer to penetration theories) [65,66]. It has been suggested that such mechanisms lead to mass transfer enhancement at low agitation rates [66] and for particles with high inertia (density, size) [72]. Furthermore, it has been suggested that such mechanisms are only effective at low solid loadings since at high solid loadings a reduction in $K_L a_{\alpha_o=0}$ has been

observed [72,73]. The latter has been hypothesised to be due to an increase in the effective viscosity which reduces the interfacial turbulence thus reducing K_L [65].

With regards to bubble-bubble interactions, it has been observed that a solid phase can either promote or hinder coalescence [65]. This is largely influenced by the surface properties of the solid phase and affects the interfacial area available for mass transfer (see equation (2.5)). It has been observed that non-wettable (hydrophobic) particles accumulate at the gas-liquid interface and can inhibit coalescence. This can be through the formation of a steric (mechanical) barrier at the bubble surface or a bridging monolayer [74]. However, if the particles are highly hydrophobic, they can destabilise the thin liquid film between bubbles thus leading to its rupture and in this way promote coalescence [75]. The latter has been postulated to explain an observed decrease in gas hold up (hence $K_L a_{\alpha_o=0}$) on addition of non-wettable solids [76,77].

With regards to particle-bubble interactions, it has been suggested that the solid phase can affect mass transfer through physical blocking [65]. This has been hypothesised to be through a reduction of either the effective interfacial area [78] or the effective diffusivity [79]. As pertains the interfacial area, it has been suggested that as a bubble's surface gets covered by particles, the effective area available for mass transfer reduces. To model this, the concept of fractional bubble surface coverage has been employed based on adhesion isotherms that take into account the floatability of the particles under different conditions [80–82]. As pertains the effective diffusivity, it has been suggested that this parameter decreases due to the presence of particles with lower permeability to the solute gas at the interfacial film [79,83].

It has also been proposed that a solid phase can affect the overall mass transfer coefficient (K_L) by impacting the rigidity of the mass transfer interface. A mobile interface usually has its K_L characterised by a 1/2 dependence on the diffusivity [84]. A rigid interface, on the other hand, has its K_L characterised by a 2/3 dependence on the diffusivity and this is usually lower than that of a mobile interface [84]. A rigid interface can arise due to the presence of surfactants at the interface [84]. However, the introduction of a solid phase to a contaminated interface can result in its cleansing through the action of the surfactant being adsorbed onto the solid phase [71,85–87]. This re-introduces mobility at the interface thus leading to a recovery in K_L [85–87].

Finally, mass transfer changes have also been observed to occur where active solid phases such as living cells/organisms (biologically active) and catalysts (chemically active) are involved. For example, reaction enhancement by catalysts at/near the interface has been observed to lead to greater concentration gradients and hence greater mass transfer [88,89]. On the other hand, both enhancement and depression of mass transfer has been observed for biologically active organisms. For the latter, various mechanisms have been proposed such as the direct uptake of oxygen at the mass transfer interface and the change in fluid viscosity of the medium. These mechanisms are reviewed in greater detail in section 2.5.

2.2.2 Model extensions

As pertains to modelling, both the film and penetration theories discussed earlier have been extended to incorporate the solid phase based on the hypothesised mechanisms of action. For example, Kawase & Moo-Young [90,91] have modelled mass transfer in gas-liquid-solid BCRs based on the penetration theory while employing non-Newtonian viscosity models to represent the solid-liquid mixture ($\upsilon = \upsilon_{eff}$ in equation (2.11)). The resulting models predicted a decrease in K_L with increase in solid loading due to an increase in effective viscosity [90,91]. Alternatively, Wenmakers et al. [92] have considered that the presence of the solid phase will lead to a decrease in the effective diffusivity ($D = D_{eff}$ in equation (2.11)). Linek et al. [86], while keeping the diffusivity constant, have instead captured the impact of the solid phase by varying the exponent of diffusivity. They proposed that the exponent decreases from 2/3 to 1/2 as solid particles are introduced to a contaminated surface. This signified the transition of the bubble surface from fully rigid to fully mobile due to the removal of surface active contaminants by the solid particles [86].

The shuttle mechanism has been also modelled. Based on the penetration theory, Holstvoogd et al. [93] showed that the enhancement would depend on both the adsorption rate and the adsorption capacity of the particles. For the case of rapid mass transfer between the liquid and the solid phases (high adsorption rate), the adsorption capacity governed the enhancement factor (E) [88,93]. The latter was defined as the ratio of the mass transfer rate in the presence of the solid phase to that in its absence and was observed to increase with increase in solid loading. This is illustrated in equation (2.14) where x represents the solid loading based on the total volume of an un-gassed solid-liquid mixture and m represents the ratio of solute gas adsorbed on the solid phase to that dissolved in the aqueous phase at equilibrium.

$$E = \sqrt{1 + mx} \tag{2.14}$$

Finally, the effect of particle-bubble adhesion has been modelled based on the film theory [82,94–97]. Vinke et al. [82] proposed that the latter would lead to an enhancement in mass transfer through a decrease in the effective thickness of the interfacial film. This is illustrated in Figure 2.3 with the resulting enhancement factor given in equation (2.15) [82]. In this equation, ζ represents the fractional bubble surface coverage whereas K_{Lp} represents the overall mass transfer coefficient for the covered portion of the interface. The latter is defined in terms of the film theory (see equation (2.8)), with the effective thickness of the interfacial film approximated in terms of the particle radius (r_p) [82,94]. The ratio τ/τ_O, on the other hand, represents the ratio of the residence time of the solid particle at the mass transfer interface to its saturation time [82,94]. It has been observed that the fractional bubble surface coverage attains to a maximum value thereby imparting an asymptotic behaviour to the enhancement factor. This trend has been in agreement with experimental measurements [88,94] thus prompting the adoption of this model by other authors [98–100].

$$E = 1 + \zeta \left\{ \frac{K_{Lp}}{K_L} \left(1 - \frac{\exp(-\tau/\tau_O)}{\tau/\tau_O} \right) - 1 \right\}; \qquad K_{Lp} = 2D/r_p \tag{2.15}$$

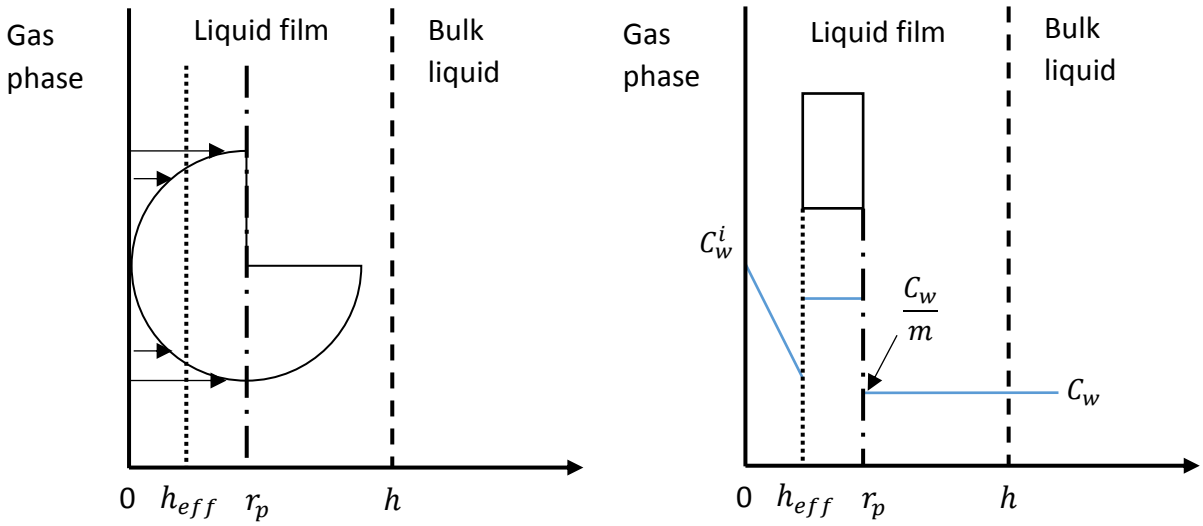

Figure 2.3: Mass transfer interfacial film with an adhered particle symbolised by cut circle (left side). Solid particle represented as a slab at a distance h_{eff} from the interface (right side). Redrawn from Vinke et al. [82] with permission.

2.3 CFD for gas-liquid mass transfer

As was concluded in section 2.1, the prediction of oxygen transfer in bioreactors on the basis of theoretical models requires an estimation of quantities such as the energy dissipation rate and the slip velocities. These values can be derived in an averaged sense from the operating conditions thus giving rise to semi-theoretical models. Garcia-Ochoa & Gomez [64] have used such models to estimate $K_L a_{\alpha_o=0}$ in reactors of varying sizes (2 – 1000 L STRs) to within $\pm 15\%$. This success notwithstanding, the reliance of these models on volume-averaged variables is contrary to the observed spatial heterogeneity within reactors [21]. Thus, for effective bioreactor design, one also needs to resolve this spatial heterogeneity.

Computational Fluid Dynamics (CFD) can be employed to provide spatially resolved estimates of the values of interest. This is possible with CFD since the latter provides an approximate (numerical) solution to the fundamental equations governing fluid flow [101]. In addition, the CFD solutions are provided on a discretised mesh of the reactor (domain) and this allows for the capture of spatial heterogeneity [101]. CFD output such as the turbulent energy dissipation rate, velocities and phase hold ups can then be coupled to theoretical models so as to predict mass transfer. In addition, the bubble size distributions (BSD) and their moments (such as Sauter mean diameter) can be predicted based on a coupling of the CFD model with a population balance model (PBM) [34].

The CFD-PBM modelling approach has become increasingly popular in recent years due to several reasons. First, there has been an increase in the computational power available to researchers and industry practitioners thus supporting the use of CFD-PBM given that it is computationally intensive by nature [21]. Second, the CFD-PBM technique has been undergoing continuous research and development so as to improve its predictive accuracy *vis-à-vis* experimental measurements in reactors [32,102–109]. Last but not least, the CFD-PBM technique has been viewed as an attractive option for scale-up studies since it is anchored on the solution of fundamental flow equations thus making it scale-independent. To this end, it has been suggested that this technique can replace pilot-scale experiments in the design cycle [21] thus leading to a speed-up and cost reduction of the design process.

Table 2.1 gives an overview of some of the studies that have been conducted based on the CFD-PBM approach. Modelling at various scales (2 – 785 L) has been attempted for both STRs and BCRs [24,110]. In addition, different modelling techniques have been proposed to

capture different phenomena within the reactors. Such techniques include those aimed at resolving the impeller motion in STRs (sliding mesh – SM, multiple reference frame – MRF, snapshot approach) as well as those aimed at modelling turbulence in the reactors (dispersed and realizable $k-\epsilon$ models, $k-\omega$ model). Furthermore, whereas a number of studies have assumed a monodisperse bubble size within the reactors, BSDs have also been modelled based on PBMs. The latter have been solved through different algorithms such as the method of classes (MC), the quadrature method of moments (QMOM) and the multiple size group method (MUSIG). The bubble number density (BND) model has also been employed as a simplification to PBMs.

The developed CFD-PBM models have been examined in terms of both global and local (spatially distributed) values of the gas hold up, the bubble sizes and $K_L a_{\alpha_o=0}$. Table 2.1 illustrates that recent models have generally been within $\pm$35% of experimental values, with the exception being a study on non-Newtonian flows where $K_L a_{\alpha_o=0}$ values were poorly predicted ($\pm$85%). The CFD-PBM models have also been able to capture spatial heterogeneity illustrating, as an example, that bubbles have a smaller size in the impeller discharge whereas in other areas of the reactor larger bubbles occur due to coalescence [111]. Similarly, it has been shown that $K_L a_{\alpha_o=0}$ (based on equation (2.11)) will be higher in the impeller discharge due to a higher value of the turbulent energy dissipation rate [22]. Such insight cannot be obtained based on empirical or semi-theoretical models thus underscoring the strength of the CFD-PBM approach.

The CFD-PBM approach has also been extended to model gas-liquid-solid systems in both biological and non-biological processes. With regards to biological processes, systems such as wastewater treatment [112], cell cultivation [113] and enzyme production [114] have been modelled. For such processes, CFD-PBM models have been used to identify zones in reactors with low substrate (or oxygen) concentrations, with such insight leading to optimal reactor design and operation [113]. On the other hand, modelling efforts in non-biological processes such as mineral flotation have been aimed at capturing the hydrodynamics of the reactors [81,115,116]. In such systems, the hydrodynamics inform particle-bubble attachment and detachment processes thus dictating the efficiency of the flotation process [81,115,116]. The ability of the CFD-PBM approach to capture the complex hydrodynamics in such multiphase systems has been a key point of attraction.

Table 2.1: Overview of studies employing CFD-PBM for gas-liquid mass transfer			
Reactor type [Reference]	**CFD-PBM approach**	**Variables predicted**	**Remarks**
STR [111]	1. MRF 2. Dispersed $k-\epsilon$ turbulence model 3. BND	1. Gas hold up 2. Average bubble size	1. CFD-based gas hold up about 8% lower than experimental value. 2. Small bubbles in impeller discharge. Large bubbles elsewhere due to coalescence.
STR [24]	1. MRF 2. Dispersed $k-\epsilon$ turbulence model 3. PBM (MC)	1. Sauter mean diameter 2. $K_L a_{\alpha_o=0}$ (eqn. (2.11) with $\Lambda = 2/\sqrt{\pi}$)	1. Incorporation of PBM improved prediction of $K_L a_{\alpha_o=0}$ (0.017 s^{-1} by CFD-PBM versus 0.0169 s^{-1} measured experimentally).
STR [22]	1. MRF 2. Realizable $k-\epsilon$ turbulence model 3. PBM (QMOM)	1. Sauter mean diameter 2. $K_L a_{\alpha_o=0}$ (eqn. (2.12) and eqn. (2.11) with $\Lambda = 0.4$)	1. Agreement between predicted and measured local bubble sizes. 2. Local $K_L a_{\alpha_o=0}$ by eqn. (2.11) higher around impeller region whereas that by eqn. (2.12) is higher in the bulk.
STR [23]	1. MRF 2. Dispersed $k-\epsilon$ turbulence model 3. PBM (MUSIG)	1. Gas hold up 2. Sauter mean diameter 3. $K_L a_{\alpha_o=0}$ (equations (2.11) – (2.13))	1. CFD-based gas hold up aboout 21% higher than experimental value. 2. $K_L a_{\alpha_o=0}$ values by equations (2.12) and (2.11) with $\Lambda = 0.4$ within $\pm$15% of experimental values. Other models performed poorly.
STR [117]	1. MRF 2. $k-\omega$ turbulence model 3. PBM (MUSIG)	1. Gas hold up 2. Sauter mean diameter 3. $K_L a_{\alpha_o=0}$ (non-Newtonian variant of eqn. (2.11))	1. CFD-based gas hold up values within $\pm$35% of experimental values. 2. $K_L a_{\alpha_o=0}$ values within $\pm$85% of experimental values.
STR [110]	1. MRF and SM 2. Per phase $k-\epsilon$ turbulence model 3. BND	1. Gas hold up 2. Sauter mean diameter	1. CFD-based gas hold up values within $\pm$25% of experimental values. 2. Effect of turbulence on the rise velocity of bubbles investigated.

Table 2.1: Overview of studies employing CFD-PBM for gas-liquid mass transfer			
Reactor type [Reference]	**CFD-PBM approach**	**Variables predicted**	**Remarks**
STR [33]	1. Snapshot approach 2. Dispersed $k-\epsilon$ turbulence model 3. Monodisperse	1. Gas hold up	1. CFD-based gas hold up values about 15% – 20% higher than experimental values. 2. Effect of turbulence on the rise velocity of bubbles investigated.
STR [36]	1. SM 2. Multiphase $k-\epsilon$ turbulence model 3. Monodisperse	1. Gas hold up	1. CFD-based gas hold up values within ±5% of experimental values. 2. Effect of non-drag forces investigated.
BCR [118]	1. 2D axisymmetric simulation 2. Dispersed $k-\epsilon$ turbulence model 3. PBM (MC)	1. Gas hold up 2. Sauter mean diameter 3. $K_L a_{\alpha_o=0}$ (equations (2.11) – (2.12))	1. CFD-based gas hold up values in both bubbly and churn-turbulent flow regimes agreed with experimental values. 2. $K_L a_{\alpha_o=0}$ values by equations (2.11) and (2.12) were similar though there was slight adjustment of the models' constants. Good agreement with experimental values observed.
BCR [119]	1. 2D axisymmetric simulation 2. Dispersed $k-\epsilon$ turbulence model 3. PBM (MC)	1. Gas hold up 2. Bubble size distributions (BSD)	1. Hydrodynamics and gas hold up well predicted for both bubbly and churn-turbulent flow regimes. 2. BSD predicted for different flow regimes through incorporation of PBM.
BCR [120]	1. 2D axisymmetric simulation 2. Dispersed $k-\epsilon$ turbulence model 3. PBM (MC)	1. Gas hold up 2. $K_L a_{\alpha_o=0}$ (eqn. (2.12))	1. Different operating conditions (pressures, temperatures, superficial .gas velocities) and liquid properties (viscosity, surface tension) examined. 2. Average gas hold up adequately captured (±20%). 3. Reasonable $K_L a_{\alpha_o=0}$ predictions up to 1 MPa (±15%) with further model improvement required for higher pressure range.

2.4 Gas-liquid-liquid mass transfer

The introduction of secondary immiscible liquids such as hydrocarbons, perfluorocarbons and ionic liquids into gas-liquid systems has been explored in both aerobic fermentation and biological waste gas treatment [9,121,122]. In such cases, the secondary liquid phase is introduced so as to act as a carrier or reservoir of the solute gas. However, in alkane biocatalysis, the primary role of the alkane phase as the secondary liquid phase is to provide the substrate for the cells/organisms. This notwithstanding, oxygen transfer in alkane biocatalysis is impacted by the secondary liquid phase in a manner similar to these gas-liquid-liquid systems. Thus, it can be examined in the wider context of such systems.

An analysis of literature reveals that, similar to gas-liquid-solid systems, gas-liquid-liquid systems have shown varying results where mass transfer is concerned. Clarke & Correia [9] summarised the reported results on the overall volumetric mass transfer coefficient into three trends. These included an initial increase to a maximum followed by a decrease, an initial increase that was sustained or plateaued at a peak value and finally a constant or decreasing value [9]. These trends were observed with respect to an increase in the volume fraction of the secondary liquid phase. In seeking to explain these trends, Clarke & Correia [9] focussed on the impact that addition of the secondary liquid phase would have on the effective fluid properties and the system's turbulence. However, before delving into these factors, it is proposed that the variation in reported results can be partially explained by a re-examination of how the overall volumetric mass transfer coefficient is computed in such systems [123]. Central to this is the question of how changes in the solubility of the system on introduction of the secondary liquid phase are accounted for in the formulations employed [123–125]. This is discussed further in the next section.

2.4.1 Measurement of the overall volumetric mass transfer coefficient

The dynamic gassing-out method, an experimental method initially designed for gas-liquid systems, is commonly used in gas-liquid-liquid systems to obtain a measure of the overall volumetric mass transfer coefficient [15,17,126]. Its use is made possible by the fact that dissolved oxygen probes measure oxygen tension which is the same in all phases at equilibrium [127]. The obtained measurements, reported as concentration profiles, are then fitted to models such as equations (2.16) – (2.17) so as to compute the overall volumetric mass transfer coefficient in the presence of a secondary liquid phase ($K_L a'$) [15,17,126]. In

these equations, the solubility of the solute gas in the liquid-liquid mixture (C^*) is defined as the volumetric average of the solubility in the aqueous phase (C_w^*) and that in the secondary liquid phase (C_o^*) [9,40,128,129]. The volume fraction of the secondary liquid phase based on the total liquid volume is represented by x. It is to be noted that this equation is a direct extension of equation (2.1) based on the assumption that the liquid-liquid mixture can be represented as a pseudo-homogenous liquid with a higher solubility (usually $C_o^* > C_w^*$).

$$\frac{dC}{dt} = K_L a\,'(C^* - C) \tag{2.16}$$

$$C^* = (1 - x)C_w^* + xC_o^*. \tag{2.17}$$

An alternative model to the above equations can be derived by considering the heterogeneity of the liquid-liquid system. For such a system, mass balance equations can be posed as given by equations (2.18) – (2.19) [128].

$$\text{OTR} = E \cdot K_L a\,(C_w^* - C_w\,) \tag{2.18}$$

$$\text{OTR} = (1 - x)\frac{dC_w}{dt} + x\frac{dC_O}{dt} \tag{2.19}$$

Equation (2.18) above defines the mass transfer flux based on the changes at the gas-liquid interfacial film. The enhancement factor (E) accounts for new mass transfer pathways that can be introduced by the secondary liquid phase (discussed later). Equation (2.19), on the other hand, considers the changes in the bulk. Based on this equation, it can be observed that for a fixed OTR, the rate of change in solute gas concentration dissolved in the aqueous phase (dC_w/dt) decreases with an increase in volume fraction of the secondary liquid phase. Alternatively, the system takes longer to saturate on introduction of the secondary liquid phase due to a higher absorption capacity (solubility) [70,123].

Substituting equation (2.19) into equation (2.18) results in equation (2.20) [123]. In this equation, $E\,'$ represents a modified enhancement factor whereas m represents the solubility ratio. This equation is simplified based on an assumption of equilibrium in concentrations of the solute gas dissolved in both liquid phases ($C_o^* = mC_w^*$). The equilibrium assumption is

justifiable given that the secondary liquid phase is usually dispersed within the primary liquid phase resulting in a high interfacial area that permits for rapid partitioning of the dissolved solute gas [130].

$$\frac{dC_w}{dt} = E' \cdot K_L a \, (C_w^* - C_w) \, ; \quad E' = \frac{E}{1 + x(m-1)} \tag{2.20}$$

Equations (2.16) and (2.20) are equivalent since both can be expressed in terms of partial pressure (see equation (2.2)) with Henry's constants arising on both the right- and left-hand sides of the equations cancelling out. In addition, since the dynamic gassing-out method measures oxygen tension rather than actual concentrations, both equations can be equally applied to describe the system. However, different measures of the overall volumetric mass transfer coefficient emerge. These different measures have been reported in literature as highlighted in Table 2.2 and Table 2.3. It is to be noted that whereas the equations described above are derived for a liquid-phase analysis of mass transfer, complementary equations have been derived for gas-phase analysis [131,132]. This has been taken into consideration in populating Table 2.2 and Table 2.3.

Table 2.2: $K_L a'$ values for gas-liquid-liquid systems focussing on oxygen transfer

Reactor type [Reference]	Primary liquid phase	Secondary liquid phase [Concentration]	$K_L a'$ trend with increasing volume fraction of secondary liquid phase
STR [129]	Water	PFC-40 [0 – 10%]	Constant.
STR [126]	Water	Silicone oil [0 – 50%]	Initial increase (up to $x = 10\%$) followed by decrease at 400 rpm. Opposite trend at 600 rpm.
STR [15]	Water	n-$C_{12\text{-}13}$ [0 – 20%]	Initial increase (up to $x = 10\%$) then decrease for $\geq$ 800 rpm. Decrease for < 800 rpm.
STR [19]	Water	PFC [0 – 30%]	Varied behaviour depending on impeller type, agitation and aeration rate.
		Olive oil [0 – 20 %]	Decrease.
STR [17]	Aqueous growth medium	n-Hexadecane [0 – 33%]	Decrease.
STR [132]	Water	n-Heptane [0 – 100%]	Increase up to $x = 15\%$ and again from $x = 40\%$ up to phase inversion ($x \approx 60\%$).
		n-Dodecane [0 – 100%]	Initial increase (up to $x \approx 1\%$) followed by decrease in oil-in-water emulsions ($x < 60\%$).
		n-Hexadecane [0 – 100%]	Initial increase (up to $x \approx 2\%$) followed by decrease in oil-in-water emulsions ($x < 60\%$).

Table 2.3: $K_L a$ values for gas-liquid-liquid systems focussing on oxygen transfer

Reactor type [Reference]	Primary liquid phase	Secondary liquid phase [Concentration]	$K_L a$ trend with increasing volume fraction of secondary liquid phase
STR [128]	Water	n-C_{11-18} [0 – 100%]	Constant K_L for oil-in-water emulsion ($x < 18\%$).
STR [133]	Water	n-Heptane [0 – 5%]	Initial decrease (up to $x \approx 1\%$) followed by an increase.
		n-Dodecane [0 – 5%]	Initial increase (up to $x \approx 1\%$) followed by a decrease towards air-water value.
BCR [134]	Water	Toluene [0 – 10%]	Slightly increasing but lower than air-water case.
		Anisole [0 – 10%]	Slightly increasing but lower than air-water case.
		2-ethyl-1-hexanol [0 – 10%]	Slightly increasing but lower than air-water case.
		Decyl alcohol [0 – 10%]	Increase but only slightly higher than air-water case.
		Dodecane [0 – 10%]	Increase (initially rapid then steady).
		n-Decane [0 – 10%]	Increase (initially rapid then steady).
		n-Heptane [0 – 10%]	Increase (initially rapid then steady).
BCR [135]	Water	Silicone oils [0 – 10%]	Initial decrease ($x < 2\%$) followed by an increase.
BCR [131]	Water	PFC-40 [0 – 4%]	Constant.
		Silicone oils [0 – 10%]	Initial decrease followed by a recovery beyond 5%.
		n-Dodecane [0 – 10%]	Constant.
		n-Hexadecane [0 – 10%]	Constant.

It can be observed from Table 2.2 and Table 2.3 that even within the different measures of the overall volumetric mass transfer coefficient various trends of the latter have been reported. To explain these observations, numerous hypotheses have been put forth. For example, Dumont & Delmas [20] reviewed previous work and illustrated the potential effects of new mass transfer pathways that can be introduced by the secondary liquid phase. Clarke & Correia [9], on the other hand, have illustrated the potential impact of the secondary liquid phase on the effective fluid properties and the system's turbulence. These hypotheses are reviewed in greater detail in the next section.

2.4.2 Mass transfer mechanisms in the presence of a secondary liquid phase

The enhancement factor (E) in equation (2.18) has been previously employed to capture new mass transfer pathways that can be introduced by the secondary liquid phase [128]. Such pathways include parallel mass transfer and series mass transfer with or without shuttling (see Figure 2.4). To assess which of the pathways is most likely, the concept of the spreading coefficient (S) has been traditionally employed [128,133,136]. The latter is defined by equation (2.21), with σ representing the interfacial tension while the subscripts wg, og and ow represent the aqueous-gas, alkane-gas and alkane-aqueous interfaces respectively.

$$S = \sigma_{wg} - (\sigma_{og} + \sigma_{ow}) \tag{2.21}$$

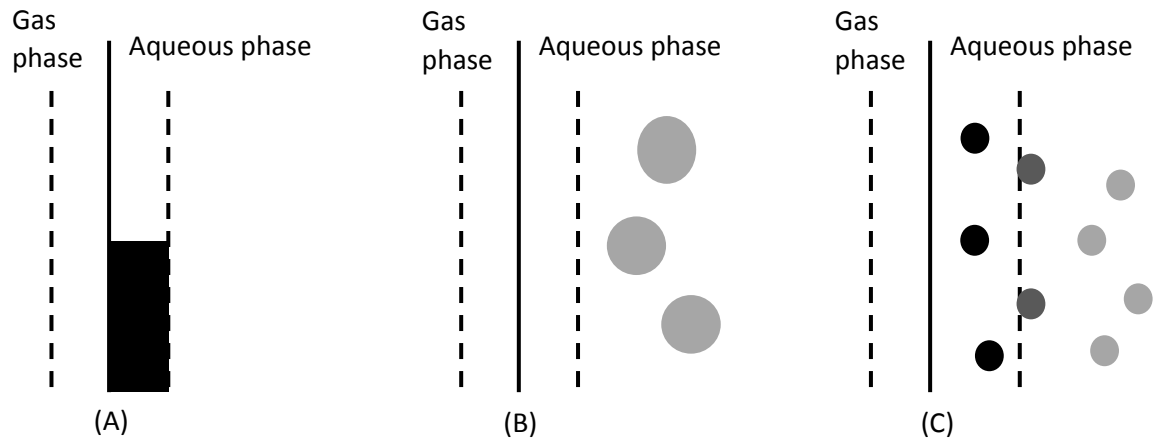

Figure 2.4: Gas-liquid boundary layer showing possible mass transfer pathways – parallel (A), series (B) and series with shuttling (C). Secondary liquid phase represented by filled symbols with degree of shading representing oxygen concentration.

For $S > 0$, the secondary liquid phase is likely to form a film on a bubble surface thus giving rise to parallel mass transfer (Figure 2.4 (A)). Experimental evidence for this has been provided based on "static interactions" of air bubbles and hydrocarbon droplets [130]. This notwithstanding, the parallel mass transfer pathway has been critiqued on various grounds. First, whereas a positive spreading coefficient may computed based on static measurements, the hydrodynamics and average coalescence time in agitated reactors may not provide sufficient time for film formation [130,137]. Second, the consideration of interfacial tension measurements of mutually saturated liquids (as opposed to pure liquids) has been shown by Brilman (cited in [20]) to give rise to negative values of the spreading coefficient. This has been noted to be the case even for systems with initially positive spreading coefficient values [20]. Such observations have led to the conclusion that the parallel mass transfer pathway remains unlikely.

Series mass transfer, on the other hand, has often been assumed to be the more likely pathway [20]. It has been traditionally associated with a negative spreading coefficient ($S < 0$). Furthermore, this pathway can be enhanced by a shuttle effect similar to that hypothesised for gas-liquid-solid systems. In this mechanism, droplets of the secondary liquid phase would have to be a size smaller than the gas-liquid interfacial film thickness (contrast Figure 2.4 (B) and (C)). This would allow them to penetrate the mass transfer film and take up the solute gas. The droplets would then be returned to the bulk fluid where they would release the solute gas due to a concentration gradient [138].

Besides the above changes, it has also been suggested that a secondary liquid phase can impact the hydrodynamics of a reactor through a change in the effective fluid properties as well as a reactor's turbulence levels [9]. For example, the effective viscosity (assuming a pseudo-homogenous liquid) has been observed to increase with increasing volume fraction of the secondary liquid phase [14]. This has been proposed to lead to a decrease in mass transfer through a decrease in turbulence and the associated decrease in renewal frequency of fluid elements at the mass transfer interface [9,14]. In addition, secondary liquid phases with high viscosities (hence low values of diffusivity) have been observed to lead to low values of effective permeability of the solute gas $\left(\sqrt{D_{eff}} \cdot C^*\right)$ despite an increase in solubility (C^*) [137].

The surface tension has also been observed to change as a result of the secondary liquid phase. Though secondary liquids used in gas-liquid-liquid systems typically have low

solubility in the primary aqueous phase, mutually saturated values of the surface tension have been observed to be lower than those of the pure aqueous phase in certain cases [132,134]. Alternatively, it has been suggested that the film formation process (for cases with $S > 0$) tends to lower the surface tension. Either of these mechanisms can result in smaller-sized bubbles and hence an increase in interfacial area. Concomitantly, a decrease in K_L can occur due to a surfactant effect [128].

With regards to the reactor's turbulence, it has been observed that droplets of a secondary liquid phase can either increase or decrease the turbulence levels in the primary liquid phase [139–141]. This interaction depends on the droplet size, its inertia, the volume fraction of the secondary liquid phase and the prevailing turbulence intensity among other factors [142–146]. Such changes in the turbulence levels can lead to corresponding changes in surface renewal frequency at the gas-liquid interface or changes in the bubble coalescence and breakup phenomena [9]. Consequently, both K_L and the interfacial area would be affected [9]. Such interactions are not easy to approximate *a priori,* hence they are often ignored when using the modelling approaches reviewed below. However, the modelling of particle-turbulence interaction based on CFD techniques [109,147] can provide an approximation of the influence of such effects.

2.4.3 Model extensions

Attempts at incorporating the mechanisms reviewed above into 2-phase gas-liquid models have been made. This has been done by proposing models that estimate the possible enhancement in mass transfer. Equations (2.22) and (2.23) provide examples of such models. Equation (2.22) has been proposed for the parallel mass transfer pathway [148] whereas equation (2.23) has been proposed for the series mass transfer pathway with shuttling [138]. In these equations, D_r represents the ratio of solute gas' diffusivity in the secondary liquid phase to that in the primary liquid phase. Additionally, m and x represent the solubility ratio and the volume fraction of the secondary liquid phase respectively.

$$E = 1 + x(m\sqrt{D_r} - 1) \tag{2.22}$$

$$E = \sqrt{1 + x(m - 1)} \tag{2.23}$$

Models such as those given above offer a first approximation to possible mass transfer enhancement. They have been shown to approximate mass transfer phenomena in equipment with fixed interfacial area such as a stirred cell [138] and a laminar film absorber [149]. Furthermore, these models have been improved upon by taking into account greater detail such as the spatial distribution of droplets near the interface [148,150–153]. However, an underlying criticism of these models has been that they only predict continuous enhancement whereas experimental results show varied behaviour (see Table 2.2 and Table 2.3). Pinho & Alves [154] have recently commented on this arguing that the enhancement factor should be formulated so as to contain both enhancing and retarding factors as competing parameters. These same remarks can be extended to empirical models that have been proposed based on single trends, such as that in equation (2.24) [17].

$$K_L a' = \Gamma \cdot \left(\frac{P_g}{V}\right)^{\beta} v_s{}^{\delta}(1-x)^{\zeta} \tag{2.24}$$

In seeking to address the above, Pinho & Alves [154] have proposed semi-empirical models for the enhancement factor that contain both enhancing and retarding factors. For a spreading phase ($S > 0$), they suggested that film formation on the gas bubble at low interfacial hold up of the secondary liquid phase would lead to an increase in mass transfer resistance [154]. However, at high interfacial hold up, the shedding of saturated (or near saturated) droplets of the secondary liquid phase from the film would enhance mass transfer [154]. For a non-spreading phase ($S < 0$), they suggested that the shuttle effect would lead to enhancement at low interfacial hold up [154]. At high interfacial hold up, however, mass transfer would be retarded due to increased resistance in a manner similar to cases with $S > 0$ [154].

Zhang, Cai et al. [155], on the other hand, have considered a hydrodynamic effect in addition to the shuttle effect. Their model, based on the penetration theory, resulted in an equation similar to equation (2.11). In their equation, an effective diffusivity employed that incorporated the shuttle effect ($D = D_{eff}$) [155]. In addition, effective values of the viscosity and density were employed based on the assumption that the liquid-liquid mixture could be treated as a pseudo-homogeneous liquid [155]. This use of effective fluid properties together with the consideration of changes in the energy dissipation rate constituted the hydrodynamic effect. It was suggested that this effect would dominate at high loadings of the secondary liquid phase [155]. At these conditions, an increase in the effective viscosity would lead to a decrease in mass transfer for a constant energy dissipation rate [155].

2.5 Gas-liquid-liquid mass transfer in the presence of a solid phase

A complete analysis of gas-liquid-liquid systems requires the consideration of the cells/organisms introduced to carry out the relevant bioprocesses such as fermentation or alkane biocatalysis. These cells form a separate solid phase and are usually of a smaller dimension relative to the gas bubbles and droplets of the secondary liquid phase. As an example of this, diameters of 1 – 20 μm have been reported for *S. cerevisiae* cells in comparison to bubble diameters of about 1 mm [16].

The presence of cells/organisms in a system can introduce changes to the mass transfer behaviour of the reactor. This is highlighted in the examples enumerated in Table 2.4. The table provides a summary of experimental work that has been done with the focus of quantifying the effects of both the secondary liquid phase and the solid phase (cells) on oxygen transfer. It excludes studies done in similar gas-liquid-liquid-solid systems whose objectives were not in line with those of this work. For example, it excludes studies whose focus was on the promotion of maximum growth and productivity of the cells [156–159]. In addition, it excludes studies whose focus was on the mass transfer of volatile organic compounds (for example, methane or benzene) as applied to the abatement of air pollution [121,160].

2.5.1 Mass transfer mechanisms in the presence of a solid phase

It can be observed from Table 2.4 that the solid phase has been predominantly observed to lead to a decrease in $K_L a'$. As these results are based on deactivated (non-viable) cells, similar mechanisms to those reviewed in section 2.2 may be suggested. Active cells, on the other hand, can introduce extra mechanisms through which oxygen transfer is impacted. For example, the latter are known to enhance oxygen transfer due to direct oxygen uptake at the gas-liquid interface [161]. This interaction of the cells with the gas-liquid interface is dependent on their hydrophobicity, a property that has been observed to change depending on the cell type and the cell's growth phase [160,162].

It has also been observed that extra-cellular secretions by active cells can have surface active effects. This can lead to an increase in interfacial area [163] and a concomitant decrease in K_L. The overall effect of these competing factors on $K_L a'$ depends on their magnitude. Finally, morphological changes in growing cells (pellets versus filamentous mycelia) have been

observed to result in changes to the effective viscosity thus impacting the mass transfer process [114].

Table 2.4: $K_L a'$ values for gas-liquid-liquid-solid systems focussing on oxygen transfer

Reactor type [Reference]	Primary liquid phase	Secondary liquid phase/ Cell type [Concentrations]	$K_L a'$ trend with introduction of cells and secondary liquid phase
STR [16,164]	Water	n-C_{13}-C_{21}/ *S. cerevisiae* [2 – 20%] [1 – 10 g/L]	The agitation rate, cells' concentration and n-C_{13}-C_{21} volume fraction observed to have statistically significant effects on $K_L a'$ (80% confidence level). The addition of n-C_{13}-C_{21} resulted in an initial increase in $K_L a'$ followed by a decrease (peak at around 11% volume fraction). At high agitation rates, a negative effect of cells' concentration was observed whereas at low agitation rate a slightly positive effect was observed.
STR [19]	Growth medium	PFC/ *Y. lipolytica* [0 – 30 %] [0 – 10 g/L]	PFC addition resulted in a positive effect on $K_L a'$. Addition of the cells resulted in a slight decrease in $K_L a'$.
STR [165]	Broth	n-Dodecane/ *P. shermanii* [0 – 20%] [30.5 – 120.5 g/L]	n-Dodecane addition resulted in an increase in $K_L a'$. Addition of the cells resulted in a decrease in $K_L a'$.
STR [166]	Broth	n-Dodecane/ *P. shermanii* [0 – 20%] [30.5 – 120.5 g/L]	n-Dodecane addition resulted in an increase in $K_L a'$. Addition of the cells resulted in a decrease in $K_L a'$.
		n-Dodecane/ *S. cerevisiae* [0 – 20%] [43 – 150 g/L]	

2.5.2 Model extensions

In terms of modelling, the empirical approach has been adopted due to the complexity of such systems. Equation (2.25) by Amaral et al. [19] and equation (2.26) by Galaction et al. [165,166] are examples of models that have been proposed. In these equations, Ω represents the cells' concentration by dry weight with its effect captured through exponent ξ whereas x represents the volume fraction of the secondary liquid phase. Other terms are as previously defined. It can be observed that though the basic structure of equation (2.4) for gas-liquid systems has been maintained, differences have emerged in terms of how to capture the effects of both the secondary liquid phase and the solid phase.

$$K_L a' = \Gamma \cdot \left(\frac{P_g}{V}\right)^{\beta} {v_s}^{\delta} (1-x)^{\zeta} \Omega^{\xi} \tag{2.25}$$

$$K_L a' = \Gamma \cdot \left(\left(\frac{P_g}{V}\right)^{\beta} {v_s}^{\delta} \Omega^{\xi}\right)^{x} \tag{2.26}$$

2.6 CFD for gas-liquid-liquid mass transfer

In comparison to gas-liquid systems, the addition of a secondary liquid phase and a solid phase (cells) complicates the hydrodynamics in a reactor. As noted before, the prevailing hydrodynamics can change through multiple mechanisms such as changes to the effective fluid properties or turbulence modification. Such changes have an effect on mass transfer. Consequently, these need to be accounted for by the CFD techniques employed.

To the best of the author's knowledge, few studies have been undertaken on the CFD-based modelling of gas-liquid-liquid systems. Such studies have been in diverse fields such as the flow in mini-channels [167], the flow on inclined plates for distillation column packings [168] and the flow in annular centrifugal separators [169]. With regards to gas-liquid-liquid STRs, there has been some work done on macro-mixing as characterised by the mixing time [170,171]. These studies, however, fell short of investigating mass transfer. Moradkhani et al. [172], on the other hand, have studied oxygen transfer and phenol biodegradation in a gas-liquid-liquid STR. However, the details given on their experimental setup suggest that the primary and secondary liquid phases remained stratified (flat interface) while only the gas phase was dispersed [172,173]. This setup is quintessentially different from that investigated

in this work in which both the gas phase and the secondary liquid phase are dispersed within the primary liquid phase (aqueous phase). Besides this, a more systematic and detailed numerical investigation of the hydrodynamics and mass transfer in alkane-based stirred bioreactors is presented herein.

2.7 Summary

The foregoing discussion has illustrated that mass transfer in 2-phase gas-liquid systems is a fairly well understood topic that has seen the development of predictive models based on fundamental considerations. Research has also been conducted into the case of gas-liquid mass transfer in the presence of a solid phase with the results showing varying trends. Various hypotheses have been suggested to explain the latter and these hypotheses have guided attempts at extending the 2-phase fundamental predictive models. Recent work, however, has been focused on the prediction of mass transfer based on Computational Fluid Dynamics (CFD). This involves the use of CFD models to capture the hydrodynamics of reactors, with the CFD output coupled to fundamental models of the overall volumetric mass transfer coefficient. The end result of this approach has been the development of scale-independent design tools that are able to resolve spatial heterogeneity within reactors.

With the aim of developing similar CFD-based tools for use in alkane-based systems, the foregoing discussion has identified several gaps that need to be addressed with regards to such systems. First, it has been shown that there is a lack of consistency in literature on the reporting of the overall volumetric mass transfer coefficient. Different measures of the latter have been reported. This has partly served to hinder the consistent extension of 2-phase fundamental mass transfer theories to alkane-based systems and consequently, various modelling approaches have been proposed. This observation served as the basis of the first research question of this study which asked, “What are the appropriate fundamental models that can be employed to predict oxygen transfer in alkane-based bioprocesses based on CFD output?” Chapter 3.0 addresses this gap by proposing a consistent modelling framework for the overall mass transfer coefficient.

A second gap noted from the foregoing discussion was the lack of clarity on the effect of the additional phases (liquid and cells/organisms) on the hydrodynamics and oxygen transfer. Various mechanisms of action have been proposed such as a change in the fluid properties (viscosity, surface tension) or a change in the turbulence levels. However, what remains

unclear is which of these mechanisms are dominant and which should be accounted for in modelling. This observation led to the second research question of this study which asked "What are the main differences in the hydrodynamics and oxygen transfer of an alkane-based bioprocess in comparison to a 2-phase gas-liquid system? Can these be captured based on CFD modelling?" Chapter 6.0 addresses this question with reference to the 3-phase (cell-free) system whereas Chapter 7.0 extends the work to incorporate the effects of the solid phase (non-viable yeast cells).

A final gap noted in the discussion was the scarcity of literature on CFD-based modelling of alkane-based systems. This inspired the last two research questions asked in this study that touched on the accuracy of the proposed CFD modelling. In particular, it was asked, "How does CFD-based prediction of oxygen transfer in a 3-phase cell-free alkane-based bioprocess compare with experimental data?" Similarly, the question was posed for the 4-phase system, "How does CFD-based prediction of oxygen transfer in a 4-phase alkane-based bioprocess with non-viable yeast cells compare with experimental data?" These questions have been respectively addressed in Chapters 6.0 and 7.0.

3.0 Modelling framework for the overall mass transfer coefficient in alkane-based systems

This chapter addresses the first gap identified in the literature review by proposing a theoretically consistent modelling framework for the overall mass transfer coefficient in alkane-based systems. The framework has been tested against experimental data to illustrate its applicability. Furthermore, it has been proposed that CFD-based modelling of oxygen transfer in alkane-based systems can be performed on the basis of this framework. Thus, the first objective of this study was tackled in this chapter.

The results based on this chapter were presented at the 2017 Heat Transfer, Fluid Mechanics and Thermodynamics conference and subsequently published in the conference proceedings [123].

3.1 Modelling rationale

From Chapter 2.0, it has been established that theoretical models have been proposed to account for possible effects introduced by a secondary liquid phase on the overall volumetric mass transfer coefficient. These include, as an example, the model proposed for the shuttling effect (see equation (2.23)). However, such models predict continuous enhancement in mass transfer with increasing volume fraction of the secondary liquid phase whereas experimental results illustrate both enhancement and depression. Thus, it has been suggested that enhancement factors should be formulated so as to contain both enhancing and retarding factors [154]. While this may be true, there is also need to consider that different measures of the overall volumetric mass transfer coefficient have been reported in literature. These differ in terms of the details captured in the equations from which they were derived. The question thus arises whether this lack of consistency may have resulted in a failure to account for certain enhancing or retarding effects. This idea is further explored in this chapter.

3.2 Model equations

Experimental studies of oxygen transfer in alkane-based systems are typically done using the dynamic gassing-out method based on equation (2.16) (repeated on next page). This equation employs the assumption that the liquid-liquid mixture can be treated as a pseudo-homogenous

liquid characterised by volume-averaged values of the oxygen concentration (C) and its saturation value (C^*). The $K_L a'$ values obtained from this equation do not reveal much about possible changes at the mass transfer interface.

Equation (2.20), on the other hand, provides a more elaborate description of the mass transfer process. It takes into account the heterogeneity of the mixture. In this equation, the oxygen concentration (C_w) and its saturation value (C_w^*) are described based on the aqueous phase. In addition, the equation describes two competing factors that a secondary liquid phase can introduce – an enhancement due to new mass transfer pathways (E) and an apparent decrease in the mass transfer rate due to a greater absorption capacity (solubility) of the mixture. This latter effect is represented by the denominator in equation (2.20) and can be observed to be a function of the volume fraction of the secondary liquid phase (x) as well as the solubility ratio (m).

Both equations (2.16) and (2.20) can be equally applied to describe alkane-based systems. Their equivalence arises from the fact that both can be expressed in terms of partial pressure (see equation (2.2)) with Henry's constants arising on both the right- and left-hand sides of the equations cancelling out. In addition, the dynamic gassing-out method measures oxygen tension rather than actual concentrations. Thus, a definition for $K_L a'$ emerges as given in equation (3.1). This can be further re-written as equation (3.2) based on experimental observations that the $K_L a$ values from equation (2.20) or its variants tend to be equal to that in primary liquid phase ($K_L a_{\alpha_o=0}$) for low volume fractions of the secondary phase [123,128,131]. Since this proposition does not always hold (see Table 2.3), an approximation ($\approx$) is employed in equation (3.2) [123].

$$\frac{dC}{dt} = K_L a'(C^* - C) \tag{2.16}$$

$$\frac{dC_w}{dt} = E' \cdot K_L a\,(C_w^* - C_w)\,; \quad E' = \frac{E}{1 + x(m-1)} \tag{2.20}$$

$$K_L a' = E' \cdot K_L a \tag{3.1}$$

$$\frac{K_L a'}{K_L a_{\alpha_o=0}} = E' \cdot \frac{K_L a}{K_L a_{\alpha_o=0}} \approx E' \tag{3.2}$$

The above modelling approach is appealing in that it allows for $K_L a'$ values to be approximated based on fundamental mass transfer equations specified for gas-liquid systems. In addition, changes to the reactor's hydrodynamics (as described by an appropriate CFD model) can be captured through predicted values of the energy dissipation rate, the gas hold up and the bubble diameter. This represents a relaxation of the common assumption of constant energy dissipation rate (or hydrodynamics) employed in models such as those by Zhang, Cai et al. [155].

The specification of the modified enhancement factor (E') in equation (3.2) would depend on the prior assumptions concerning the governing mass transfer pathway. Various enhancement factor models can be obtained as given in equations (3.3) and (3.4) [123]. These equations respectively represent parallel and series mass transfer, both scaled down by a factor capturing the apparent decrease in oxygen transfer rate due to an increase in mixture's solubility [123]. The exponent φ in equation (3.4) takes on a value of 0.5 for series mass transfer with shuttling and a value of 1 for series mass transfer without shuttling [123]. The predictions by these equations are contrasted with the respective unmodified/original models in Figure 3.1 and Figure 3.2.

$$E' = \frac{1 + x(m\sqrt{D_r} - 1)}{1 + x(m - 1)} \tag{3.3}$$

$$E' = \frac{1}{(1 + x(m - 1))^{\varphi}} \tag{3.4}$$

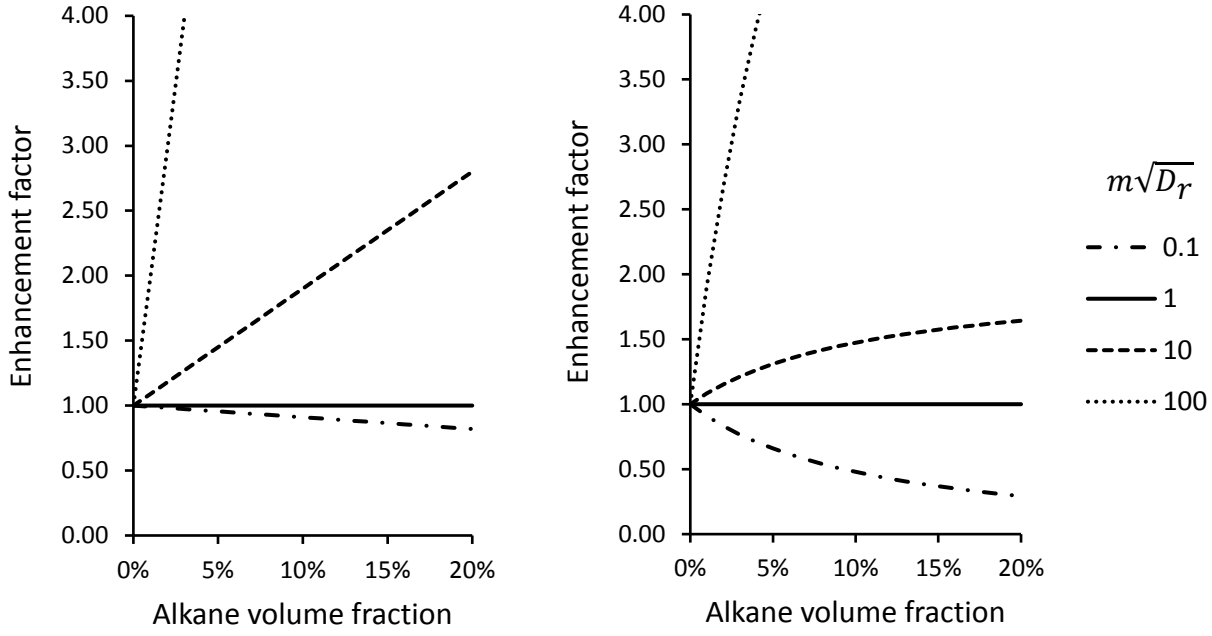

Figure 3.1: Enhancement factor versus volume fraction of secondary liquid phase for mass transfer in parallel (solubility ratio, $m = 10$). Right side – equation (3.3). Left side – equation (2.22).

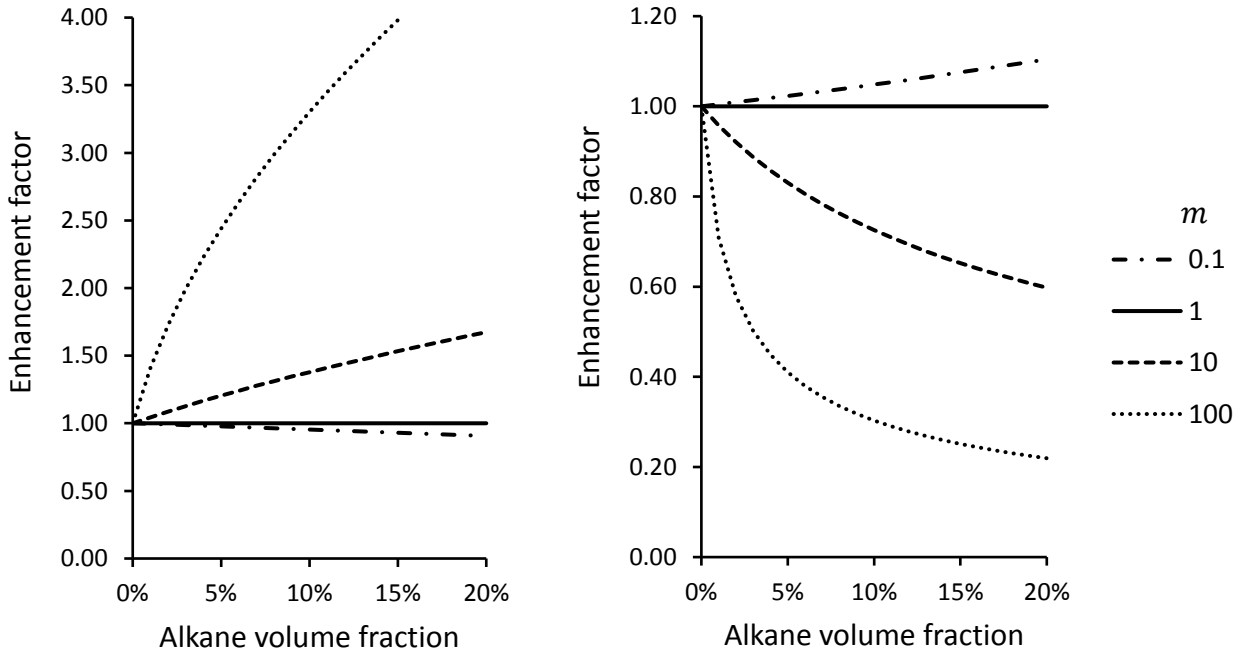

Figure 3.2: Enhancement factor versus volume fraction of secondary liquid phase for mass transfer in series with shuttling. Right side – equation (3.4). Left side – equation (2.23).

The left-side images of Figure 3.1 and Figure 3.2 illustrate enhancement in mass transfer as predicted by the original models (equations (2.22) and (2.23) respectively). The exception to this is when the parameters $m\sqrt{D_r}$ and m are less than unity. Since the secondary liquid phase is typically characterised by a greater solubility of oxygen ($m > 1$), the predicted decrease in mass transfer based on equation (2.23) (left image of Figure 3.2) rarely occurs. On the other hand, a decrease in mass transfer can occur for the parallel case when the diffusivity ratio is rather small ($D_r = 0.001$ for $m\sqrt{D_r}$ = 0.1 whereas $D_r = 0.01$ for $m\sqrt{D_r}$ = 1 on Figure 3.1).

The right-side images of Figure 3.1 and Figure 3.2 illustrate both enhancement and depression of mass transfer based on the modified models (equations (3.3) and (3.4) respectively). The cases of $m\sqrt{D_r}$ and m being less than unity have already been highlighted as rare occurrences. Consequently, the parallel mass transfer model predicts a nil or an asymptotic increase in mass transfer once the solubility effect is accounted for whereas the series mass transfer model with shuttling predicts a nil or an asymptotic decrease of the same. For series mass transfer without shuttling, similar results to those displayed on the right-side image of Figure 3.2 were obtained.

3.3 Case study

To test the hypothesised model represented by equation (3.2), an initial examination of oxygen transfer measurements in a cell-free system mimicking alkane biocatalysis was performed [123]. The experimental work by Correia et al. [14,25] was considered in which the overall volumetric mass transfer coefficient was measured based on two methodologies – the pressure step method and the dynamic gassing out method. The latter method, commonly employed in literature, is known to under-predict values of $K_L a'$ in non-coalescing media due to its assumption of uniform gas-phase concentration in the dispersed gas bubbles [25,42,174]. The pressure step method, on the other hand, addresses this shortcoming. However, it has been rarely used in studies on gas-liquid-liquid systems [25,133] probably due to its more involving computations. Nevertheless, Correia et al. [25] illustrated that at agitation rates of 600 and 800 rpm both methods gave $K_L a'$ values within 18% of each other as the medium was still sufficiently coalescing (sufficient mixing in gas phase). Thus, the $K_L a'$ values at these agitations rates were considered as illustrated in Figure 3.3

.

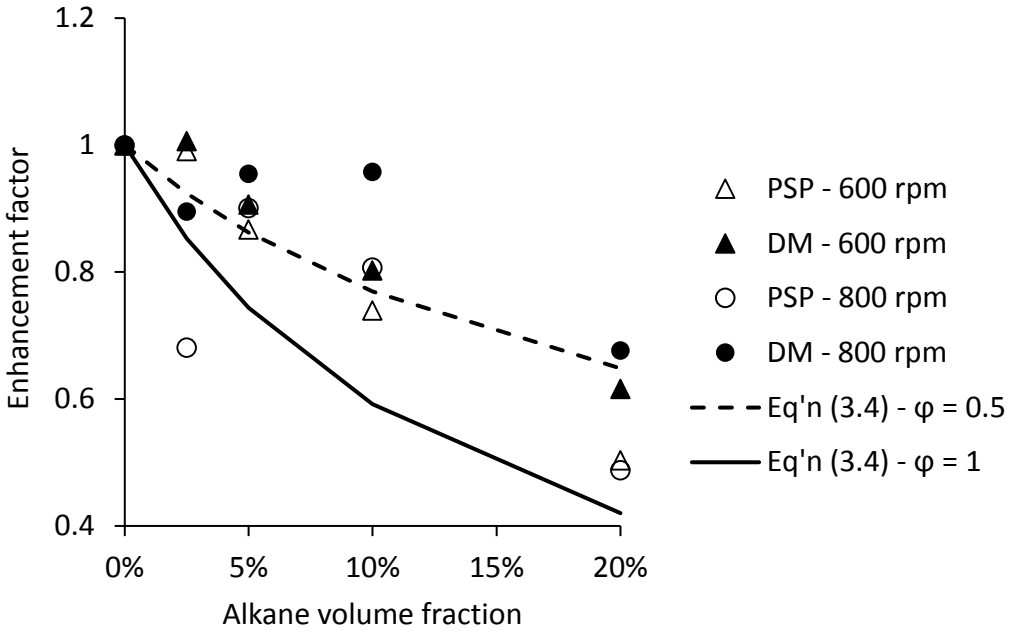

Figure 3.3: Predicted and experimental enhancement factors versus volume fraction of alkanes. PSP – pressure step method, DM – dynamic gassing-out method. See also Gakingo et al. [123].

It can be observed that there was a general decrease in the measured $K_L a'$ values. This was in line with the predicted trend based on equation (3.4), that is, series mass transfer (with or without shuttling). The case of parallel mass transfer was deemed as not appropriate given that the oxygen diffusion coefficients in water and alkane (n-C_{10}-C_{13}) were expected to be of the same order of magnitude. This, in addition to the fact the solubility ratio was greater than 1, implied that an enhancement in $K_L a'$ values would occur for parallel mass transfer (see right-side of Figure 3.1 with $m\sqrt{D_r} \geq 1$) [175].

As previously noted, the experimental results were more closely approximated by equation (3.4). This was particularly true for the case with the exponent φ set to 0.5 (series mass transfer with shuttling). For results by the pressure step method, deviations from the predicted trend were within 7% with the exception of the data points at 2.5% and 20% alkane volume fractions ($\approx$ 25% deviation). For results by the dynamic gassing-out method, on the other hand, deviations were within 10% of the predicted trend with the exception of the data point at 10% alkane volume fraction (25% deviation).

The above results supported the hypothesised model (equation (3.2)). Furthermore, noted differences between the experimental and predicted values were probably due to factors not

accounted for at this stage. These included probable changes to, for example, the interfacial area and energy dissipation rate. These changes can be investigated based on the CFD technique and this is shown in later chapters.

3.4 Summary

The work done in this chapter contributes to current knowledge by highlighting the importance of accounting for the solubility effect in the modelling of the overall volumetric mass transfer coefficient ($K_L a'$). This effect arises from an increase in the absorption capacity of a liquid-liquid mixture which leads to longer saturation times. This effect can be registered as an apparent decrease in the measured $K_L a'$ values and it can mask the influence of other effects of the secondary liquid phase (shuttling for example). The consideration of a case study of oxygen transfer in a cell-free alkane-based reactor has shown that this effect can explain the deviation between observed experimental trends and traditional theoretical models. However, the applicability of this proposition should be generalised by the consideration of other experimental data available in literature. This has not been done at present since the scope of this work was limited to modelling oxygen transfer for alkane biocatalysis.

4.0 CFD model for alkane-based systems

This chapter presents the development of the Computational Fluid Dynamics (CFD) model for the systems considered. As the model was developed in a multi-stage approach in line with objectives 2, 3, 4 and 7, the presentation herein has followed a similar structure. The initial focus of the chapter is on the modelling rationale as well as the governing equations of multiphase flow. Thereafter, the specifics of the 2-phase gas-liquid, 3-phase gas-liquid-liquid and 4-phase gas-liquid-liquid-solid systems are given. Also included is a presentation on the modelling of oxygen transfer as well as the numerical implementation of the CFD model.

4.1 Modelling rationale

Computational Fluid Dynamics (CFD) as a simulation tool can be utilised to resolve spatial heterogeneity in features of interest within a bioreactor at any given scale. Such features of interest could include the distribution of bubble or droplet sizes [111], the distribution of the overall volumetric mass transfer coefficient [22] and the identification of oxygen (or substrate) dead-zones within a bioreactor [113]. This is made possible by the fact that CFD provides an approximate solution to the fundamental equations governing fluid flow, that is, the Navier-Stokes equations [101]. In addition, the CFD solutions are provided on a discretised mesh of the bioreactor (domain) and this allows for the capture of spatial heterogeneity [101].

As the CFD simulation of multiphase bioreactors is an area of active research [32,102–109], various techniques/frameworks have emerged to capture the governing physics in the bioreactors. Such frameworks touch on the choice of continuum (or mathematical) description of the phases, the resolution of turbulence in the reactors as well as the resolution of impeller motion among other issues. These frameworks differ in terms of the amount of detail (or physics) captured, with an associated penalty of increasing computational cost for greater detail. This implies a need to make prior selection of an appropriate framework depending on the objectives of the simulation and this process entails a trade-off between the amount of detail captured versus the computational cost depending on resources available.

The continuum (or mathematical) description of a multiphase system can be based on either an Eulerian or Lagrangian framework. The Eulerian framework treats the phases as interpenetrating continua with the assumption that the phases can occupy the same space

relative to their volume fractions [24]. The averaging of the governing equations for flow (Navier-Stokes equations) results in the introduction of interphase momentum exchange terms that need to be modelled as a closure problem [176,177]. Examples of these exchange terms include the drag force, the lift force and the virtual mass force. The Lagrangian framework, on the other hand, involves tracking individual particles (bubbles, droplets, solids) of a phase through a velocity field [176,177]. The velocity field can be specified independently or computed alongside the motion of the particles if there is coupling between the two [177].

The Eulerian framework is normally employed for the continuous aqueous phase whereas for the dispersed phases (air and alkane), either an Eulerian or a Lagrangian description can be utillised [177]. This results in a mixture of frameworks such as the Euler-Euler or the Euler-Lagrangian frameworks for a 2-phase system. The computational cost of the Lagrangian framework scales with the number of particles being tracked [105,177]. Consequently, its application tends to be limited to flows with a small number of particles [105,177]. For a bioreactor with a large number of particles such as that under consideration, this approach quickly becomes unfeasible. Thus, an Eulerian description of the phases involved (air, aqueous, alkane) was adopted in this study.

With the choice of continuum description made, a second consideration was the description of turbulence. Previous experimental work on alkane-based systems has been done in the turbulent regime which is characterised by a tank's Reynolds number, $Re > 10^4$ [14,164,178]. As turbulent flow involves velocity fluctuations on a wide range of length and time scales, a complete description of the same would involve the use of the Direct Numerical Simulation (DNS) technique. This technique solves for flow while taking into account fluctuations at all length and times scales. It has a high computational cost that scales with the cube of the Reynolds number thus leading to its restricted application to low Reynolds number flows [32].

In place of the DNS technique, the Large Eddy Simulation (LES) and the Reynolds-averaged Navier-Stokes (RANS) techniques have been proposed. The former entails a spatial filtering of fluctuations, with the fluctuations above a given grid-scale resolved whereas those at a smaller (sub-grid) scale are approximated [32,177]. The RANS technique, on the other hand, involves the averaging out of the fluctuations to remain with equations for the mean flow [32,177]. While both these techniques represent a simplification to DNS, the LES technique is still able to resolve a great amount of detail. Consequently, it has been advocated for as the

tool of choice for studies in single-phase modelling of stirred reactors [32]. However, in multiphase reactors, the RANS technique remains the practical tool of choice given its lower computational burden (see Table 2.1).

The RANS technique, involving the averaging of the instantaneous Navier-Stokes equations, is usually employed to simulate the mean flow patterns. Fluctuation terms left behind from the averaging procedure (Reynolds' stresses) are either modelled as done with eddy viscosity models or directly solved for as done in the Reynolds stress model (RSM) [32]. The eddy viscosity models approximates the Reynolds' stresses in terms of gradients of the mean velocities. A proportionality constant, the eddy viscosity, arises in this approximation and it is specified in terms of various models such as the standard k–ϵ model (k – turbulent kinetic energy and ϵ – dissipation rate) [32,177]. The Reynolds stress model (RSM), on the other hand, solves directly for the Reynolds' stresses [32].

The RSM, in comparison to eddy viscosity models, is able to better capture complex features of turbulence such as anisotropy which has been observed near the impellers of stirred reactors [32,177,179]. In addition, it is able to better deal with swirl or rotational flows that are characteristic of the vortices that form behind impeller blades [32,177]. This notwithstanding, the RSM is more computationally demanding (seven extra equations in comparison to two for the standard k–ϵ model) [32]. Furthermore, it is known to suffer from convergence (or solution) difficulties [32]. Consequently, though the RSM holds the promise of more accurate simulations, its use needs to be justified based on the aim of the simulations. Given that the aim in this study was to perform an exploratory investigation into the CFD-based modelling of alkane-based systems, the eddy viscosity approach was employed as a first approximation. This was in line with practice in literature [23,24,33,111].

With the turbulence modelling framework chosen, a third consideration was the resolution of the impeller-baffle interaction. The latter is unique to stirred tank reactors since the rotating impellers generate flow that interacts with the stationary baffles (and walls) resulting in complex flow patterns. Several approaches have been proposed to model this interaction such as the black-box or impeller boundary condition approach and the inner-outer approach [32]. More recently, the multiple reference frames (MRF) approach and the sliding mesh (SM) approach have been proposed. The latter have been observed to have good predictive capability and comparable accuracy [32].

The MRF approach is an essentially steady state approach [32] that provides a "snapshot of the flow with the impeller fixed in one position" [103]. Cylindrical sub-domains are defined around the impellers, with the governing flow equations in these sub-domains specified based on a rotating frame of reference. Flow in the remainder of the tank is specified based on a stationary frame of reference [32]. The SM approach, on the other hand, is a transient approach [32]. In it, flow in the whole tank is defined based on a single frame of reference – the stationary frame of reference. However, the cylindrical sub-domains around the impellers are allowed to rotate with the impeller thus mimicking the cyclical passage of impeller blades [32,103]. This rotation is tracked through sliding-grid algorithms thus introducing extra computational cost [32]. Given that both these approaches have been observed to predict the mean flow with similar accuracy [102,103], the MRF approach was adopted for this study due its lower computational cost.

A fourth and final consideration was the treatment of the size distribution of both air bubbles and alkane droplets. This could ideally be done through the use of population balance models (PBM) (see Table 2.1). However, constant particle sizes were employed for the dispersed phases (air and alkane) as a first approximation. This was warranted by the observation that coalescence and breakage kernels (terms) in PBM have been investigated for 2-phase systems (gas-liquid or liquid-liquid) [34] with little work done on testing their accuracy in 3-phase systems. Furthermore, the use of a constant particle size in the 4-phase system was expected to be accurate based on the hypothesis that the presence of the solid phase (cells/organisms) hindered coalescence.

In summary, the above-mentioned considerations/decisions on the modelling approach represented significant but necessary simplifications to the system. With each simplification, there was a general loss of detail in the physics captured. Though this loss of detail was supplemented by the use of appropriate models, the resulting CFD model represented a first approximation to the system. Similarly, oxygen transfer results derived from the CFD model were taken as a first approximation. Though the latter were observed to be reasonable as noted in the subsequent chapters, future studies should look into the relaxation of these simplifications.

4.2 Model equations for the hydrodynamics

An Eulerian framework was employed to describe the simulated phases based on phase-weighted averaging [180]. The equations of conservation of mass and momentum (Navier-Stokes equations) for the multiphase system were as given in equations (4.1) and (4.2) respectively. Equations of flow for the single phase system could be recovered from these equations [180].

$$\frac{D}{Dt}(\alpha_i \rho_i) = 0 \tag{4.1}$$

$$\frac{D}{Dt}(\alpha_i \rho_i \bar{V}_i) = -\alpha_i \nabla p + \nabla \cdot \bar{\bar{\tau}}_i + \alpha_i \rho_i \bar{g} + \sum_{j=1}^{n} \bar{R}_{ji} + \bar{F}_i \tag{4.2}$$

In the above equations, subscripts i and j represented individual phases (air, aqueous, alkane). The phase volume fraction was represented by α_i, with the sum of the volume fractions of all phases being unity. The density and the mean velocity specific to the phase of interest were represented by ρ_i and $\bar{V}_i$ respectively. The gravitational acceleration vector, with a magnitude of 9.81 m/s^2, was represented by $\bar{g}$ whereas the shared pressure field was represented by p. The Coriolis and centrifugal forces arising from the description of flow using a rotating frame of reference in the MRF approach were represented by $\bar{F}_i$ [180]. On the other hand, the stress tensor accounting for both viscous and turbulent contributions was represented by $\bar{\bar{\tau}}_i$ whereas the interphase interaction forces were represented by $\bar{R}_{ji}$.

In this study, interphase interaction was assumed to only occur between the continuous aqueous phase and the dispersed phases as would be the case for dilute multiphase flow. This simplification was in line with practice in literature [23,24,33,111]. Furthermore, only the drag force was considered though other interaction forces occur such as the virtual mass and the lift force. It has been previously shown that the drag force is the most significant in terms of magnitude and that the gas hold up in the bulk of a stirred reactor is dictated by a balance between the drag and the buoyancy forces [33,35,36]. Consequently, the drag force between phases i and j was modelled by equation (4.3), with the interfacial exchange coefficient (K_{ji}) expanded in terms of the drag coefficient (C_D) and the diameter of the dispersed phase (d_j) (see equation (4.4)).

$$\bar{R}_{ji} = -\bar{R}_{ij} = K_{ji}\left(\overline{\mathbb{V}}_j - \overline{\mathbb{V}}_i\right) \tag{4.3}$$

$$K_{ji} = \frac{3}{4}\alpha_i\alpha_j\rho_i\frac{C_D}{d_j}\left|\overline{\mathbb{V}}_j - \overline{\mathbb{V}}_i\right| \tag{4.4}$$

The stress tensor in equation (4.2) was expanded in terms of the Boussinesq's hypothesis as given in equation (4.5). In this equation, μ_i, $\mu_{t,i}$ and k_i were respectively the molecular viscosity, turbulent viscosity and turbulent kinetic energy (TKE) for phase i while $\bar{\bar{I}}$ represented the identity tensor. The turbulent viscosity of the continuous aqueous phase (denoted by subscript w) was defined in terms of the turbulent kinetic energy (k_w) and its dissipation rate (ϵ_w) as given in equation (4.6). To model the latter parameters, an extension of the single-phase standard k–ϵ turbulence model was employed, that is, the dispersed k–ϵ model (see equations (4.7) – (4.8)). In this model, the standard k–ϵ model equations for the transport, production and dissipation of TKE were used to account for turbulence in the continuous aqueous phase. Additionally, extra terms were introduced to capture the effect of the dispersed phases (Π_{k_w} and Π_{ϵ_w}) [28–31].

$$\bar{\bar{\tau}}_i = \alpha_i(\mu_i + \mu_{t,i})\left(\nabla\overline{\mathbb{V}}_i + \nabla\overline{\mathbb{V}}_i^{\,T}\right) - \frac{2}{3}\alpha_i\left((\mu_i + \mu_{t,i})\nabla\cdot\overline{\mathbb{V}}_i + \rho_i k_i\right)\bar{\bar{I}} \tag{4.5}$$

$$\mu_{t,w} = C_\mu\rho_w\frac{k_w^2}{\epsilon_w} \tag{4.6}$$

$$\frac{D}{Dt}(\alpha_w\rho_w k_w) = \nabla\cdot\left(\alpha_w\left(\mu_w + \frac{\mu_{t,w}}{\sigma_k}\right)\nabla k_w\right) + \alpha_w G_{k,w} - \alpha_w\rho_w\epsilon_w + \alpha_w\rho_w\Pi_{k_w} \tag{4.7}$$

$$\frac{D}{Dt}(\alpha_w\rho_w\epsilon_w) = \nabla\cdot\left(\alpha_w\left(\mu_w + \frac{\mu_{t,w}}{\sigma_\epsilon}\right)\nabla\epsilon_w\right) + \alpha_w\frac{\epsilon_w}{k_w}\left(C_{1\epsilon}G_{k,w} - C_{2\epsilon}\rho_w\epsilon_w\right) + \alpha_w\rho_w\Pi_{\epsilon_w} \tag{4.8}$$

In equations (4.7) and (4.8) above, the production of TKE from gradients of the mean velocity in the continuous phase was captured by $G_{k,w}$. This term is expanded in equation (4.9) wherein the colon symbol (:) represented the double contraction of the velocity gradient tensors [180]. The generation of TKE by the motion of the dispersed phases, on the other hand, was captured by Π_{k_w}. This was expanded in terms of the model by Simonin et al. [28–

30,180] which considers both the mean and the turbulent motion of the dispersed phases in defining the work done due to interfacial forces (see equation (4.10)). It was also assumed that the TKE due to the dispersed phases would be dissipated at a time-scale similar to that of the TKE generated from gradients of the mean velocity [181]. This time-scale of dissipation was captured by Π_{ϵ_w} as given in equation (4.11) [181].

$$G_{k,w} = \mu_{t,w}\left(\nabla\overline{\mathrm{V}_w} + \nabla\overline{\mathrm{V}_w}^{T}\right) : \nabla\overline{\mathrm{V}_w} \tag{4.9}$$

$$\Pi_{k_w} = \frac{\rho_j}{\rho_j + C_{AM}\rho_w} \cdot \frac{K_{jw}}{\alpha_w \rho_w}\left[k_{jw} - 2k_w + \overline{\mathrm{V}}_{dr} \cdot \left(\overline{\mathrm{V}}_j - \overline{\mathrm{V}}_w\right)\right] \tag{4.10}$$

$$\Pi_{\epsilon_w} = C_{3\epsilon}\frac{\epsilon_w}{k_w}\Pi_{k_w} \tag{4.11}$$

In the equations above, the interfacial exchange coefficient between the dispersed and aqueous phases (K_{jw}) was as previously defined (see equation (4.4)). On the other hand, $\overline{\mathrm{V}}_{dr}$ represented the drift velocity or in other words, the diffusion of the dispersed phases due to turbulence. This parameter has been expanded in terms of the gradients of the phases and dispersion tensor $\left(\overline{\overline{\mathrm{D}}}_{jw}\right)$ as illustrated in equation (4.12) [180]. The covariance of fluctuating velocities (k_{jw}) appearing both in equations (4.10) and (4.12) was specified in terms of the TKE in the aqueous phase (k_w) and time-scales of turbulence (τ_{jw}^t, τ_{jw}^F) as specified in equation (4.14) [28–31]. Finally, the constants C_μ , $C_{1\epsilon}$, $C_{2\epsilon}$, σ_k, σ_ϵ, C_{AM} and $C_{3\epsilon}$ took on values as specified in Table 4.1 [180].

$$\overline{\mathrm{V}}_{dr} = -\overline{\overline{\mathrm{D}}}_{jw} \cdot \left(\frac{\nabla\alpha_j}{\alpha_j} - \frac{\nabla\alpha_w}{\alpha_w}\right) \tag{4.12}$$

$$\overline{\overline{\mathrm{D}}}_{jw} = \frac{1}{3}k_{jw}\tau_{jw}^t \tag{4.13}$$

$$k_{jw} = 2k_w\left(\frac{b+\theta_{jw}}{1+\theta_{jw}}\right);\quad b = (1+C_{AM})\left(\frac{\rho_j}{\rho_w}+1\right)^{-1} \text{ and } \quad \theta_{jw} = \frac{\tau_{jw}^t}{\tau_{jw}^F} \tag{4.14}$$

Table 4.1: Constants for model equations [180]

Constants	C_μ	$C_{1\epsilon}$	$C_{2\epsilon}$	σ_k	σ_ϵ	C_{AM}	$C_{3\epsilon}$
Value	0.09	1.44	1.92	1	1.3	0.5	1.2

The turbulence quantities of the dispersed phases were not computed based on equations such as those described above. Rather, they were derived from turbulence quantities of the continuous phase [180]. An extension to Tchen's theory of particle dispersion in homogenous turbulent flows was employed to achieve this [28–31]. In this approach, the turbulence quantities of the particles were computed from the TKE of the continuous aqueous phase (k_w) and time-scales of turbulence [28–31]. An example of this is given in equation (4.15) for the TKE of the dispersed phase (k_j) [28–31]. It is to be noted that this approach was adopted as a first approximation given that this theory was defined for dilute multiphase flows [182].

$$k_j = k_w\left(\frac{b^2+\theta_{jw}}{1+\theta_{jw}}\right);\quad b = (1+C_{AM})\left(\frac{\rho_j}{\rho_w}+1\right)^{-1} \text{ and } \quad \theta_{jw} = \frac{\tau_{jw}^t}{\tau_{jw}^F} \tag{4.15}$$

4.2.1 Gas-liquid system

An estimation of the drag force required the specification of the diameter of the dispersed phase in addition to the drag coefficient (see equations (4.3) and (4.4)). For the 2-phase air-aqueous system, a semi-theoretical correlation was used to obtain the bubble diameter (d_g) as this was not measured experimentally [14]. The correlation given by equation (4.16) was adopted [64,183]. In this correlation, σ_{gw} represented the surface tension with a value of 72 mN/m [132], $\epsilon_{w,ave}$ represented the volume-averaged energy dissipation rate and other terms were as previously defined. Bubble diameters of 3.4 mm (600rpm) and 2.4 mm (800rpm) were obtained from this correlation. Given the close range of predicted bubble diameters, a constant value of 3 mm was employed.

To estimate the drag coefficient, the model by Ishii and Zuber [184] was employed (see equations (4.17) – (4.19)). This model specified the drag coefficient based on the size (thus shape) of the bubbles. For small bubbles of diameter ($d_g \leq 1$ mm) with a typically spherical shape, the drag coefficient ($C_{D,sph}$) was given by equation (4.17) [180]. In this case, Re represented the bubble's Reynolds number. For slightly larger bubbles ($1 < d_g \leq 15$ mm) with a typically ellipsoidal shape, the drag coefficient ($C_{D,ell}$) was given by equation (4.18) [180]. Finally, for bubbles with diameter, $d_g > 15$ mm, and a typically spherical cap shape, the drag coefficient ($C_{D,cap}$) was given by equation (4.19) [180].

$$d_g = 0.7\left(\frac{{\sigma_{gw}}^{0.6}}{{\rho_w}^{0.6}\epsilon_{w,ave}^{0.4}}\right)\left(\frac{\mu_w}{\mu_g}\right)^{0.1} \tag{4.16}$$

$$C_{D,sph} = \frac{24}{Re}(1 + 0.1Re^{0.75}); \quad Re = \frac{\rho_w|\bar{V}_g - \bar{V}_w|d_g}{\mu_{eff}} \text{ and } \mu_{eff} = \frac{\mu_w}{1-\alpha_g} \tag{4.17}$$

$$C_{D,ell} = \frac{2}{3}d_g\left(\frac{|\bar{g}|\,\Delta\rho}{\sigma_{gw}}\right)^{0.5}\left(\frac{1+17.67(1-\alpha_g)^{1.29}}{18.67(1-\alpha_g)^{1.5}}\right)^2 \tag{4.18}$$

$$C_{D,cap} = \frac{8}{3}(1-\alpha_g)^2 \tag{4.19}$$

The model by Ishii and Zuber [184] also accounted for the effect of high volume fraction of the air bubbles on the effective drag. This was particularly relevant for the stirred tank reactor since the gas phase is known to accumulate behind the impeller blades resulting regions of high volume fraction [110]. A higher drag value has been typically observed for the ellipsoidal regime due to a hindrance effect of multiple bubbles (see equation (4.18)) whereas a lower drag value has been typically observed in the spherical cap regime due to the acceleration of bubbles in the wake of preceding bubbles (see equation (4.19)) [184]. The correction terms for these effects in the equations above were expressed in terms of the volume fraction of the gas phase (α_g).

Finally, the impact of freestream turbulence on the effective drag was also considered. This involved the accounting for observations that turbulent eddies interact with particles thus perturbing their motion. This has often been reported to result in a higher drag value [185–189] and various models have been proposed to account for this effect. Such models typically propose correction factors that are related to different measures of turbulence such as the turbulence viscosity, the Kolmogoroff's length scale and turbulence time-scales [33,35,110,185,190]. The model by Lane et al. [110] was adopted as it represented the current state-of-art. This model proposes a correction for the effective drag in terms of the particle's relaxation time (τ_p) and the integral timescale of turbulence (τ_L). This is given in equation (4.20) [110].

$$\frac{C_D}{C_{D,\infty}} = \psi \cdot \left[1 - 1.4\left(\frac{\tau_p}{\tau_L}\right)^{0.7}\exp\left(-0.6\,\frac{\tau_p}{\tau_L}\right)\right]^{-2} \tag{4.20}$$

In the equation above, $C_{D,\infty}$ represented the drag coefficient in a stagnant liquid (equations (4.17) – (4.19)). Furthermore, a tuning constant, ψ, with a value $0 < \psi \leq 1$ was introduced to moderate the effect of this correction factor. This was necessary due to the uncertainty involved in the application of this correlation to the case of large bubbles (d_g = 3 mm) whereas the correlation was derived based on data for small particles (≤ 1 mm) [33,110]. The impact of this tuning constant has been reported in later chapters.

4.2.2 Gas-liquid-liquid system

Two modelling approaches were investigated in the extension of the CFD model from the 2-phase gas-liquid system to the 3-phase gas-liquid-liquid system. The first approach was based on the hypothesis that the alkane phase acts through a change in the effective fluid properties of the system such as density and viscosity [9,170]. Thus, the alkane-aqueous mixture was assumed to be a pseudo-homogeneous liquid. This resulted in an essentially 2-phase system and was referred to as the pseudo-homogeneous Euler-Euler (PH-EE) approach (see Figure 4.1). The second approach, on the other hand, involved the simulation of the three individual phases using the Eulerian framework (see Figure 4.1). This allowed for the assessment of the importance of interfacial interaction terms between the continuous aqueous phase and the dispersed phases (air and alkane). This approach was referred to as the Euler-Euler-Euler approach (EEE).

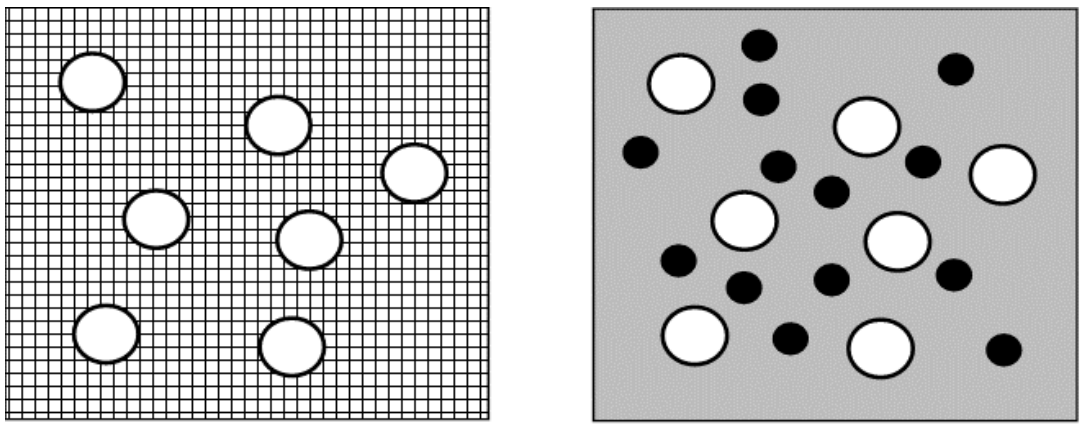

Figure 4.1 (A) The pseudo-homogenous Euler-Euler (PH-EE) modelling approach with empty circles representing the gas phase and the gridded background representing the alkane-aqueous mixture. (B) The Euler-Euler-Euler (EEE) modelling approach with empty circles representing the gas phase, filled circles representing the alkane phase and the grey background representing the aqueous phase. Adapted from Gakingo et al. [191].

For both the PH-EE and the EEE modelling approaches, the interfacial drag was specified based on equations (4.3) and (4.4). For the air-aqueous interfacial drag, the bubble diameter was retained as 3 mm. This represented a slight over-prediction given that Correia at al. [14] measured diameters between 2.9 mm (2.5% alkane) and 2.6mm (20% alkane) at 600 rpm and between 2.5 mm (2.5% alkane) and 2.1 mm (20% alkane) at 800 rpm. The influence of this assumption has been reported on in Chapter 6.0.

With regards to the drag coefficient, equations (4.17) – (4.20) were employed for the air-aqueous interface. Values of the effective density and viscosity were used with these equations for the simulations based on the PH-EE approach. However, for simulations based on the EEE approach, the density and viscosity of water were employed.

Interfacial drag between the aqueous phase and the alkane phase was also considered for simulations based on the EEE approach. In this case, estimates of the diameters of alkane droplets (d_o) were obtained based on equation (4.21) [53]. In this equation, σ_{ow} represented the interfacial tension between the aqueous and the alkane phase with the latter denoted by subscript o. The interfacial tension was assumed to be equal to 40 mN/m [132]. Other parameters considered by this equation included the diameter of the impeller (D_{imp}), the rotational speed (N) and the average volume fraction of the alkane phase ($\alpha_{o,ave}$). Diameters in the range of 50 – 100 µm were obtained. These could not be validated since the diameters of the alkane droplets have not been previously measured [14,164].

The drag coefficient for the alkane-aqueous interface was given by the Schiller-Naumann model that is applicable for small spherical particles with a rigid interface [54]. The model equations were as specified by equations (4.22) and (4.23), with Re being the droplet's Reynolds number. Furthermore, the influence of turbulence on drag was neglected due to the small size of the alkane droplets. This was justified based on experimental observations that the drag force is minimally impacted by turbulence for particles with a diameter $< 10\lambda$, where λ is the Kolmogoroff's length scale [185,186]. A value of 30 µm was computed for the latter based on volume-averaged variables in comparison with a maximum droplet diameter of 100 µm. Thus, the alkane droplet size was lower than the set criteria (10λ) and the impact of turbulence on drag could be neglected.

$$\frac{d_o}{\mathrm{D}_{imp}} = 0.047(1 + 2.5\alpha_{o,ave})\left(\frac{\sigma_{ow}}{\rho_w \mathrm{N}^2 \mathrm{D}_{imp}^3}\right)^{0.6} \tag{4.21}$$

$$C_{D,\infty} = \begin{cases} \frac{24}{Re}(1 + 0.15Re^{0.687}) & Re \leq 1000 \\ 0.44 & Re > 1000 \end{cases} \tag{4.22}$$

$$Re = \frac{\rho_w |\overline{\mathrm{V}}_o - \overline{\mathrm{V}}_w| d_o}{\mu_w} \tag{4.23}$$

4.2.3 Gas-liquid-liquid-solid system

For the 4-phase system, the previously developed 3-phase CFD model was employed with properties modified so as to account for the presence of the yeast cells. Such modifications included, for example, considering a possible change in the effective fluid properties. Given that the alkane phase, similar to the yeast cells, had been previously proposed to affect these properties, it was necessary to examine which of the additional phases had the primary influence.

With regards to the effective viscosity, it was noted that the addition of the alkane phase to the aqueous phase resulted in values of between 1 mPa s (0% alkane) and 1.95 mPa s (20% alkane) [14]. In contrast, the addition of non-viable yeast cells in the range 0 – 3.25 g/L resulted in an insignificant change [192]. This trend was expected to remain valid at yeast concentrations of up to 10 g/L as employed in the validation case studies [164]. Furthermore, investigations into the appropriate modelling approach in the 3-phase system illustrated that the reactor's hydrodynamics were more sensitive to turbulence than to the effective viscosity (see Chapter 6.0). Thus, the influence of the yeast phase on the effective viscosity could be neglected.

With regards to the coalescing behaviour of the medium, the yeast cells were observed to have a greater effect than the alkane phase. Whereas bubble diameters in the gas-liquid-liquid system remained in the range of 2 – 3 mm [14], the bubble diameters in the gas-liquid-liquid-solid system were of the order of $\leq$ 1 mm (see Figure 4.2). It was further observed that the bubble diameters in the 4-phase system could be fitted by an empirical correlation suggested for a 2-phase gas-liquid system with a non-coalescing medium [46] as illustrated in Figure 4.2. The empirical correlation was as given in equation (4.24), with the constant Γ set to 0.0109 instead of 0.014 as originally proposed [46] based on a minimization of the sum of

squared errors. The exponent β, on the other hand, was retained as -0.37 [46]. The relatively good fit of this correlation derived for a 2-phase gas-liquid system suggested that the yeast cells made the medium non-coalescing.

$$d_g = \Gamma \cdot \left(\frac{P_g}{V}\right)^{\beta} \tag{4.24}$$

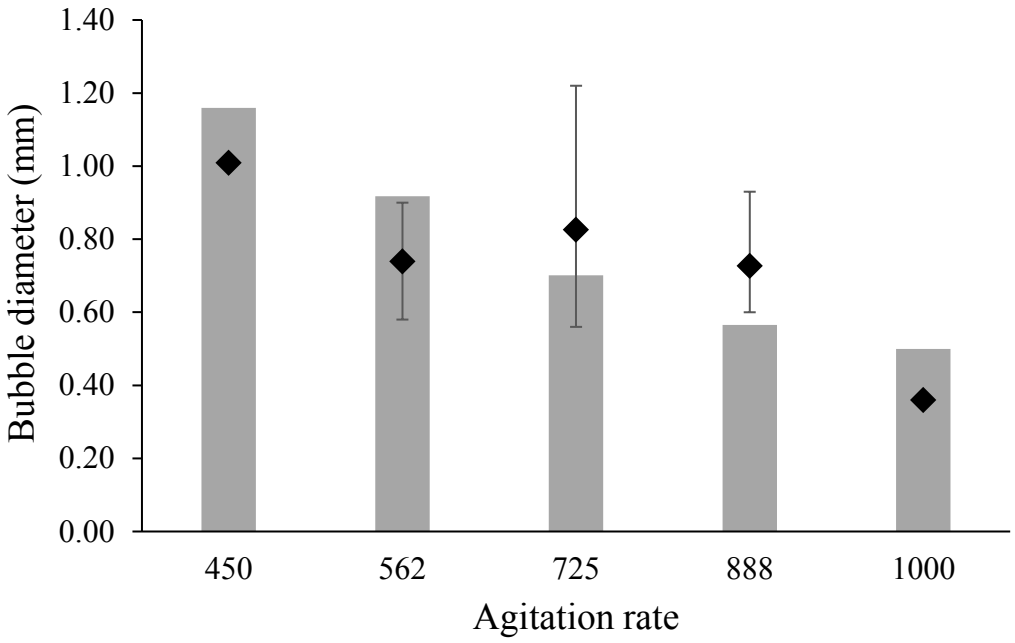

Figure 4.2: Predicted versus experimental bubble diameters. The experimental values (in symbols) represent values averaged over the alkane concentration and yeast loading, with the error bars representing the maximum and minimum values. Adapted from Gakingo et al. [193]

The good fit of bubble diameters to equation (4.24) also suggested that this correlation could be used as a first approximation in the modelling of such 4-phase systems. Such a use of this equation would be advantageous in that it would preclude the need for a prior knowledge of the bubble diameters. Consequently, equation (4.24) was adopted for further simulations. It must be noted, however, that this equation was only sensitive to changes in the agitation rate (through the P_g/V term). It did not account for the changes in the yeast loading or the alkane concentration. Given that the impact of the alkane concentration on the bubble diameter was expected to be minimal (as reviewed above), this did not present a challenge. However, the inability of the equation to resolve changes in the yeast loading meant that the CFD model would be similarly limited. This has been considered in the analysis presented in Chapter 7.0.

With the bubble diameters for the 4-phase system specified, the next step was to specify the drag coefficient at the air-aqueous interface. The latter was given as shown in equation (4.25). In this equation, $C_{D,\infty}$ was given by Schiller Naumann model due to the small size of the air bubbles. This model has been previously specified in equations (4.22) and (4.23). However, in these equations, the values of the alkane phase diameter (d_o) and velocity ($\overline{V}_o$) were replaced with those of the gas phase.

$$\frac{C_D}{C_{D,\infty}} = f\left(\frac{\tau_p}{\tau_L}\right) \cdot g(\alpha_g) \tag{4.25}$$

$$g(\alpha_g) = \exp(3.64\alpha_g) + \alpha_g^{0.864} \tag{4.26}$$

The drag coefficient was also modified to account for the effect of turbulence and high gas volume fraction. As pertains the effect of turbulence, the model by Lane et al. [110] was employed as represented by function $f\left(\tau_p/\tau_L\right)$ (see equation (4.20)). It is to be noted that the constant ψ introduced into equation (4.20) in section 4.2.1 was set to unity since the prevailing bubble sizes were in the order of 1 mm. This was in agreement with the size range for which this model was derived [110].

The effect of high gas volume fraction (α_g) or particle-particle interaction was captured by the function $g(\alpha_g)$ as expanded in equation (4.26) [182,194]. This correlation predicted an increase in effective drag with increase in gas volume fraction. This was based on observations in literature that the motion of small particles tends to be hindered by neighbouring particles [182,194,195] since they (unlike large particles) do not exert a dominating stress field in their immediate neighbourhood [196].

Finally, the droplet diameter and drag coefficient for the alkane-aqueous pair were specified based on the equations given in the previous section (see equations (4.21) – (4.23)). As pertains the droplet size, a lack of experimental measurements [16,164] prevented a proper assessment of the possible influence of the yeast cells at the alkane-aqueous interface. Thus, as a first approximation, equation (4.21) was employed with the interfacial tension retained as 40 mN/m [132]. This gave droplets in the size range of 45 – 120 µm in line with the agitation rates considered. For the drag coefficient, on the other hand, the Schiller-Naumann model [54] was employed given the small size of the alkane droplets.

4.3 Model equations for oxygen transfer

In the modelling of oxygen transfer, a number of simplifying assumptions were made. The first assumption entailed the treatment of the hydrodynamics of the reactor and the oxygen transfer within the reactor as decoupled/independent problems. This was in line with standard experimental procedure where time is allowed for the establishment of hydrodynamics and the equilibrating of the bubble break up and coalescence phenomenon prior to measurements [14]. This assumption allowed for a solution of the spatially distributed phase hold ups and velocity fields in the reactor followed by a solution of the oxygen transfer equations based on the generated information.

The second assumption touched on partitioning of the dissolved oxygen concentration between the alkane phase and aqueous phase in the bulk of the reactor. It was assumed that equilibrium would exist and this could be justified based on the small size of alkane droplets that leads to a high interfacial area and consequently fast mass transfer across these phases [130]. This assumption implied that for a full description of the oxygen transfer problem in the bulk of the reactor, it was sufficient to consider oxygen transfer in only two phases – the gas phase and the aqueous phase. Accordingly, species equations for oxygen transfer were posed as given in equations (4.27) and (4.28).

$$\frac{D}{Dt}(\alpha_w C_w) = -\nabla \cdot (\alpha_w \bar{J}_w) + K_L a'(C_w^* - C_w) \tag{4.27}$$

$$\frac{D}{Dt}\left(\alpha_g C_g\right) = -\nabla \cdot \left(\alpha_g \bar{J}_g\right) - K_L a'(C_w^* - C_w) \tag{4.28}$$

In these equations, C represented the molar concentration of oxygen with subscripts w and g representing the aqueous and gas phases respectively. The total diffusive flux of oxygen comprising of both molecular and turbulent fluxes was represented by $\bar{J}$. The oxygen transfer rate across the gas phase and the aqueous phase was a product of the overall volumetric mass transfer coefficient ($K_L a'$) and the concentration driving force ($C_w^* - C_w$). The overall volumetric mass transfer coefficient was defined based on an assumption of negligible mass transfer resistance in the gas phase (refer to Figure 2.1). This assumption, commonly used in experimental studies, has been recently investigated by Laakkonen et al. [197] for a stirred tank operating at similar power inputs to those used in this work (0.3 – 4.4 W/kg). Laakkonen et al. [197] reported that the gas phase offered minimal resistance to the mass transfer process

despite considering the cases of evaporation of water into the gas bubbles and nitrogen counter-diffusion.

The overall volumetric mass transfer coefficient was also modified to reflect the conditions at the gas-aqueous interface in the presence of additional phases. Possible effects of the additional phases have already been reviewed in Chapter 2.0. In addition, proposed formulations for $K_L a'$ were given in Chapter 3.0 as illustrated in equation (4.29). In the next sections, a further discussion on modelling of the mass transfer process at the interface is given for 2-phase, 3-phase and 4-phase systems respectively.

$$K_L a' \approx E' \cdot K_L a_{\alpha_o=0} = E' \cdot \Lambda \cdot D^{\eta} \left(\frac{\epsilon}{\upsilon}\right)^{\gamma} \cdot \left(\frac{6\alpha_g}{d_g}\right); \qquad \alpha_g < 0.3 \qquad (4.29)$$

4.3.1 Gas-liquid system

In the absence of both the alkane phase and the solid phase, equation (4.29) reduced to the eddy cell model [59]. In this case, the enhancement factor (E') took on a value of unity while the exponents η and γ took on the values 0.5 and 0.25 respectively. The diffusivity of oxygen in the aqueous phase, represented by D, took on the value 2.1 x 10^{-9} m^2/s [175] whereas the constant Λ was set to 0.523 [63].

The definition of the interfacial area (hence $K_L a'$) in equation (4.29) was limited to the bulk of the reactor. This is a region characterised by low volume fraction of the gas phase. Regions of high gas volume fraction ($\alpha_g \rightarrow 1$) also exist and these include areas behind the impeller blades where gas accumulates due to pressure differences [198]. Such regions tend to be characterised by large air bubbles due to increased coalescence [110]. However, the use of a constant bubble diameter (d_g = 3 mm) in the simulations implied that the interfacial area (hence $K_L a'$) would be over-predicted in these regions. To minimise this error, the interfacial area was delineated to regions with $\alpha_g < 0.3$. This value, chosen in line with a previous study [110], was higher than the measured average gas hold up values [14]. Thus, it was expected to represent the larger portion or the bulk of the reactor. This notwithstanding, the impact of this definition has been investigated and is commented on in later chapters.

4.3.2 Gas-liquid-liquid system

The enhancement factor (E') in equation (4.29) was employed to capture two competing factors that the alkane phase can introduce – an enhancement due to new mass transfer pathways and an apparent decrease in the mass transfer rate due to a greater absorption capacity (solubility) of the liquid-liquid mixture. The various possible mass transfer pathways were introduced in Chapter 2.0 and these included parallel mass transfer and series mass transfer (with or without shuttling). Based on an initial examination of experimental data (refer to Chapter 3.0), series mass transfer with shuttling (MT-SS) or without shuttling (MT-S) was seen to be the most likely mass transfer pathway. Consequently, mass transfer at the interface was modelled based on these two scenarios as reflected in equation (4.30). In this equation, the volume fraction of the alkane phase based on the total volume in a gassed reactor (α_o) as opposed to that based on the total volume in an un-gassed reactor as specified in the definition in Chapter 3.0.

$$E' = \frac{1}{(1 + \alpha_o(m-1))^{\varphi}} \tag{4.30}$$

It is to be noted that the choosing between either parallel or series mass transfer pathways represented the choosing of idealised models of what happens at the interface. A more fundamental methodology would have been to numerically solve an advective-diffusion equation at the scale of the gas-liquid interface as has been done by Wenmakers et al. [92]. However, the CFD methodology employed in this study did not resolve the spatial details of the tank down to the scales of the bubbles, droplets and gas-liquid interfaces. This would have been unfeasible given that the objective was to model oxygen transfer in the entire tank. Thus, it was necessary to use idealised models of what happens at the interface.

4.3.3 Gas-liquid-liquid-solid system

For this system, various possible effects of the non-viable yeast cells on the mass transfer process were considered. These included the possible impact of the yeast cells on the effective fluid properties plus the possible interaction of the latter with gas-liquid interface (collision, attachment and detachment). With regards to the effective fluid properties, minimal changes in the effective viscosity (refer to section 4.2.3) and effective diffusivity [83] were observed

given the low cell concentrations used. However, particle-bubble interaction could still have a dominant effect on the mass transfer process. This has been commented on in Chapter 7.0.

4.4 Bioreactor specifications and experimental design

4.4.1 Bioreactor specifications

Three-dimensional simulations of a New Brunswick Bioflo bioreactor were set up and run. Figure 4.3 illustrates a 2D cross-section of this bioreactor and highlights the major components modelled such as the baffles, a ring sparger and two Rushton turbine impellers. Figure 4.3 also illustrates the dimensions of the components considered such as a tank diameter of 177 mm and a tank height of 220 mm. The dimensions and positioning of the impellers have also been given. With regards to the baffles, the latter extended along the vertical walls of the reactor and had a width of 22 mm and a thickness of 1.5 mm. The ring sparger, on the other hand, had an inner and outer diameter of 38 mm and 50 mm respectively and was placed 18 mm above the base of the reactor. It provided aeration at a rate of 0.8 vvm through seven openings of diameter 1 mm each (five on top, two on the bottom side).

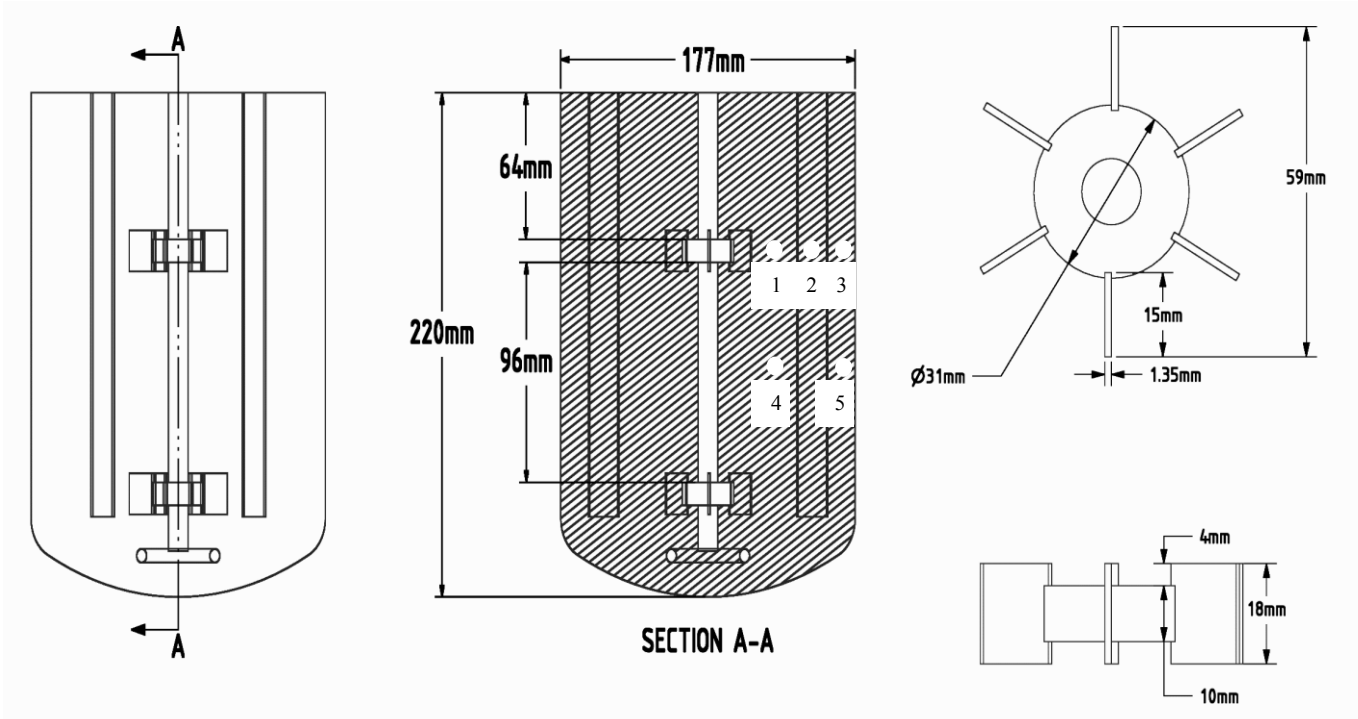

Figure 4.3: Schematic of reactor illustrating cross-sectional details (centre image) plus details of impeller (right-side image). Numbered symbols on cross-section (1 – 5) represent probe points where oxygen concentration was tracked in the simulation. Adapted from Gakingo et al. [193]

4.4.2 Materials

The multiphase medium employed for the gas-liquid-liquid simulations comprised of water (ρ_w = 998 kg/m^3, μ_w = 1 mPa s), air (ρ_g = 1.23 kg/m^3, μ_g = 0.02 mPa s) and an n-$C_{10–13}$ alkane cut (ρ_o = 743 kg/m^3, μ_o = 1.4 mPa s) [14]. For the gas-liquid-liquid-solid simulations, an n-$C_{13–21}$ alkane cut with an estimated density of 752 kg/m^3 and viscosity of 2.74 mPa s [199,200] was employed in addition to the non-viable yeast cells [164]. The diffusivity of oxygen in these alkane cuts was expected to be of the same order of magnitude as that in water [175]. However, oxygen was more soluble in the alkane cuts with the solubility ratio ($m = C_o^*/C_w^*$) estimated to have a value of about 8 [40,175].

Simulations of the 3-phase system by the PH-EE approach necessitated the specification of effective fluid properties. The effective densities (ρ_{eff}) of the alkane-aqueous mixture were obtained by volume-averaging based on the total liquid volume in an un-gassed reactor (see equation (4.31)). On the other hand, the effective viscosities were obtained from measurements performed by Correia et al. [14]. The latter measured the viscosity of pressure-homogenised samples of the mixture using an Anton Paar rheometer [14]. The variation of these fluid properties with alkane concentration is illustrated in Figure 4.4.

$$\rho_{eff} = (1 - x)\rho_w + x\rho_o \tag{4.31}$$

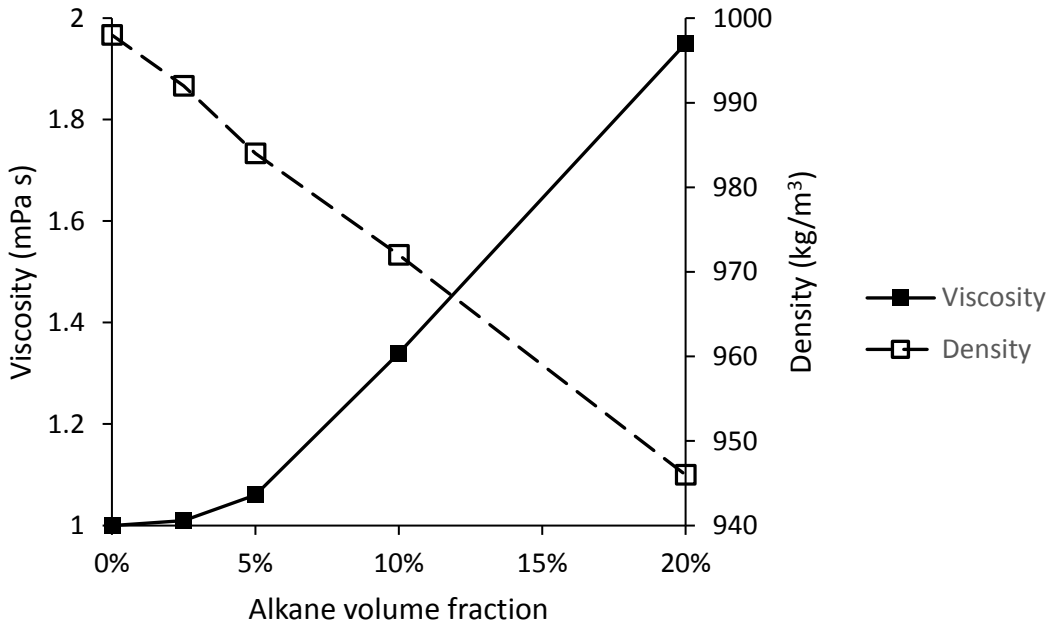

Figure 4.4: Variation of effective fluid properties with alkane concentration [14].

4.4.3 Experimental design

Simulations were run at process conditions similar to those employed in the case studies considered [14,16,164]. For the 3-phase system, the alkane concentration was varied between 0% and 20%, with two agitation rates modelled as illustrated in Table 4.2. Though higher agitation rates were experimentally investigated [14], only those indicated in Table 4.2 were considered since measurements of $K_L a'$ by the pressure step method and the dynamic gassing-out method at these conditions gave values that were within 18% of each other [25]. Given that the $K_L a'$ results by the dynamic gassing-out method are prone to under-prediction [25], the values by this method were used as lower bound estimates in the validation of CFD-predicted values. On the other hand, the $K_L a'$ results by the pressure step method were used as upper bound estimates.

For the 4-phase system, Hollis & Clarke [16,164] employed a central composite design to investigate the influence of process conditions on oxygen transfer. Their experimental conditions were as listed in Table 4.3. Given that these authors [16,164] used the dynamic gassing-out method, their results have been employed as lower bound estimates in the validation of the CFD results as noted in Chapter 7.0.

Table 4.2: Experimental conditions for the 3-phase system [14]

Agitation rate (rpm)	Alkane volume fraction (%)
600	0.0
	2.5
	5.0
	10.0
	20.0
800	0.0
	2.5
	5.0
	10.0
	20.0

Table 4.3: Experimental conditions for the 4-phase system [16,164]

Agitation rate (rpm)	Alkane volume fraction (%)	Yeast loading (g/L)
450	11.0	5.5
561	5.7	2.8
		8.2
	16.4	2.8
		8.2
725	2.0	5.5
	11.0	1.0
		5.5
		10.0
	20.0	5.5
888	5.7	2.8
		8.2
	16.4	2.8
		8.2
1000	11.0	5.5

4.5 Numerical implementation and model validation

4.5.1 Geometry and meshing

The solution domain of the CFD model consisted of the 3D bioreactor with no symmetry assumed. The geometry of the tank was set up using ANSYS DesignModeler package [180]. As illustrated in Figure 4.3, only the major internal components of the reactor were captured. In addition, two cylindrical sub-domains were defined around the impellers (see Figure 4.5). These sub-domains had a radius and thickness that were 1.5 times the respective dimensions of the impellers. In these sub-domains, the equations of flow were defined (and solved for) in a rotating frame of reference. In other regions of the reactor, however, a stationary frame of reference was employed. This was in accordance with the MRF approach to resolving the impeller-baffle interaction.

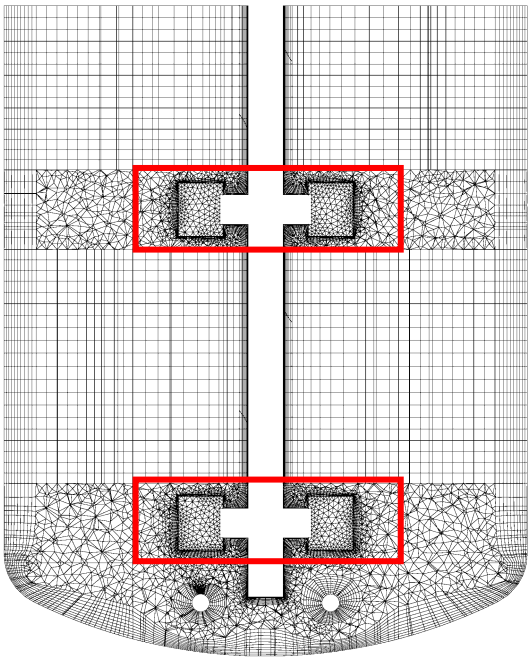

Figure 4.5: Cross-sectional plane illustrating mixed mesh employed (tetrahedrals and hexahedrals). The demarcations with red boundaries illustrate subdomains for the multiple reference frame model.

Once the tank geometry was set up, it was transferred to the ANSYS Meshing package [180] to be discretised or meshed. The objective of this step was to obtain computational cells in which the approximate (numerical) equations of flow would be solved for. The meshing procedure was carried out with a few guiding principles. First, the computational cells were concentrated in the regions of the tank where the highest gradients in velocity were expected. Such regions included the areas near the impellers as illustrated in Figure 4.5. Second, the quality of the computational cells generated was considered since poor quality meshes can contribute to error in the solution process [180]. Metrics such as the cell skewness were employed to assess quality. For the meshes generated (see Chapter 5.0), mean cell skewness values of 0.34 – 0.36 were obtained with an average standard deviation of 0.17 and maximum values of 0.79 – 0.85. These were deemed to be of sufficiently good quality (skewness < 1) [180].

4.5.2 Solver set up and boundary conditions

With the geometry and meshing done, the next step was to set up the solver in the ANSYS Fluent package [180]. This involved the specification of the model equations given in sections 4.2 (for the hydrodynamics) and 4.3 (for oxygen transfer). In addition, the material properties of the phases being simulated as well as the boundary conditions of the domain were specified. With regards to the latter, the solid surfaces of the reactor were treated using the no-slip wall boundary condition. Furthermore, the scalable wall function model was employed to approximate turbulence parameters near these walls.

The top surface of the reactor was modelled differently according to the phases being simulated. For the single phase simulations, it was treated with a free-slip wall boundary condition so as to mimic the interaction of the liquid in the reactor with the air above it. For the multiphase simulations, on the other hand, two approaches were employed to mimic the escape of air through this surface. In the first approach, a velocity-inlet boundary condition was assumed with the normal velocities of the phases fixed. For the gas phase, the normal velocity was approximated by the terminal velocity in a stagnant liquid computed based on the prevailing bubble size [27,33]. This could be justified based on the assumption of low volume fractions of the dispersed phases (air and alkane) near the top surface plus quiescent conditions in these regions that allow for gas bubbles to attain to their terminal velocities [33]. On the other hand, the normal velocity for the aqueous and alkane phases was set to zero given that they did not ideally exit the reactor. This approach was denoted as BC1.

In the second approach, an additional headspace was included at the top of the reactor geometry and this served as a degassing zone. The height of this headspace was fixed at 100 mm and at its top end, a pressure-outlet boundary condition was specified. This was a more accurate representation of gas exit through the top and was denoted as BC2. However, the extra headspace increased the computational expense thus making BC1 more attractive. Differences in terms of the predictions of these two approaches have been assessed and are presented in Chapter 6.0.

As pertains to the gas inlet through the sparger holes, a velocity-inlet boundary condition was employed. In this case, the volume fraction of the gas phase was set to unity. On the other hand, the velocity of the gas phase was computed so as to maintain at total gas flow rate of 0.8 vvm. For the remaining phases, the volume fraction was set to zero.

Finally, the MRF approach was employed to resolve the impeller-baffle interaction. Steady state values (of the mean velocity) were expected based on this approach. However, transient motion was observed to occur. This was characterised by low frequency cyclic motion that was super-imposed on the mean velocity patterns (see Chapter 5.0). The cyclic motion represented transient macro-instabilities that can be generated due to, among other reasons, the configuration of impellers in multi-impeller stirred tank reactors [201–203]. As a result of these observations, time-stepping algorithms were used in conjunction with the MRF approach. This necessitated the specification of initial conditions. The latter included zero velocities for the respective phases with the exception of the gas phase at the inlet, an even distribution of the alkane phase within the reactor and the absence of the gas phase from the reactor. The turbulence equations, on the other hand, were initialized with low values of the turbulent kinetic energy (0.01 m^2/s^2) and its dissipation rate (0.001 m^2/s^3) [204].

4.5.3 Solution procedure

With the solver set up as previously specified, it was necessary to select the discretisation technique for the spatial and temporal terms in the equations of flow. With regards to the single phase simulations, the convective spatial terms were resolved with a second order upwind scheme [180] for the momentum equations whereas a power law scheme [180] was used for the turbulence equations. For the multiphase simulations, on the other hand, a first order upwind scheme [180] was employed. The gave greater stability to the solution process though it was not as accurate as second order schemes. As pertains the diffusive spatial terms, a Green-Gauss node based scheme was employed for all simulations thus giving second order accuracy [180].

With regards to time-stepping, a bounded second order implicit scheme [180] was employed for the single phase simulations. However, for the multiphase simulations, a first order implicit scheme was employed giving greater stability [180]. Time-steps of 0.001s and 0.01s were employed for the hydrodynamics and oxygen transfer equations respectively. A larger time-step was employed for the oxygen transfer problem since its simulations ran for a longer duration (250 seconds in comparison to 10 – 30 seconds for the hydrodynamics). It is to be noted that the hydrodynamics and oxygen transfer problems were treated as independent/decoupled problems. Consequently, different time-steps could be employed for the two problems without affecting the overall solution.

The discretised systems of equations were solved on the Stellenbosch University High Performance Computing cluster [205]. The SIMPLE (single phase) and PC-SIMPLE (multiphase) algorithms were employed [180]. Convergence of the solution process was examined based on the residuals, an overall balance of the gas inlet and outlet and the time evolution of volume-averaged variables such as the gas hold up.

As pertains the residuals, convergence was generally assumed to occur when the residuals dropped to less than 10^{-3}. However, for single phase simulations, the residuals dropped quickly after the initial time steps and could attain values as low as 10^{-6}. Thus, to permit for greater convergence in single phase simulations, the residuals' check was turned off and a maximum of 15 iterations/timestep was enforced. For the multiphase simulations, on the other hand, the residuals of the continuity (mass) equations remained in the order $O(10^{-4})$ after the initial time-steps whereas the residuals for other equations were at least an order of magnitude lower. For the oxygen transfer equations, the residuals were observed to attain values as low as or lower than 10^{-6}.

4.5.4 Validation

The implemented model was validated by assessing it against both hydrodynamic and oxygen transfer parameters. In the single phase and 2-phase systems, the hydrodynamics were assessed based on the non-dimensionalised power and pumping numbers for which established values could be obtained from literature. The power number (N_P) represented the power input through the impeller action whereas the pumping number (N_q) represented the pumping capacity of the impellers. The computation of these numbers was as given in equations (4.32) and (4.33). In these equations, the impeller diameter and rotational speed were represented by D_{imp} and N respectively. Furthermore, the torque on the impellers and the radial mean velocity of the aqueous phase were represented by M and $\vec{V}_{w,rad}$ respectively. The integration in equation (4.33) was performed over height of the impeller (h), with r referring to its radial dimensions. Other terms were as previously defined.

$$N_P = \frac{\mathrm{P}}{\rho_w \mathrm{N}^3 \mathrm{D}_{imp}^5}; \quad \mathrm{P} = 2\pi \mathrm{NM} \tag{4.32}$$

$$N_q = \frac{\int_{-h/2}^{h/2} \alpha_w 2\pi r \bar{V}_{w,rad} dz}{\mathrm{ND}_{imp}^3} \tag{4.33}$$

With regards to oxygen transfer in the multiphase systems, validation was done by considering the gas hold up and $K_L a'$ values. Experimental measurements of these values had been previously obtained by the dispersion height technique (gas hold up) and either the dynamic gassing-out method or the pressure step method ($K_L a'$) [14,16,164]. These experimental values represented global (or volume-averaged) values. The CFD model, on the other hand, predicted local or spatially distributed values. Thus, to enable comparison, there was a need to generate global values from the CFD-predicted local values.

A volume-averaging approach was employed to generate global gas hold up values from the CFD-predicted local values. For $K_L a'$ values, this approach could be similarly adopted. However, Gimbun et al. [22] have argued that this approach does not take into account the impact of local concentration gradients on the average $K_L a'$ values. These authors recommend the tracking of oxygen concentration in the aqueous phase and the use of a volume-averaged oxygen concentration in conjunction with equation (2.20) (repeated below) to compute the average $K_L a'$ [22]. This is analogous to the analysis performed in experiments employing dissolved oxygen probes (the dynamic gassing-out method).

$$\frac{dC_w}{dt} = K_L a'(C_w^* - C_w) \tag{2.20}$$

The approach proposed by Gimbun et al. [22] was adopted for this study. The oxygen concentration in the aqueous phase was tracked at several points as illustrated by Figure 4.3 (centre image). Both regions of the impeller discharge and the bulk of the reactor were considered. It was observed that the oxygen concentration was similar at these various points due to rapid oxygen transport across the reactor given its scale. In addition, the oxygen concentration data obtained from these points corresponded to the volume-averaged oxygen concentration of the entire tank. Consequently, the analysis of oxygen concentration data from an individual point (point 4 on Figure 4.3 (centre image)) was considered to give a representative/global $K_L a'$ value for the tank. This approach was similar to that employed in the experiments [14,16,164].

5.0 CFD model validation

This chapter presents the results of the development and validation of the CFD model proposed for the single phase and 2-phase gas-liquid systems in line with objectives 2 and 3 of this study. Validation has been carried out by comparing CFD-predicted hydrodynamic and mass transfer parameters to established values in literature. Furthermore, the discussion has highlighted the presence of macro-instabilities (MI) in the flow patterns that were observed based on the use of time-stepping with the MRF technique. The simulation/capture of MIs based on this technique has not been previously reported in literature.

A portion of the results presented in this chapter were communicated in a 2020 paper published in the Biochemical Engineering Journal [191].

5.1 Mesh independence study

As a starting point to the validation process, the CFD model for the single phase system was run on several meshes of consecutively smaller sizes to test whether the results predicted were independent of the mesh size. The meshes generated varied in total cell count from about 400,000 to about 1,200,000 computational cells (see Table 5.1). An increase in cell count represented an increase in accuracy though this was associated with an increase in computational cost. Thus, a secondary objective of this investigation was to identify a mesh that would give reasonable accuracy at reasonable cost. This was necessary given that more computationally intensive multiphase simulations would need to be carried out.

To assess mesh independence, two parameters were monitored. These were the power number (see equation (4.32)) and the volume-averaged energy dissipation rate. The power number was taken as representative of the mean flow in the reactor whereas the energy dissipation rate was taken as a representative of the turbulence. The variation of these parameters with the mesh density is illustrated in Figure 5.1.

Table 5.1: Computational meshes employed during mesh independence study.

Mesh label	**M1**	**M2**	**M3**	**M4**
Total cell count	400,413	552,700	770,054	1,233,722

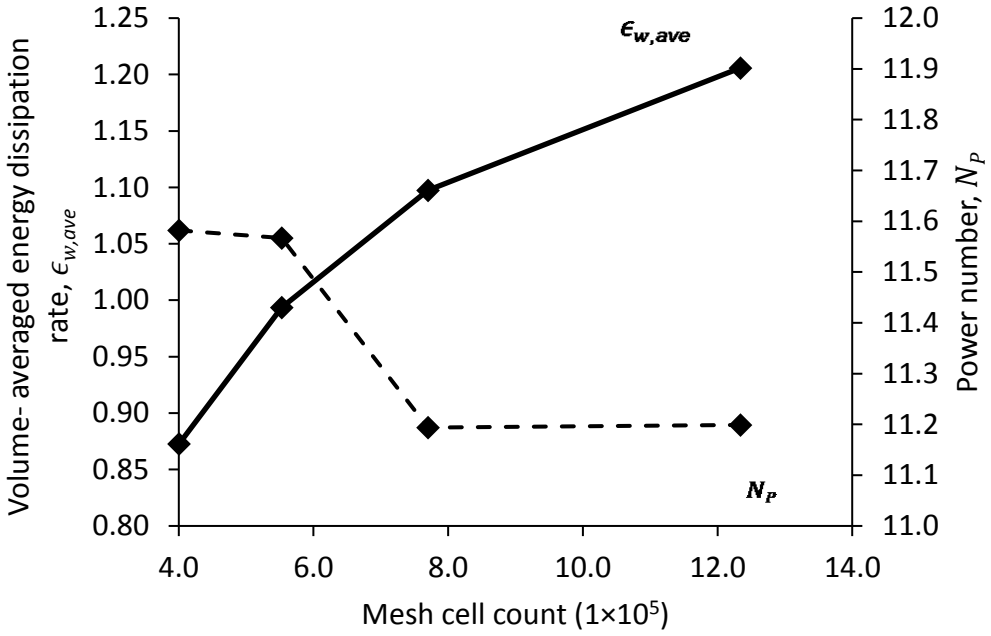

Figure 5.1: Variation of the power number and volume-averaged energy dissipation rate with the mesh density at 600 rpm. Adapted from Gakingo et al. [191].

Figure 5.1 shows that the power number was essentially constant over the range of the mesh densities. A slight drop (3% change) was noted between meshes M2 and M3 but this was considered to be insignificant. The volume-averaged energy dissipation rate ($\epsilon_{w,ave}$), on the other hand, showed greater sensitivity to the variation in mesh density. It was observed that $\epsilon_{w,ave}$ increased with an increase in the total cell count. In particular, $\epsilon_{w,ave}$ increased by 14%, 10% and 10% between meshes M1 and M2, meshes M2 and M3 and meshes M3 and M4 respectively. The change in total cell count between these meshes was approximately 40%, with the exception being between meshes M3 and M4 (60% change in cell count). Thus, it could be concluded that though $\epsilon_{w,ave}$ was increasing with increase in total cell count, the rate of increase was reducing. This implied that at higher mesh densities than those tested, the curve of $\epsilon_{w,ave}$ would flatten out thus achieving true mesh independence.

The above observations were in line with findings in literature. It has been previously reported that the mean flow velocities in a stirred tank can be adequately captured on a coarse mesh [102,103,206]. This explained the observed mesh-independence of the power number. However, $\epsilon_{w,ave}$ was not truly mesh-independent. Rather, finer meshes with total cell counts in the order $O(10^6)$ and above would be required to fully resolve turbulence [102,103,206]. It should be noted, all the same, that the decreasing rate of increase in $\epsilon_{w,ave}$ with increase in

mesh density suggested that the value of $\epsilon_{w,ave}$ as simulated above was approaching its asymptotic limit and therefore this value was reasonably accurate.

To arrive at a compromise between accuracy and computational cost, mesh M3 was adopted. With this mesh, hydrodynamic simulations of the 3-phase system would take on average 2 weeks (real time) for 10 seconds (simulation time) on a 48-core, 40 GB RAM machine [205]. For single phase and 2-phase simulations, shorter time periods were required.

5.2 Single-phase system

The mean velocities obtained for the single phase system illustrated periodic variation that was indicative of macro-instabilities (MI) in the flow pattern. Figure 5.2 and Figure 5.3 illustrate this variation as tracked in the axial velocity at several points in the reactor (refer to Figure 4.3 (centre image)). Figure 5.2 compares the variation in the upper impeller discharge jet (point 1) and in the bulk (point 4) on a plane at a non-dimensional radius of 0.45. On the other hand, Figure 5.3 compares the variation in the upper impeller discharge jet (point 3) and the bulk (point 5) but on a plane at a non-dimensional radius of 0.90. In both these cases, the radii of the planes were non-dimensionalised with respect to the radius of the tank.

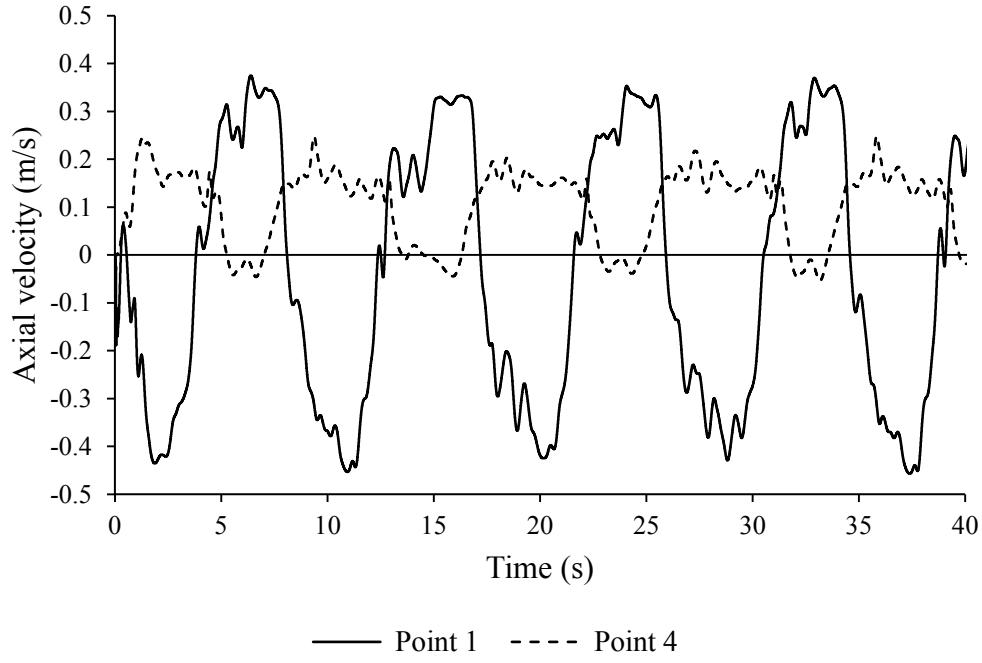

Figure 5.2: Mean axial velocity at 600 rpm. Monitor points are on a mid-baffle plane at a non-dimensionalised radius of 0.45.

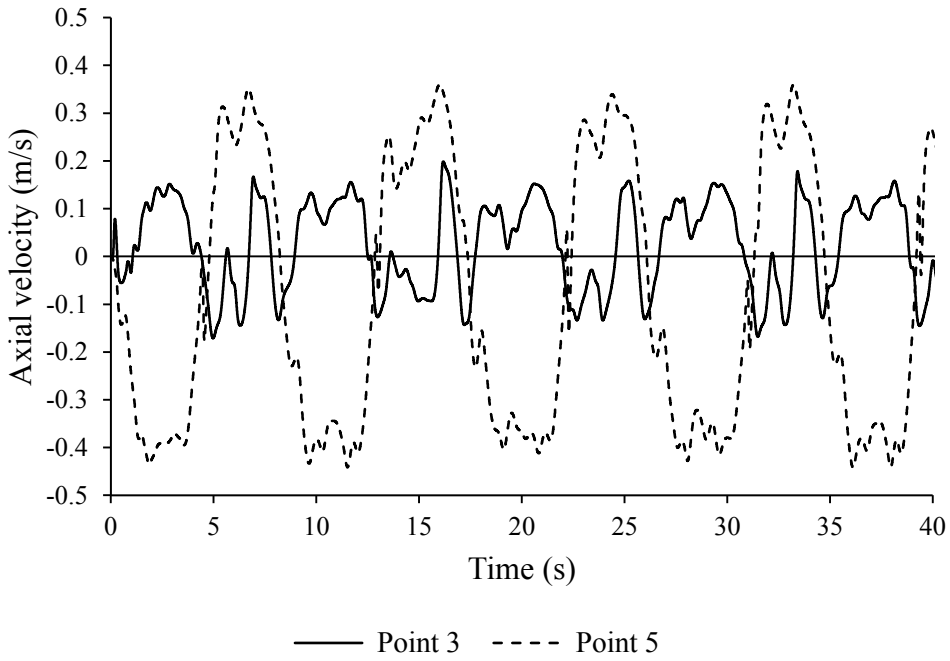

Figure 5.3: Mean axial velocity at 600 rpm. Monitor points are on a mid-baffle at a non-dimensionalised radius of 0.90.

It can be observed from Figure 5.2 and Figure 5.3 that the periodic variation in axial velocity had its highest amplitude near the impeller (point 1) and in the bulk near the wall (point 5). The periodic flow cycles at these points were largely in phase illustrating that the motion was connected, that is, that the MI extended from the impeller region to the bulk of the reactor. Moreover, the cyclic variation near the impeller (point 1) was indicative of "flapping" of the impeller discharge jet, that is, a continuous change in the discharge angle. This could be visually observed in the transient simulations.

The variation at monitor points 3 and 4 had a lower amplitude in comparison to other points. In addition, the variation was out of phase with that of points 5 and 1 respectively. This suggested that the motion at points 3 and 4 consisted of short-lived eddies that sheared off from the main MI motion. In particular, the lack of a clear dominant frequency at point 3 was likely due to a super-position of several of these eddies.

In order to better interpret the observed variation, the axial velocity data was transformed into frequency spectrums using the Fast Fourier transform (FFT) tool in ANSYS Fluent [180]. Figure 5.4 illustrates a sample of the results obtained for monitor points 1 and 4 at 600 rpm. The results obtained indicated that the periodic variation had dominant frequencies of 0.11 Hz (600 rpm) and 0.15 Hz (800 rpm), with dominance judged based on the amplitude as shown in

Figure 5.4. These frequencies corresponded to a non-dimensionalised frequency of 0.011 when non-dimensionalised with respect to the agitation speeds. This value was in line with literature observations where various dominant non-dimensional frequencies have been observed for MIs such as 0.015 – 0.02 [201], 0.02 – 0.06 [207,208] and 0.186 [209,210].

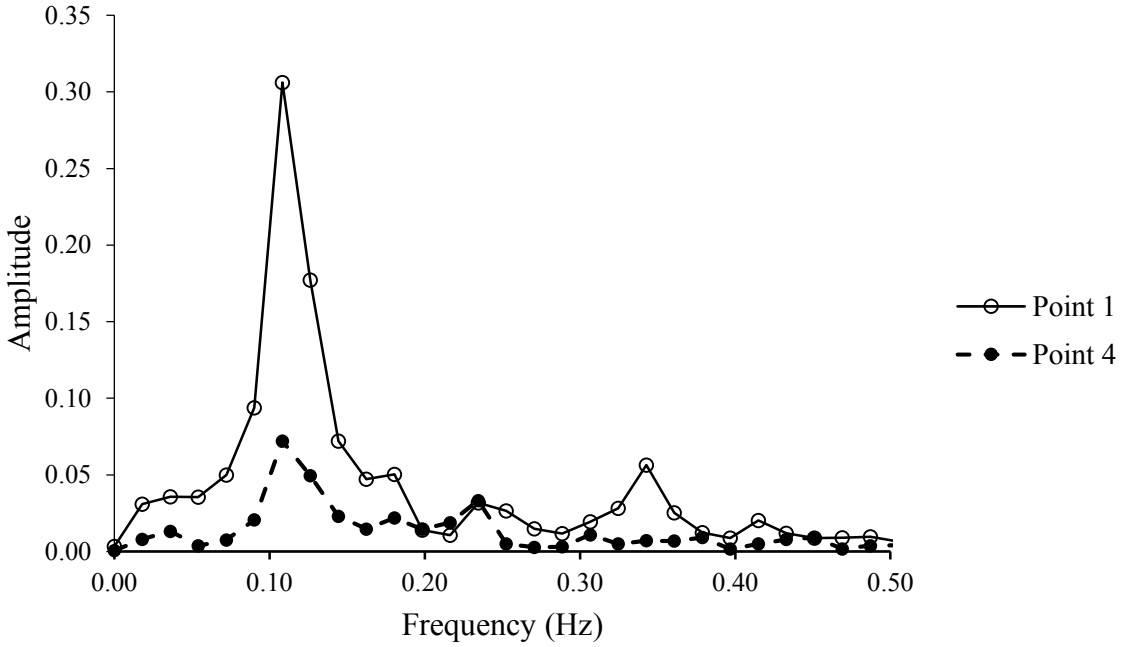

Figure 5.4: Frequency spectrum of axial velocity.

It was interesting to note that MIs were captured based on the MRF technique coupled with time-stepping. This is a first in literature, with previous simulations capturing MIs having employed the sliding mesh technique coupled to either LES [208,210] or RANS [208] for turbulence. The MRF technique, in contrast to the sliding mesh technique, is usually taken as a steady state approach as it provides a "snapshot of the flow with the impellers fixed in one position" [103]. Thus, the capture of MIs by this technique suggested that the latter arose not so much due to the impeller rotation but due to the interaction of the impeller discharge jet with the tank walls as has been suggested by Roussinova et al. [202,210]. These authors have observed that as the impeller discharge jet impinges on the wall, pressure waves are generated and reflected backwards which serve to excite/amplify instabilities in the flow [202,210]. Furthermore, the authors have noted that such a mechanism is geometry-dependent and hence instabilities can be generated at a variety of frequencies [202,210].

For stirred tanks with dual Rushton impellers, it has been observed that both stable (steady) and unstable (transient) mean flow patterns can be obtained depending on the inter-impeller spacing and the value of the off-bottom clearance of the lower impeller [26]. As an example, a

diverging flow pattern has been observed for tanks with a low value of the off-bottom clearance [26]. This flow pattern is characterised by the generation of two circulation loops by the upper impeller whereas the lower impeller generates a single major circulation loop [26]. Such a pattern was observed in the time-averaged (steady) mean velocity as shown in Figure 5.5. Thus, the transient instabilities (MIs) were super-imposed on this time-averaged (steady) flow pattern.

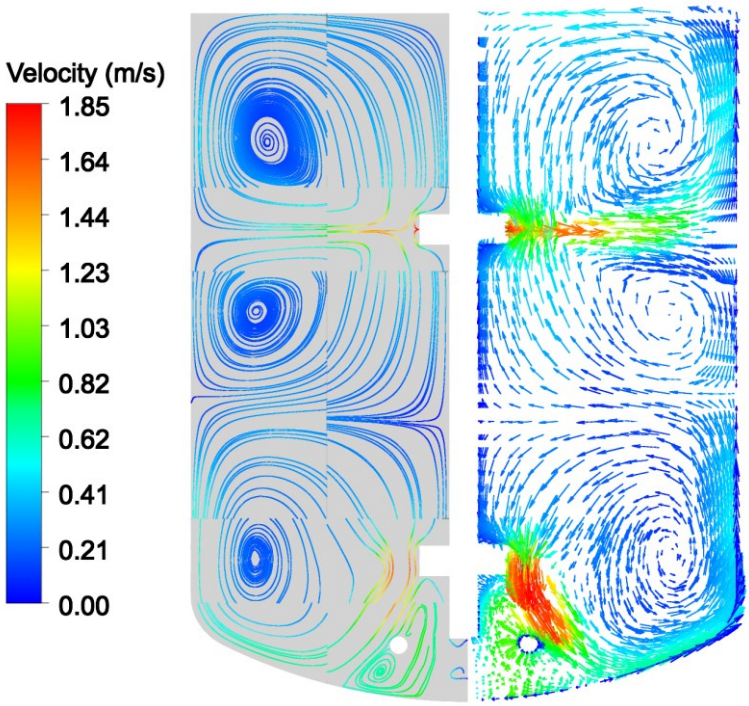

Figure 5.5: Time-averaged mean velocity vectors (right) and streamlines (left) at 600 rpm on a mid-baffle plane.

The presence of MIs was also observed to result in the periodic variation of variables of interest such as the power number and the pumping number. For example, the total power number at both 600 rpm and 800 rpm was observed to oscillate between 10.7 and 11.4, with a time-averaged value of 11.2. This latter value could be compared against a literature value of 9.5 that has been measured for a stable diverging flow pattern in a stirred tank with dual Rushton turbines [26]. In terms of the individual impellers, the upper impeller was observed to have a higher time-averaged power number (7.0) than the lower impeller (4.2) and this trend was in line with observations in literature [211]. However, the power number of the upper impeller (7.0) was greater than that normally cited in literature for Rushton turbines (5.0) [211]. This was probably a result of differences in the size of the impellers modelled. In particular, the impellers had a greater disc thickness-to-impeller diameter ratio (0.17) than is typically reported (≤ 0.05) [211,212].

As noted previously, the pumping number was also observed to oscillate due to the MIs. For the upper impeller; maximum, minimum and time-averaged values of 0.92, 0.88 and 0.91 were respectively obtained. The latter value was in line with what has been reported in literature, that is a value of 0.75 $\pm$0.15 [26,27]. For the lower impeller, on the other hand, low values of the pumping number (0.12 – 0.15) were obtained because the impeller primarily gave an axial discharge (directed towards tank bottom) as opposed to a radial discharge (see Figure 5.5). In the definition of the pumping number according to equation (4.33), only the radial discharge was considered.

5.3 Gas-liquid system

Figure 5.6 presents a comparison of the time-averaged (steady) velocity vectors of the aqueous phase in the single phase and 2-phase system. It can be observed that these profiles were different. In particular, there was a dampening of velocities in the lower impeller region. The lower impeller's discharge jet, which was directed towards the bottom of the tank in the single phase system, now encountered the gas phase which was introduced with an upwards momentum. The interaction of these two phases resulted in a dampening of the associated velocities. Moreover, the angle of the lower impeller's discharge jet as referenced from plane A-A in Figure 5.6 was reduced.

Changes to the upper impeller region were also observed. The discharge jet by the upper impeller was tilted upwards albeit slightly suggesting a lower influence of the gas phase. However, the circulation loops associated with this impeller were more substantially modified. The lower circulation loop was greater in size as demarcated in Figure 5.6 and this was probably the result of reduced interaction with the lower impeller's discharge stream. Additionally, smaller values of velocity were observed near the top surface of the tank. This was probably due to a lower proportion of the upper impeller's discharge stream being directed into the upper circulation loop as compared to the single phase case.

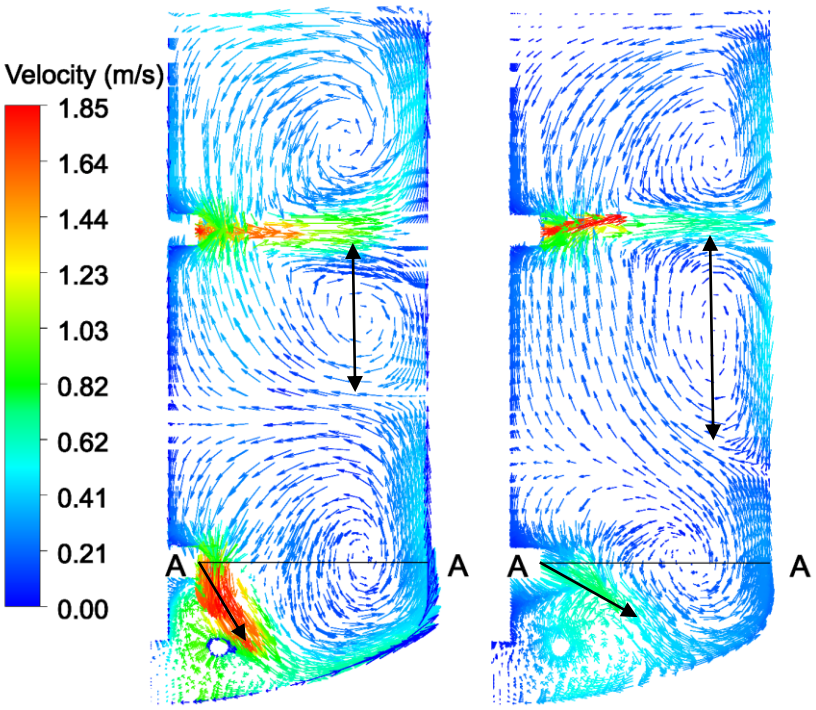

Figure 5.6: Comparison of time-averaged aqueous phase velocities in single phase (left) and 2-phase (right) simulations. Velocity vectors drawn on a mid-baffle plane and capture conditions at 600 rpm. Adapted from Gakingo et al. [191].

The above changes were observed to translate to the associated flow parameters such as the power number and the pumping number. At both 600 rpm and 800 rpm, a time-averaged power number of 5.7 was obtained in comparison to the value of 11.2 reported for the single phase system. This represented a 49% drop in the power drawn. It has been reported in literature that the formation of gas cavities or regions of high gas volume fraction behind the impeller blades (see Figure 5.7) leads to lower power consumption by the impellers [213,214]. Furthermore, empirical correlations have been proposed to predict this decrease in the power drawn. For the setup considered, the correlation by Hughmark [214] predicted a decrease in power of 33% and 35% for 600 rpm and 800 rpm respectively. These values were lower than the CFD-predicted value of 49% but still in the same order of magnitude.

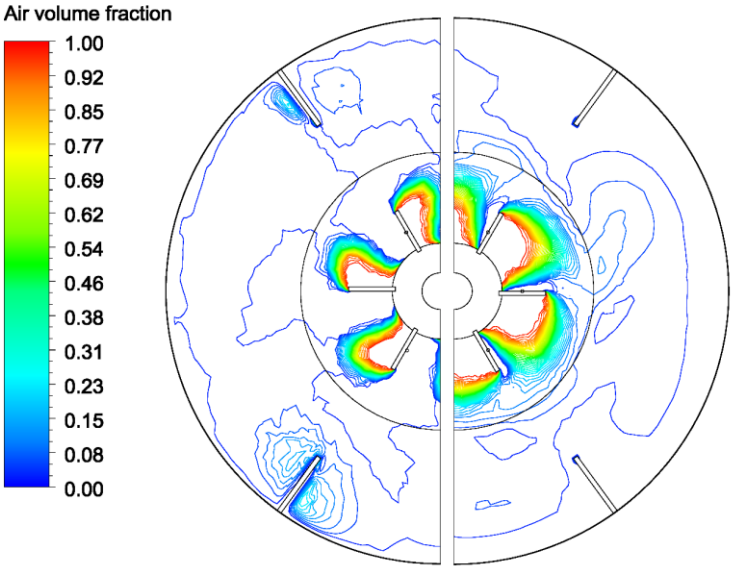

Figure 5.7: Contours of local gas hold up at 600 rpm on horizontal planes passing through the centres of the upper (left) and lower (right) impellers.

With regards to the pumping number, lower values were obtained for the upper impeller. At 600 rpm and 800 rpm, time-averaged values of 0.53 and 0.47 were respectively obtained. These represented a 42% and 48% drop in the pumping number in comparison to that of the single phase system (0.91). As the pumping number was indicative of the pumping capacity, these results illustrated a decrease in the pumping efficiency due to the formation of gas cavities as has been reported in literature [33]. For the lower impeller, however, a slight recovery in the radially-directed portion of the discharge stream (see Figure 5.6) resulted in a recovery of the pumping number (refer to equation (4.33)). Time-averaged values of 0.22 and 0.25 were respectively obtained at 600 rpm and 800 rpm in comparison to a time-averaged value of 0.13 in the single phase case.

For the 2-phase simulations, it was of interest to examine what effects, if any, the previously observed MIs had on mass transfer parameters such as the gas hold up. Figure 5.8 illustrates that the MIs resulted in periodic variation of the gas hold up once pseudo-steady state was achieved. This oscillation was more clearly defined at 800 rpm with the period of oscillation being about 3 seconds (frequency $\cong$ 0.33 Hz). The amplitude of oscillation of the overall gas hold up was about 7% of the steady state gas hold up suggesting an insignificant change. However, fluctuations in the local or spatially distributed gas hold up could have been more significant (see Figure 5.9). The observation of a shorter oscillation period than that observed for velocity oscillations in the single phase case (dominant frequency of 0.15 Hz at 800 rpm)

suggested that flow field modification arising from the presence of an additional phase could alter the MIs. This was further confirmed by the observations of no periodic variation (MIs) in 3-phase simulations by the Euler-Euler-Euler (EEE) approach. In this case, the MIs were dissipated due to a higher turbulent viscosity in the system.

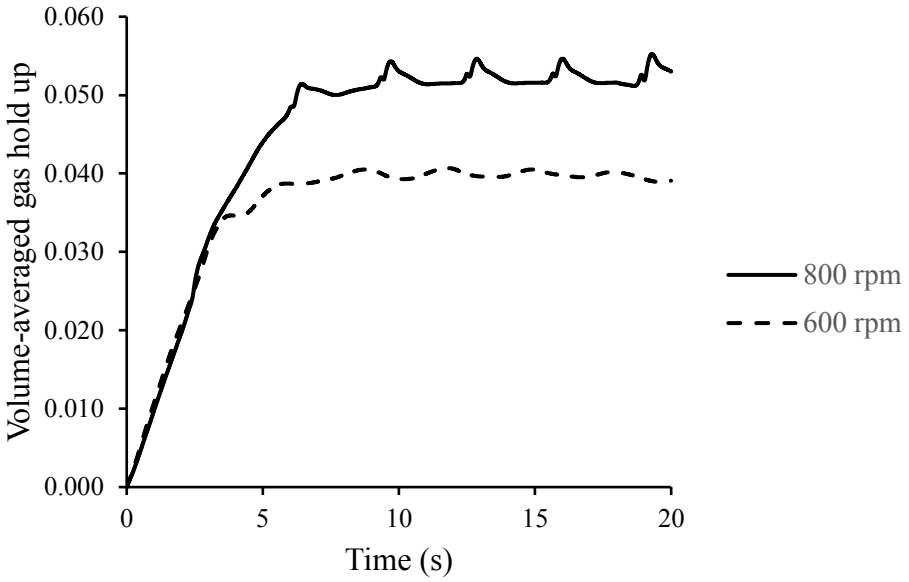

Figure 5.8: Accumulation of volume-averaged gas hold up in tank.

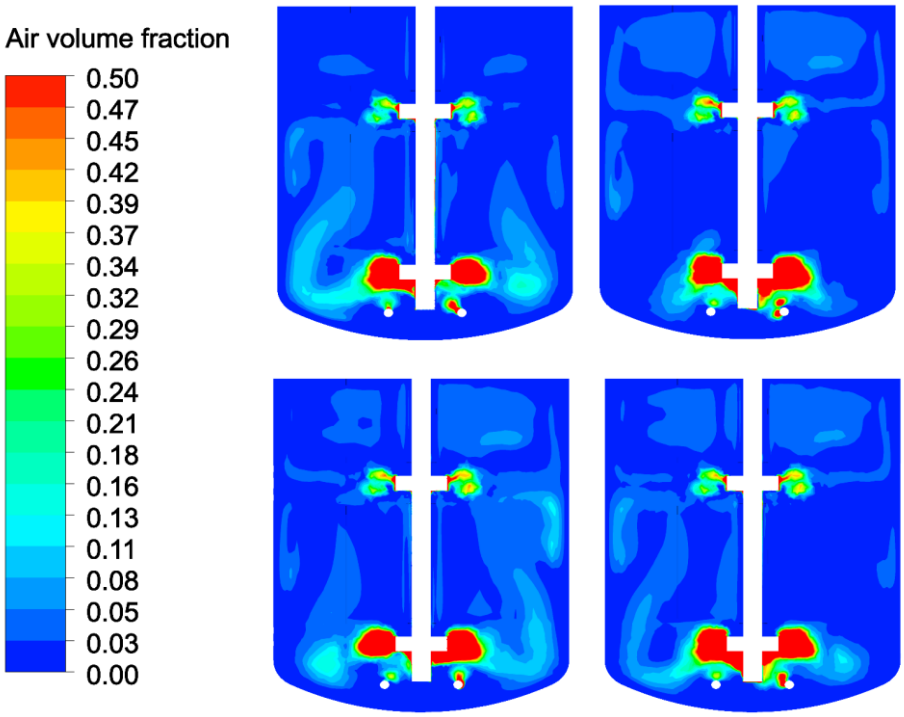

Figure 5.9: Time snapshots of contours of the local gas hold up at 600 rpm. Sequence: top, left then right; bottom, left then right.

The time-averaged gas hold up values were validated by comparing them to experimentally measured values [14]. This is illustrated in Figure 5.10. In this figure, the effect of turbulence on the effective drag and consequently the gas hold up is also included. The figure illustrates that when the effective drag was based on the value in a stagnant liquid ($C_D = C_{D,\infty}$), an under-prediction in gas hold up occurred in line with observations in literature [35,110]. At 600 rpm, the gas hold up was under-predicted by 25% whereas at 800 rpm a greater margin was observed, that is, a 40% under-prediction.

The accounting for the effect of turbulence on the effective drag, on the other hand, led to an over-prediction in gas hold up. The use of equation (4.20) with constant ψ set to unity led to an over-prediction of 60% and 26% at 600 rpm and 800 rpm respectively. Given that equation (4.20) was derived based on data for particles with size ≤ 1 mm, it was hypothesised that the observed over-prediction arose due to the use of this equation on particles with a larger characteristic size (d_g = 3 mm) [33,110]. Consequently, the magnitude of the corrective effect captured by equation (4.20) was reduced by tuning the constant ψ. It was observed that a value of 0.5 gave sufficient results as illustrated in Figure 5.10. This value was retained for subsequent simulations of the 3-phase gas-liquid-liquid system since a similar bubble size was employed (refer to section 4.2.2). However, for the 4-phase gas-liquid-liquid-solid system the prevailing bubble sizes were in the range of 1 mm and thus the constant ψ was set to unity.

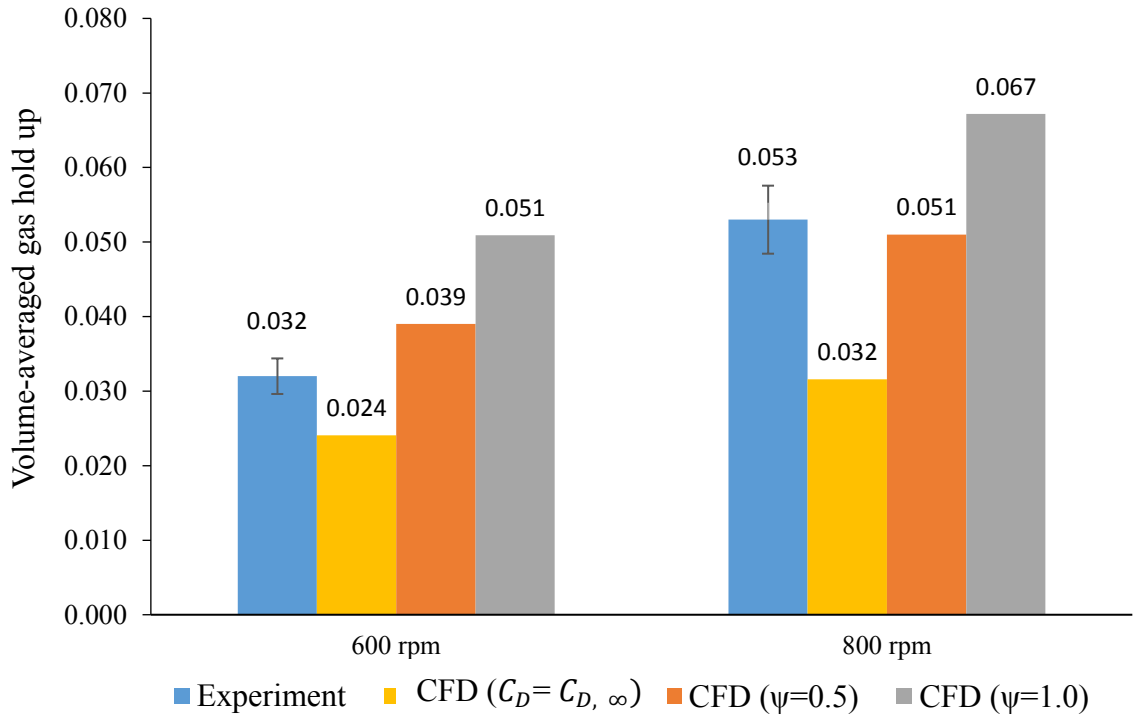

Figure 5.10: Experimental versus CFD-predicted values of the volume-averaged gas hold-up. Adapted from Gakingo et al. [191].

5.4 Summary

The development and validation of CFD model for the single phase and 2-phase systems has revealed several insights that can be applied to future bioreactor design. Foremost, it has been shown that the main features of flow in a stirred tank reactor can be captured based on a CFD model employing a RANS-based approach for turbulence and the MRF technique for impeller-baffle interaction among other simplifying assumptions. The predicted time-averaged flow and its characteristic parameters were observed to be in agreement with findings in literature. For example, a time-averaged power number of 11.2 was obtained for the single phase system in comparison to an experimentally measured value of 9.5. Furthermore, this number dropped to 5.7 in the 2-phase system representing a 49% drop in the power drawn which compared well with empirical modelling of the same (33% – 35% drop in power). In similar fashion, a time-averaged pumping number of 0.91 was obtained for the upper impeller in the single phase and this compared well with experimentally reported values of 0.75 $\pm$0.15. However, for the 2-phase case, this number dropped to values of 0.53 (600 rpm) and 0.47 (800 rpm) representing a drop in the pumping capacity in agreement with findings in literature.

In connection with above, it has also been shown that the gas hold up in a 2-phase system can be adequately predicted by a CFD model using the above-mentioned simplifying assumptions in addition to the assumption of a constant bubble size. However, in this case, it was necessary to adequately account for the effect of turbulence on the effective drag experienced by the gas phase. A failure to consider this effect led to under-predicted gas hold up values whereas accounting for the same based on a correlation representing the current state-of-art resulted in gas hold up values that were accurate to within 22%.

Finally, it has been shown that macro-instabilities (MI) in the flow of stirred tank reactors can be captured using the multiple reference frame (MRF) technique with time-stepping. This represented a first in literature given that previous simulations on MIs have relied on using the sliding mesh (SM) technique [208,210]. Besides this, the observation of capture of MIs by the MRF technique was significant since the latter technique offers a lower computational burden in comparison to the SM technique. Thus, future studies on MIs in stirred reactors can be conducted based on the MRF technique instead.

The presence of MIs also raised the interesting question of whether mass transfer would be affected by their presence. Figure 5.8 illustrated that the overall gas hold up oscillated as a result of the MIs. Though the amplitude of oscillation was small for the overall gas hold up, a look at the temporal changes in the local (spatially distributed) gas hold up values suggested that more significant fluctuations could occur locally (see Figure 5.9). This was significant since it implied that micro-organisms in a reactor experiencing MIs could be exposed to fluctuating concentrations of oxygen or substrate thus impacting their productivity.

6.0 Gas-liquid-liquid system

This chapter presents a discussion of both the hydrodynamics and oxygen transfer in the 3-phase alkane-based bioreactor and in so doing addresses itself to objectives 4, 5 and 6 of the study. These objectives included; the identification of the hydrodynamic changes introduced by the alkane phase and their incorporation into a 2-phase CFD model, the prediction of oxygen transfer in the 3-phase system and the validation of the same against experimental measurements.

The findings of this chapter were communicated in a 2020 paper published in the Biochemical Engineering Journal [191].

6.1 Hydrodynamics and gas hold up trends

The influence of the alkane phase on the hydrodynamics of the bioreactor was modelled and investigated on the basis of two hypotheses. The first hypothesis was that the alkane phase would act through a change in the effective fluid properties of the system [9,170]. This resulted in the pseudo-homogeneous Euler-Euler (PH-EE) approach based on treating the alkane-aqueous mixture as a pseudo-homogeneous liquid. The second hypothesis was that the influence of the alkane phase would be through interphase interactions terms. This resulted in the Euler-Euler-Euler (EEE) approach in which the three phases (air, water, alkane) were individually simulated (see Figure 4.1). To assess these hypotheses, the variation in predicted gas hold up was compared to that obtained through experimental measurements. Figure 6.1 and Figure 6.2 illustrate these results.

It can be observed from these figures that the experimental gas hold up values generally decreased with an increase in the volume fraction of the alkane phase. This trend was approximated by the CFD model based on the EEE approach. However, the CFD model based on the PH-EE approach predicted rather constant gas hold-up values. This latter observation suggested that the reactor's hydrodynamics were insensitive to changes in the effective fluid properties (refer to Figure 4.4). This was likely the case since the flow within the bioreactor remained turbulent as evidenced by a volume-averaged viscosity ratio (μ_t/μ_{eff}) of the order $O(10-100)$. Though this ratio decreased with an increase in alkane volume fraction (increase in the effective viscosity, μ_{eff}), the observation that μ_t/μ_{eff} was always greater

than unity confirmed that the hydrodynamics of the reactor were dominated by the turbulence levels (as represented by the turbulent viscosity, μ_t). Thus, it was concluded that the PH-EE approach (and its underlying hypothesis) was inadequate at capturing the changes in hydrodynamics introduced by the alkane phase.

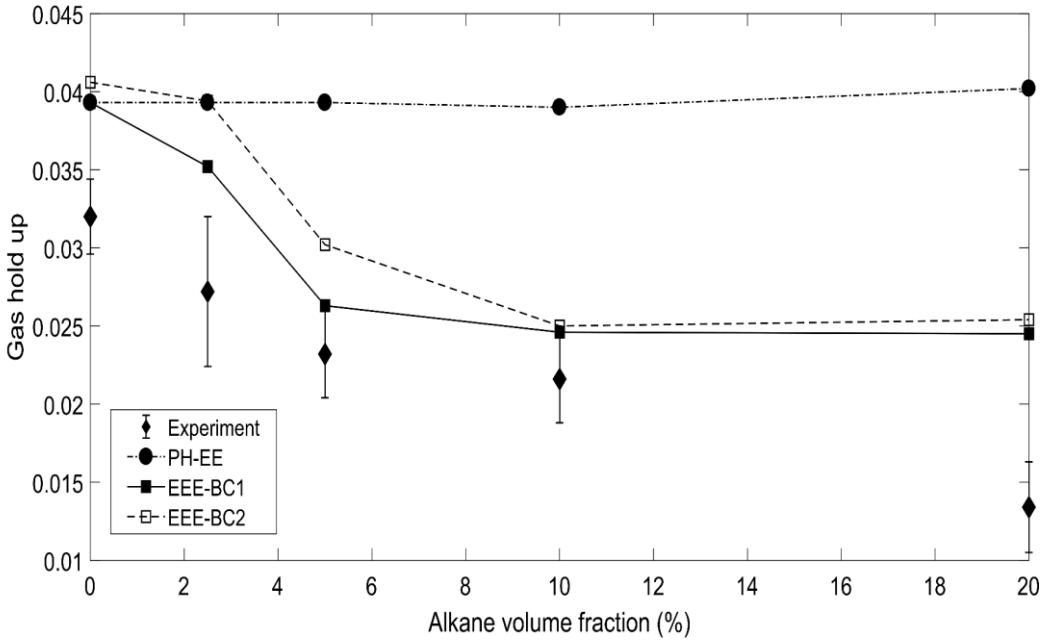

Figure 6.1: Experimental versus CFD-based volume-averaged gas hold-up values at 600 rpm. Reproduced from Gakingo et al. [191].

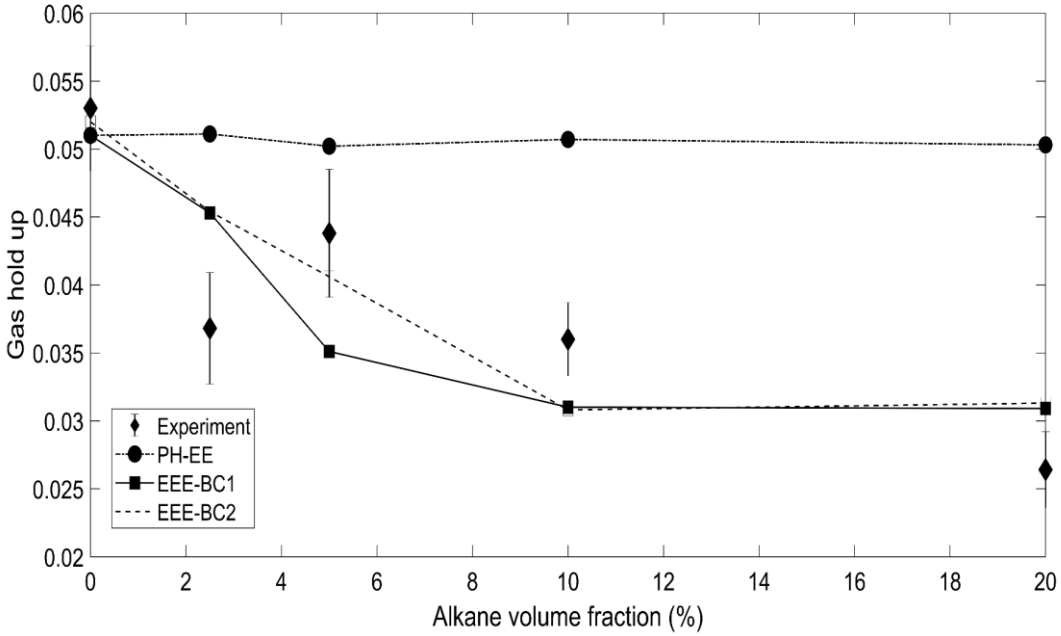

Figure 6.2: Experimental versus CFD-based volume-averaged gas hold-up values at 800 rpm. Reproduced from Gakingo et al. [191].

As already noted, gas hold up values predicted based on the EEE approach approximated the experimentally observed trend. Figure 6.1 and Figure 6.2 illustrate that between 0% and 10% alkane volume fraction, the CFD model predicted a decrease in gas hold up. However, between 10% and 20% alkane volume fraction, the predicted gas hold up remained constant. This trend was replicated for both boundary conditions employed to model gas exit from the top surface of the reactor, that is BC1 (velocity-inlet boundary condition) and BC2 (pressure-outlet boundary condition). Higher gas hold up values were predicted based on BC2 in comparison to BC1, with a maximum difference of 16% observed. This could be attributed to the action of the headspace included at the top surface of the reactor in the BC2 setup serving as a secondary source of the gas phase. Gas was ingested from this headspace in addition to that supplied from the sparger and this led to higher gas hold up values especially at lower alkane concentrations. Given that simulations based on BC1 avoided this effect (due to the absence of the headspace), the subsequent presentation and discussion of results was based on simulations employing this approach.

Gas hold up predictions by the EEE-BC1 approach were generally within 30% of the experimental values. This was especially so in the 0% – 10% alkane volume fraction range where a decrease in the global or volume-averaged gas hold up was predicted (see Figure 6.1 and Figure 6.2). In order to better understand this trend, the changes in the local or spatially distributed gas hold up were assessed. Figure 6.3 gives an example of such an assessment where the local gas hold up in the 2-phase case was compared to that in the 3-phase case at 5% alkane volume fraction. It can be observed from this figure that there were changes to the size of gas cavities formed in the impeller regions (smaller in the 3-phase case). Additionally, there were changes to the degree of gas dispersion within the bulk of the reactor (lower in the 3-phase case).

The lower degree in gas dispersion illustrated in Figure 6.3 could be attributed to changes in the mean velocities of the flow and hence the drag force experienced by the gas phase. Since the drag force was the only modelled means of momentum exchange across the phases (see equations (4.3) and (4.4)), this force was responsible for the dispersing the gas phase within the reactor. In the 3-phase simulations, a lower value of the effective drag was experienced. This arose from reduced mean velocities as illustrated in Figure 6.4.

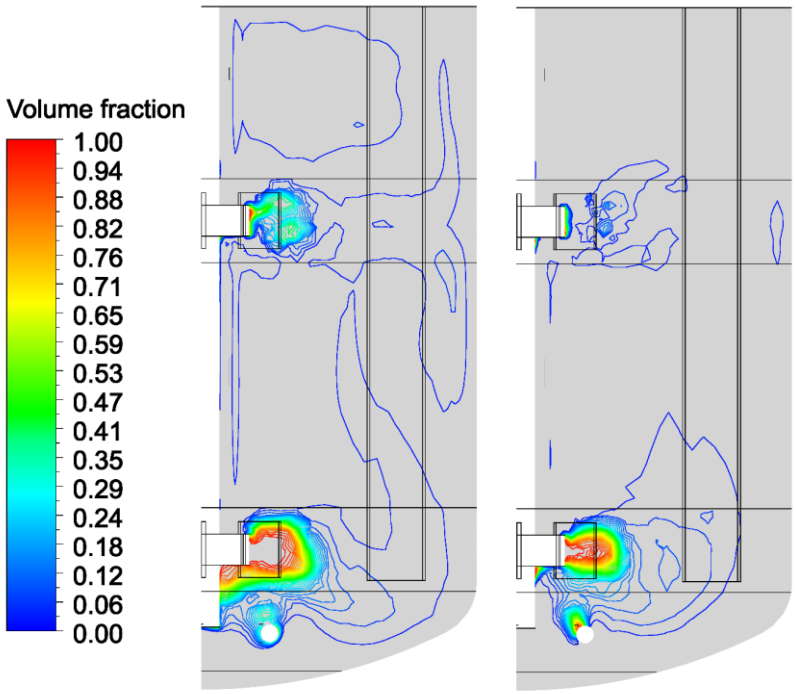

Figure 6.3: Contours of time-averaged local gas hold-up on a mid-baffle plane at 600 rpm. Mesh outlines of the baffles and the impellers are also included. Left – 2-phase case. Right – 3-phase case with 5% alkane volume fraction.

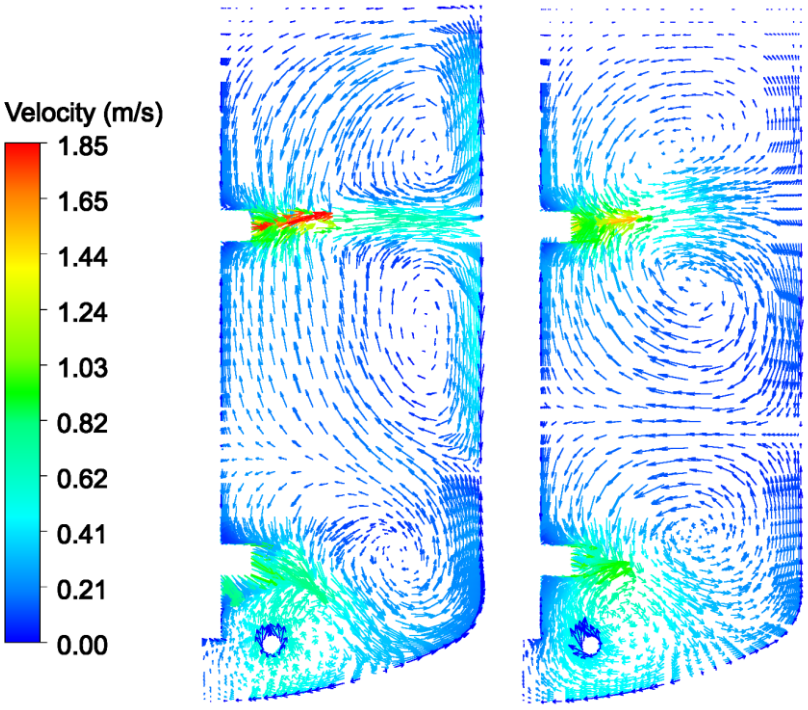

Figure 6.4: Vectors of the time-averaged mean velocities in the aqueous phase on a mid-baffle plane 600 rpm. Left – 2-phase case. Right – 3-phase case with 5% alkane volume fraction. Reproduced from Gakingo et al. [191].

Figure 6.4 illustrates that the discharge jet associated with the upper impeller dissipated quicker for the 3-phase case than for the 2-phase case. Consequently, the circulation loops associated with the upper impeller in the 3-phase case were characterised by smaller velocity magnitudes. This translated to lower gas entrainment (through the drag force) as evidenced by a lack of gas accumulation in the near-wall regions traversed by these circulation loops (see Figure 6.4). In a similar manner, smaller mean velocities associated with the discharge jet of the lower impeller resulted in reduced gas entrainment towards the tank bottom (see Figure 6.4).

The lower degree of gas dispersion could explain the predicted decrease in global gas hold up values between 0% and 10% alkane volume fractions (see Figure 6.1 and Figure 6.2). However, the CFD model predicted an insignificant change in the gas hold up beyond 10% alkane volume fraction. Consequently, over-predictions of 83% and 17% were observed at 20% alkane volume fraction for 600 rpm and 800 rpm respectively. This observation suggested that an additional mechanism was necessary to account for changes in the gas hold up beyond 10% alkane volume fraction.

To address the above, it was hypothesised that the mechanism unaccounted for in the simulations was that of coalescing of air bubbles. This would lead to bubbles of a larger size than that specified (3 mm) and a typically lower residence time [14]. Conditions for such coalescing behaviour were created by the rise of the gas phase through a central core of the reactor due to lower dispersion. The enhanced volume fraction of the gas phase in this region would lead to a higher collision frequency of air bubbles thus promoting the formation of larger bubbles. Furthermore, it was reasoned that such an effect would only be dominant at comparatively low agitation rates whereas at high agitation rates, intensified bubble break up would counter-act this effect. This could account for the higher degree of over-prediction observed at 600 rpm (83%) in comparison to that at 800 rpm (17%).

The rise of the gas phase through the central core of the reactor was also observed to lead to flooding of the impellers by the gas phase. This implied a reduction in the pumping capacity as illustrated in Figure 6.5. This observation was in line with previous reports in literature [171,215]. It should be noted, however, that there was a slight recovery in the pumping number between 2.5% and 5% alkane volume fractions as illustrated in Figure 6.5. This was considered to be due to an initial decrease in the size of the gas cavities behind the impeller

blades (see upper impeller in Figure 6.4). However, at higher values of the alkane volume fraction, flooding began to occur with the subsequent loss of pumping capacity.

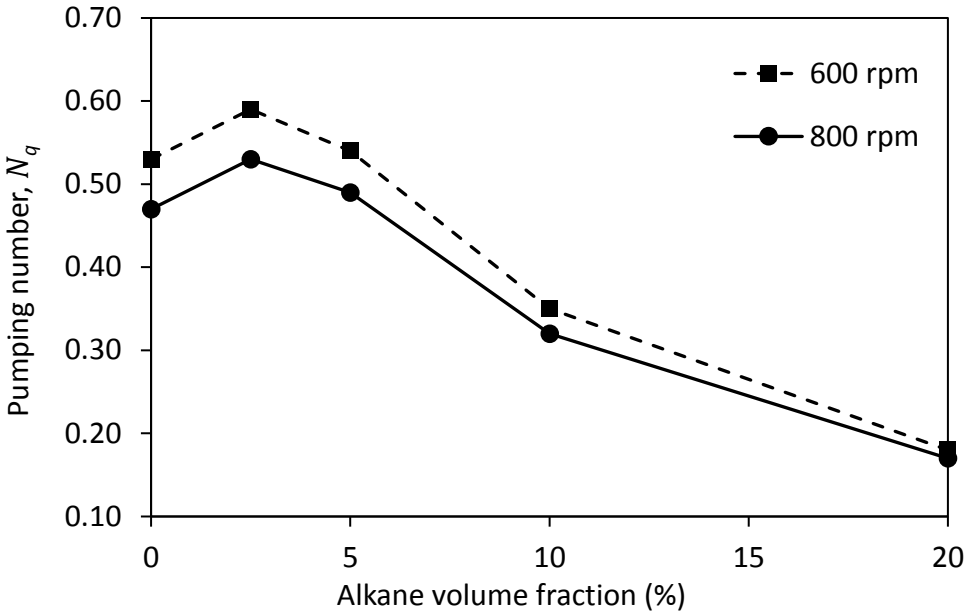

Figure 6.5: Variation of the time-averaged pumping number with the alkane volume fraction for the upper impeller. Reproduced from Gakingo et al. [191].

As a final observation on the hydrodynamics of the system, the influence of the alkane phase on the power drawn by the impellers was investigated. Figure 6.6 illustrates that the power was predicted to increase as the alkane volume fraction increased. A similar trend has been previously reported for a 2-phase liquid-solid system [216]. In the latter study, the authors measured an increase in the power drawn as the solid loading increased and they attributed this to enhanced dissipation by the solid phase [216]. This could be similarly stated for the alkane-based system considered herein. However, it is important to note that observations to the contrary have also been reported in literature [170,217]. In particular, a reduction in the power drawn has been observed for liquid-liquid systems and this was attributed to a reduction in the effective density of the resulting mixture [170,217]. Such contradicting results in literature suggest that this is a point needing further experimental investigations.

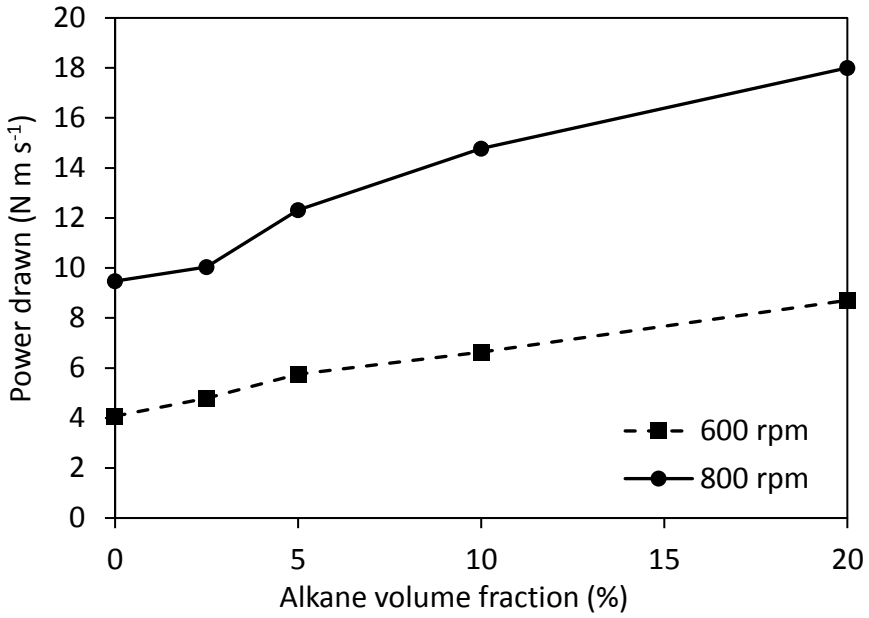

Figure 6.6: Variation of the power drawn by the impellers with the alkane volume fraction.

6.2 Impact of the secondary liquid phase on hydrodynamics

As has been already noted, the lower degree of gas dispersion within the reactor was due to a reduced amount of the effective drag experienced. The latter was itself a consequence of a reduction of mean velocities. This reduction in mean velocities arose due to an increase in turbulent viscosity which is known to have a dampening effect [29]. The turbulence viscosity ($\mu_{t,w}$) increased with an increase in alkane volume fraction giving a volume-averaged turbulence viscosity ratio ($\mu_{t,w}/\mu_w$) of order $O(100-1000)$. This was an indication that the alkane phase had an impact on the turbulence levels in the reactor. The mechanism through which this happened is discussed in further detail below.

Momentum exchange across the phases was captured through the consideration of the drag force. This was modelled by appropriate terms in both the momentum equations (see equations (4.3) and (4.4)) and the turbulent kinetic energy (TKE) equations (see equations (4.7) and (4.8)). The latter were a description of turbulence in the continuous aqueous phase, with the generation and dissipation of TKE by the dispersed phases introduced into these equations through additional terms (see equations (4.10) and (4.11)) [28–30,180]. These terms represented the work done by the drag force and considered both its mean and fluctuating/turbulent components [28–30,180].

Given that the above terms associated with the dispersed phases could be turned on and off in the simulation software, their effects could be isolated and investigated independently. From such an analysis, it was observed that the turbulence levels in the reactor were insignificantly impacted by the gas phase. This was hypothesised to be due to the small density (hence inertia) of the air bubbles. The alkane phase, on the other hand, was found to have an appreciable effect on turbulence. This was chiefly through the fluctuating component of the work done by the drag force. The mean component of this work was expected to be negligible given the small size of the alkane droplets. Small-sized particles have been noted to follow the mean flow of the continuous phase with a relative velocity approaching zero and thus the mean component of the work done by the drag force tends to be negligible [147].

The above consideration of the interaction of the alkane phase with the turbulence of the continuous phase led to higher values of the TKE and its dissipation rate. Consequently, higher values of the turbulent viscosity were obtained (see equation (4.6)). Higher values of the latter led to a greater dampening of the mean velocities with the subsequent effects on the drag and residence time of the gas phase. In addition, there was a dissipation of the macro-instabilities noted in the single phase and 2-phase simulations.

6.3 Oxygen transfer

Oxygen transport within the reactor was modelled on the basis of equations (4.27) and (4.28) (see section 4.3). In addition, the oxygen concentration in the aqueous phase was tracked at several points in the reactor (see Figure 4.3 (centre image)). The values obtained from these points were similar due to rapid convective transport hence only data from a single point in the bulk (point 4) was employed for subsequent analysis. Samples of the oxygen concentration profiles obtained are illustrated in Figure 6.7.

Figure 6.7 presents oxygen transfer results from both the series model (MT-S) and the series model with shuttling (MT-SS). In addition, it contrasts the simulated profiles to experimental oxygen concentration profiles obtained from the dynamic gassing-out method [25]. It can be observed that there was generally good agreement between the simulated and experimental oxygen concentration profiles at 2.5% alkane volume fraction. However, the simulated profiles deviated from their experimental counterparts at 20% alkane volume fraction. This suggested a dependence of the CFD-based oxygen transfer results on the alkane volume fraction. A clearer picture of this is given Figure 6.8 and Figure 6.9 which contrast the

experimental versus predicted $K_L a'$ values for the 600 rpm case and the 800 rpm case respectively.

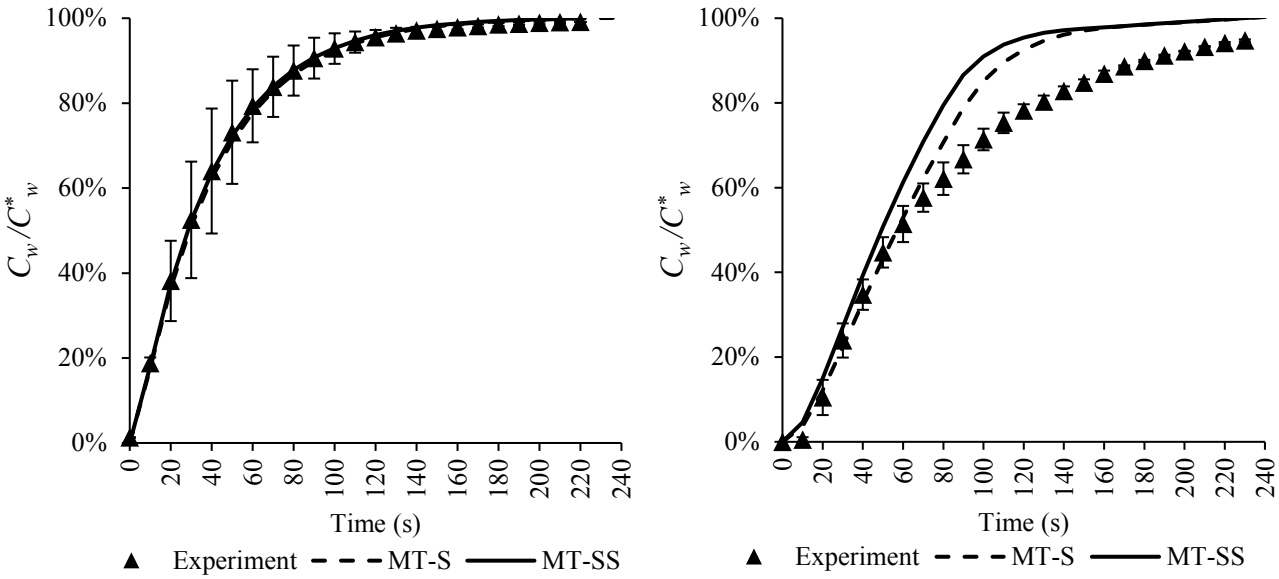

Figure 6.7: Variation of non-dimensionless oxygen concentration profiles with time at 600 rpm and 2.5% (left) or 20% (right) alkane volume fractions. Simulated values based on series mass transfer model (MT-S) and series mass transfer model with shuttling (MT-SS). Adapted from Gakingo et al. [191].

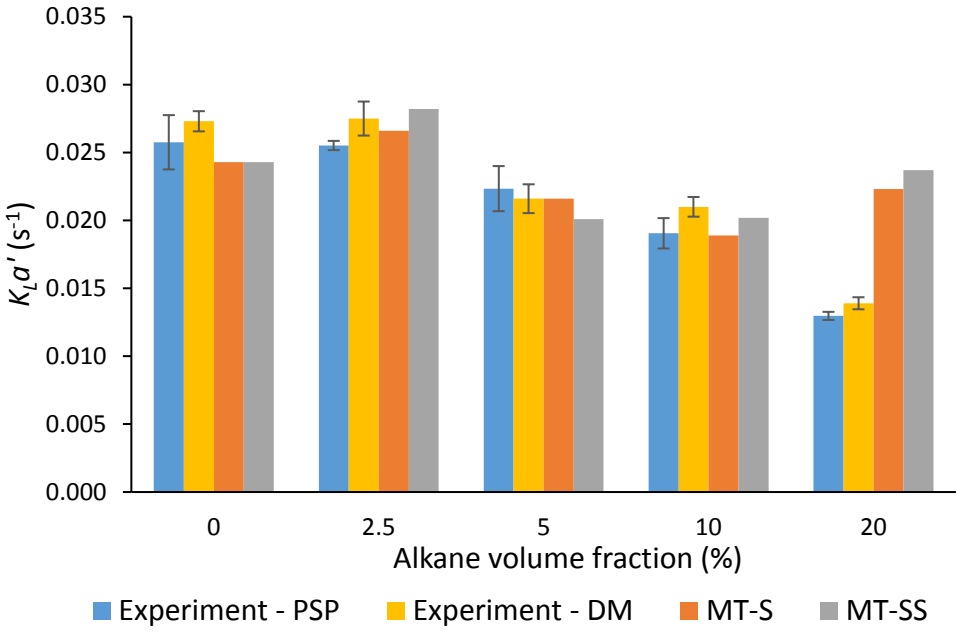

Figure 6.8: Comparison of predicted versus experimental values of $K_L a'$ at 600 rpm. The latter measured by either the pressure step method (PSP) or the dynamic gassing-out method (DM). Adapted from Gakingo et al. [191].

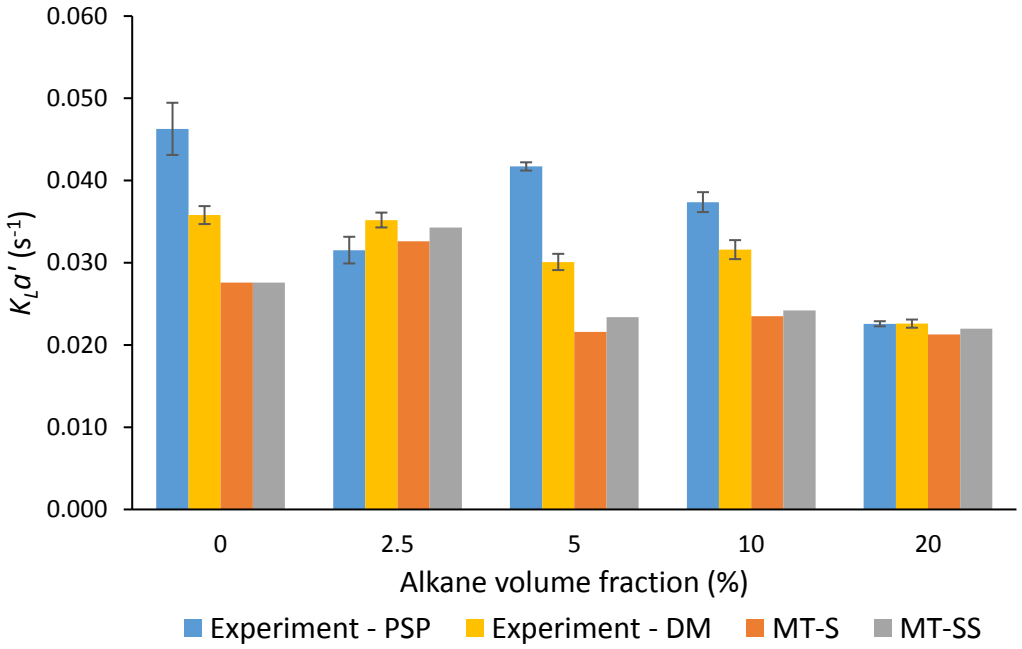

Figure 6.9: Comparison of predicted versus experimental values of $K_L a'$ at 800 rpm. The latter measured by either the pressure step method (PSP) or the dynamic gassing-out method (DM). Adapted from Gakingo et al. [191].

Figure 6.8 and Figure 6.9 compare the predicted $K_L a'$ values to experimental values obtained by two methodologies – the pressure step method (PSP) and the dynamic gassing-out method (DM). The difference between these two methodologies has been previously alluded to where it was noted that the DM tends to under-predict $K_L a'$ values in non-coalescing media [25,42,174] whereas the PSP does not [25,133]. Thus, the DM values were used as the lower-bound estimates in validating the CFD-based values whereas the PSP values were used as upper-bound estimates. A maximum difference of 18% was noted between these experimental values for the agitation rates considered [25].

It can be observed from Figure 6.8 and Figure 6.9 that both the MT-S and the MT-SS models predicted similar $K_L a'$ values, with a maximum difference of 8% noted at 800 rpm and 5% alkane volume fraction (see Figure 6.9). This was contrary to the initial expectation of an increasing difference in the two models with increase in the alkane volume fraction (see Figure 3.3). This observation could be attributed to the computation of global $K_L a'$ values based on a consideration of the concentration driving force (see equation (2.20) in section 4.5.4). The latter served to average out the differences between the two models.

Besides a consideration of the possible changes in oxygen transfer as captured by the MT-S or MT-SS models, the predicted $K_L a'$ values in Figure 6.8 and Figure 6.9 also considered possible changes due to the hydrodynamics. Figure 6.10 illustrates this for the 600 rpm case by contrasting the enhancement factor based on the MT-S model at constant versus varying hydrodynamic conditions. It can be observed that at constant hydrodynamic conditions (no CFD input), a continuously decreasing trend in mass transfer was predicted (see also Figure 3.3). However, incorporation of the changes in hydrodynamics as captured by CFD led to a change in the trend. As the energy dissipation rate increased due to the action of the alkane phase, the $K_L a'$ values increased (see equation (4.29) in section 4.3). On the other hand, a decrease in gas hold up (hence interfacial area) counteracted this effect.

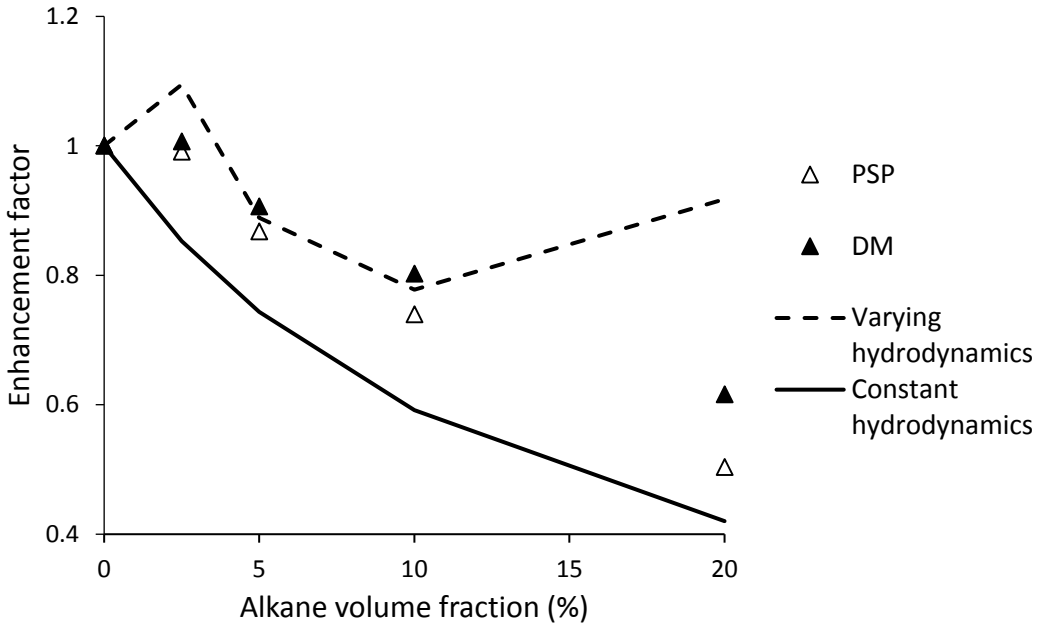

Figure 6.10: Enhancement factor based on MT-S model at 600 rpm with experimental values by the pressure step method (PSP) and the dynamic gassing-out method (DM).

With regards to the accuracy of predicted $K_L a'$ values, it was observed that the predictions at 600 rpm were within 11% of the values measured by the PSP (see Figure 6.8). The exception to this was at 20% alkane volume fraction where over-predictions of 72% and 83% were observed for the MT-S and the MT-SS models respectively (see Figure 6.8 and Figure 6.10). These over-predictions were of a similar order of magnitude as the over-prediction in gas hold up at this experimental point (83%). This suggested that the over-prediction in gas hold up (hence interfacial area) was responsible for the over-prediction in $K_L a'$.

With regards to the 800 rpm case (see Figure 6.9), simulated $K_L a'$ values were within 10% of the values measured by the PSP at only two experimental points – 2.5% and 20% alkane volume fractions. At all other experimental points, under-predictions were observed with the margins being as high as 48% in some cases (5% alkane volume fraction). Taking into account the observation that the gas hold-up values had been generally well predicted (see Figure 6.2), these results implied a need to re-asses the specification of the interfacial area in the model. In particular, the modelling assumptions employed in sections 4.2 and 4.3 were re-examined by modifying them and re-running the oxygen transport equations. The latter included the assumption of a single bubble size for all simulations as well as the assumption that the interfacial area in the bulk region of the reactor could be demarcated based on a gas phase volume fraction of $\alpha_g < 0.3$. It must be highlighted that these assumptions were employed for the 600 rpm case with reasonable success.

Figure 6.11 illustrates the results from the re-examination of the first modelling assumption. In this case, the use of the initially computed bubble diameter of 2.4 mm was compared to the assumed diameter of 3 mm (refer to section 4.2.1). Improvement in the predicted interfacial area (hence $K_L a'$) was noted at low alkane volume fractions ($\leq$5%) with insignificant changes at higher concentrations. The largest improvement was at 0% alkane volume fraction where the $K_L a'$ value with respect to PSP was now under-predicted by 29% in comparison to 40% when a diameter of 3 mm was assumed. However, the $K_L a'$ value at 2.5% alkane volume fraction was now worse off – a 22% over-prediction in comparison to an initial 3%. This notwithstanding, the latter result was deemed to be more accurate and in line with the 23% over-prediction in gas hold up at this point (see Figure 6.2).

With regards to the second assumption, the definition of the interfacial area was extended from regions in the reactor with a gas phase volume fraction of $\alpha_g < 0.3$ to include any regions with $\alpha_g < 0.8$. In addition, the diameter of the air bubbles was maintained at 2.4 mm. Given the arbitrariness in the definition of what constituted the bulk region of the reactor, only a single simulation was run. This was done at 0% alkane volume fraction where the largest sensitivity to changes in bubble diameter had been observed (see Figure 6.11). It was anticipated that this simulation would give a sense of the largest possible improvement.

The results obtained did indeed indicate an improvement. The experimental $K_L a'$ values based on the PSP were now under-predicted by 16% in comparison to 40% ($d_g = 3$ mm,

$\alpha_g < 0.3$) or 29% ($d_g = 2.4$ mm, $\alpha_g < 0.3$). These results showed that more accurate $K_L a'$ values could indeed be obtained by a more rigorous specification of the interfacial area. It is proposed that this can be done through the incorporation of a population balance model.

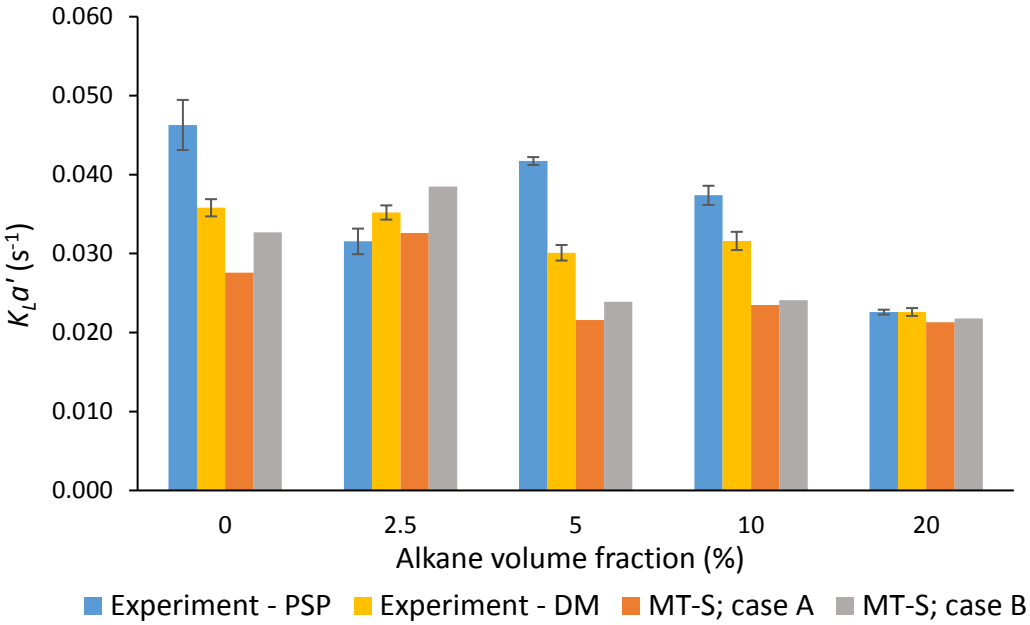

Figure 6.11: Comparison of the impact of modelling assumptions in values of $K_L a'$ at 800 rpm. Case A represents a bubble size of 3 mm whereas case B represents a bubble size of 2.4 mm. Adapted from Gakingo et al. [191].

6.4 Summary

The investigations into the 3-phase (cell-free) alkane-based system done in this chapter have revealed several significant findings that can aid in the design of bioreactors for such or similar systems. Foremost, a validated approach to the CFD-based modelling of cell-free alkane-based stirred reactors has been presented. It has been shown that the alkane phase should be modelled as an independent phase and its interaction with the turbulence of the system considered. This was done on the basis of the Euler-Euler-Euler (EEE) approach leading to predicted gas hold up values that were generally within 30% of the experimental values. Furthermore, it has been shown that use of either a velocity-inlet boundary condition (BC1) or a pressure-outlet boundary condition (BC2) to represent the exit of the gas phase from the top surface of the reactor will result in a similar trend of the predicted gas hold up values. A maximum difference of 16% was observed between the results of simulations employing these two boundary conditions and this was attributed to the ingestion of air from the headspace included at the top of the reactor during the set up of BC2.

Secondly, clarity has been provided on the mechanisms by which the alkane phase affects the hydrodynamics of a stirred tank reactor. It has been shown that for a stirred tank reactor operating in the turbulent regime, the alkane phase will not affect the hydrodynamics through a change in the effective fluid properties (viscosity). This is because the hydrodynamics of such a reactor are dominated by turbulence as evidenced by a larger value of turbulence viscosity in comparison to the fluid's effective viscosity (μ_t/μ_{eff} of the order $O(10-100)$). Modelling based on the pseudo-homogenous treatment of the liquid-liquid mixture (PH-EE approach) resulted in constant gas hold up values that were not in agreement with the experimental trend of a decrease in gas hold up with increase in alkane concentration (see Figure 6.1 and Figure 6.2).

In connection with the above, it has been shown that changes in the hydrodynamics due to the alkane phase should rather be attributed to the influence of the latter on the turbulence of the system. In particular, the turbulent motion of the alkane droplets contributed to higher values of the turbulent kinetic energy and its dissipation rate thus leading to an increase in the turbulence viscosity. The latter, in turn, acted to reduce the mean velocities of the continuous phase thereby resulting in reduced drag experienced by the gas phase. The end result of this was a reduction in gas hold up which was in agreement with the experimental trend. The CFD model based on the EEE approach was observed to predict gas hold up values that were generally within 30% of the experimental values.

Secondary effects of the alkane phase have also been shown with regards to its impact on other features of the flow such as the pumping capacity, the power drawn as well as temporal flow variations. As pertains the pumping capacity, a reduction in the same was observed and this was attributed to flooding of the impellers by the gas phase due to its reduced dispersion within the reactor. The power drawn by impellers, on the other hand, increased with increase in alkane concentration and this was attributed to the increased dissipation rate by the alkane phase. Finally, temporal flow variations (macro-instabilities) were dampened due to the increase in turbulence viscosity as explained above.

As pertains to oxygen transfer, it has been shown that a CFD-based approach can predict $K_L a'$ values with reasonable accuracy. This was illustrated by good predictions obtained at 600 rpm where $K_L a'$ values were within 11% of experimental values for alkane concentrations $\alpha_o \leq 10\%$. However, improvements to this modelling approach are needed

through, for example, the inclusion of a population balance model for the bubble size distribution.

Besides the above, possible mechanisms through which the alkane phase can impact oxygen transfer have been highlighted. In particular, the $K_L a'$ values were shown to be quite sensitive to changes in the gas hold up and the turbulence levels. On the other hand, minimal sensitivity was observed in the specification of different possible mass transfer pathways (8% maximum difference). As only the cases of series mass transfer with or without shuttling have been considered, it would be interesting to investigate whether similar observations can be obtained if the assumptions underpinning the mass transfer model were changed. For example, parallel mass transfer can be considered. This is recommended as future work.

7.0 Gas-liquid-liquid-solid system

This chapter presents a discussion on both the hydrodynamics and oxygen transfer in the 4-phase alkane-based bioreactor. It addresses itself to objectives 7, 8 and 9 of the study. The latter included the extension of the CFD-based modelling approach to the 4-phase system as well as the prediction and validation of oxygen transfer in the system.

7.1 Hydrodynamics and gas hold up trends

Similar to Chapter 6.0, the ability of the extended CFD model to represent the 4-phase system was assessed by comparing the predicted gas hold up values to the experimental values. Figure 7.1 and Figure 7.2 present the results of this analysis. It is to be noted that the CFD simulations were run at fewer data points (9) as compared to the experimentally measured data points (15). This difference was a result of the CFD modelling approach adopted. In particular, the CFD modelling approach could be able to directly account for changes in the agitation rate and the alkane concentration. However, the use of average bubble diameters based on equation (4.24) to capture the non-coalescing effect of the yeast phase meant that changes due to different yeast loadings could not be resolved (refer to section 4.2.3). Equation (4.24) could predict an average bubble diameter at a given agitation rate but could not distinguish between different yeast loadings at the same agitation rate. Consequently, fewer CFD simulations had to be run.

As an illustrative example of the above, entries 2, 4 and 5 in Figure 7.1 represented three experimental data points with different yeast loadings but fixed values of the alkane concentration and the agitation rate. For these points, however, only a single CFD simulation was run based on an average bubble diameter (equation (4.24)). Consequently, repeated entries of the CFD output had to be employed to populate the parity plot. All such entries in Figure 7.1 have appeared in a horizontal plane parallel to the x-axis.

Figure 7.2, on the other hand, provides a different perspective on the data. In this figure, changes in the gas hold up data due to changes in either the alkane concentration or the yeast loading were averaged out. Instead, error bars were employed to capture the spread in gas hold up data due to these factors. Thus, the figure provides a direct comparison of the experimental and predicted values with reference to changes in the agitation rate.

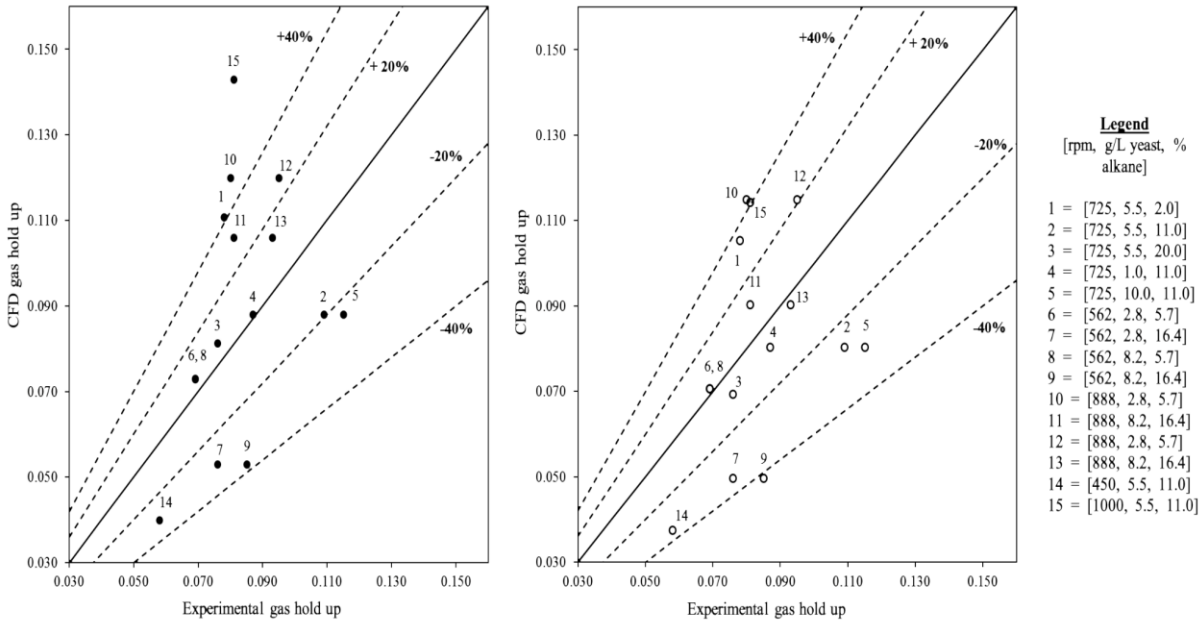

Figure 7.1: Comparison of experimental versus predicted gas hold up values. Left – predicted gas hold up values based on initial equations of the drag force. Right – predicted gas hold up values based on modified equations of the drag force (equation (7.1)). Reproduced from Gakingo et al. [193].

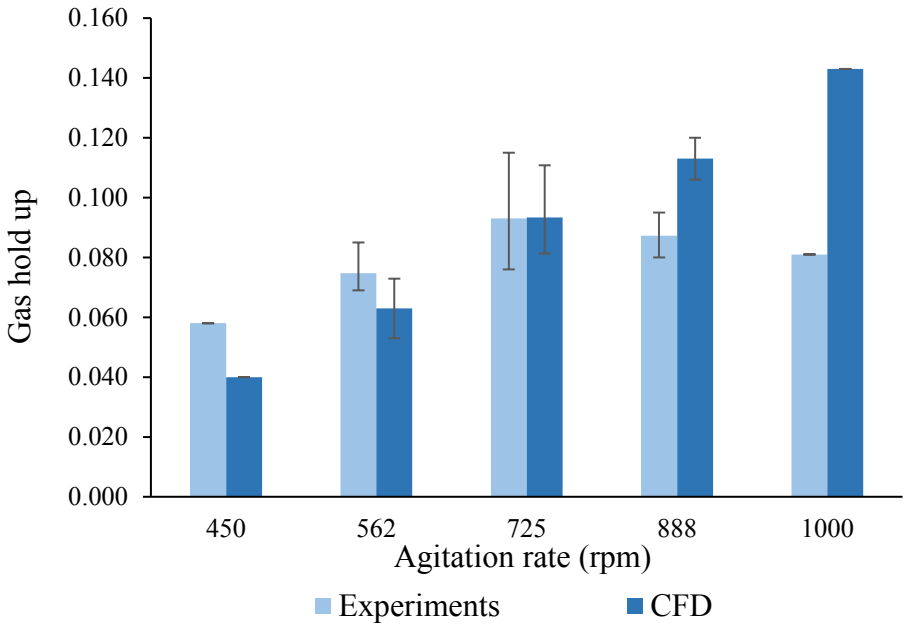

Figure 7.2: Experimental versus predicted gas hold up values, with the latter based on the initial equations of the drag force. The gas hold up values have been averaged over the alkane concentration and yeast loading. Adapted from Gakingo et al. [193].

It can be observed from Figure 7.1 (left image) and Figure 7.2 that the CFD model based on the initial equations of the drag force (refer to section 4.2.3) predicted reasonable gas hold up values. This could be quantified to within 20% and 40% accuracy bands, with the majority of predicted values being within 40% accuracy as illustrated in Figure 7.1 (left image). This compared well with the results generated for the 3-phase gas-liquid-liquid system where a general accuracy of 30% was reported (see Figure 6.1 and Figure 6.2). It is to be noted, however, that a number of points lay outside the 40% accuracy range. Such points included point 15 (1000 rpm, 11% alkane volume fraction) where the CFD model over-predicted the gas hold up by 77%. This represented the maximum over-prediction by the CFD model occurring at the highest agitation rate as illustrated in Figure 7.2.

The CFD model was also noted to predict a continuous increase in gas hold up with increase in agitation rate (see Figure 7.2). Contrary to this, the experimental values peaked at around 725 rpm and slightly declined thereafter. This suggested that there was an extra mechanism, not accounted for in the CFD model, that counteracted the predicted continuous increase in gas hold up. Furthermore, this mechanism became significant at higher agitation rates.

To explain the above observation, it was hypothesised that clusters of individual air bubbles bridged by the yeast cells were forming. Moreover, these clusters escaped the reactor faster than individual bubbles thus reducing the gas hold up. This was in line with previous observations in mineral flotation studies where clusters of air bubbles bridged by mineral particles have been reported [218–220]. Additionally, clusters of air bubbles and oil droplets bridged by yeast cells have been observed in a previous study on hydrocarbon fermentation [162]. However, in the particular study [162], live yeast with an affinity for the oil phase was employed in contrast to the non-viable (dead) yeast cells used in the case study under consideration [16,164].

It is to be noted that the seemingly greater effect of cluster formation at higher agitation rates could be linked to observations of improved floatability of small particles at high agitation rates [221–223]. This has been observed in mineral flotation studies [221,222] and was reasonably expected to apply in this case since the yeast cells had a size distribution in the range of 1 – 20 μm [16,164]. The mechanism behind this was that of increased particle-bubble collision rates as, among other reasons, the local or spatially distributed gas hold up increased with increase in agitation rate (see Figure 7.3).

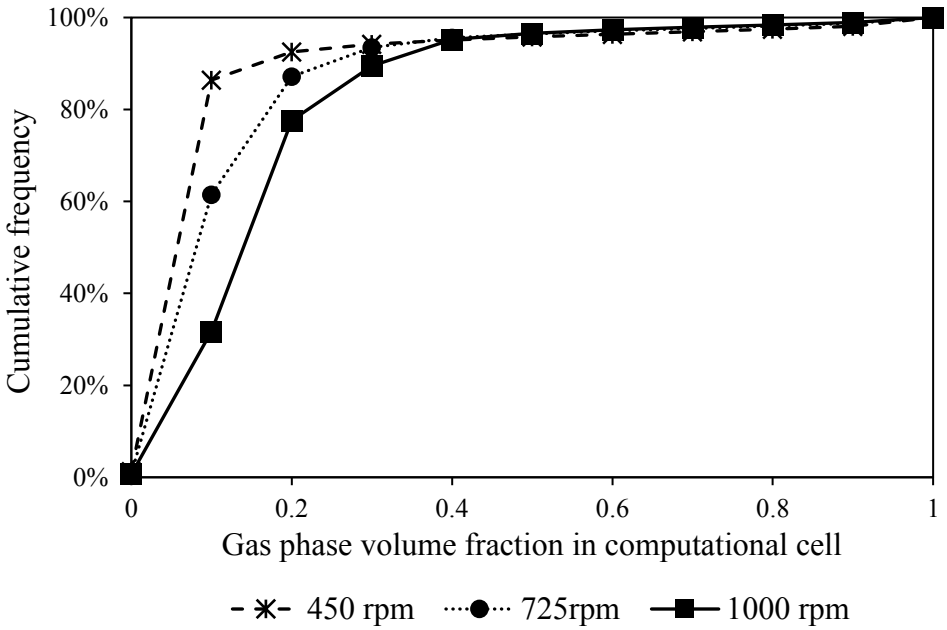

Figure 7.3: Cumulative frequency of computational cells containing a given gas phase volume fraction. Simulations done at 11% alkane volume fraction and varying agitation rates. Reproduced from Gakingo et al. [193].

To test the hypothesis on cluster formation, it was assumed that the bubble clusters would bring about reduced gas hold up through a reduction in the effective drag. This implied a need to correct the drag terms specified in equations (4.25) and (4.26) (repeated below). Given that the likelihood of cluster formation increased with increase in the local gas hold up (higher particle-bubble collision rates), a correction term based on the local gas hold up (α_g) was introduced as illustrated in equation (7.1). In this equation, the hindrance effect arising from bubble-bubble interaction was limited to $\alpha_g < 0.1$. This was in line with the observation that the changes in the local gas hold up were largely confined to the range $0 < \alpha_g < 0.4$ (see Figure 7.3). Consequently, the clustering phenomenon was expected to occur within this range. For $\alpha_g \geq 0.1$, on the other hand, it was assumed that the drag force would decrease with increase in local gas hold up in a manner similar to that observed in bubble swarms [110]. Finally, a constant $\Theta = 2.4$ was introduced into the equation to enforce continuity at $\alpha_g = 0.1$. Results from the simulations employing equation (7.1) are presented in Figure 7.1 (right image).

$$\frac{C_D}{C_{D,\infty}} = f\left(\frac{\tau_p}{\tau_L}\right) \cdot g(\alpha_g) \qquad (4.25)$$

$$g(\alpha_g) = \exp(3.64\alpha_g) + \alpha_g^{0.864} \tag{4.26}$$

$$g(\alpha_g) = \begin{cases} \exp(3.64\alpha_g) + \alpha_g^{0.864} & \alpha_g < 0.1 \\ \Theta \cdot (1 - \alpha_g)^4 & otherwise \end{cases} \tag{7.1}$$

A comparison the gas hold up values predicted prior to and after the consideration of cluster formation illustrated that improved predictions were obtained based on the latter (see Figure 7.1). In particular, the degree of over-prediction at agitation rates higher than 725 rpm was reduced. As an example of this, the over-prediction error at point 15 (1000 rpm) was now 41%, down from 77% initially. It was also observed that the predicted gas hold up values for agitation rates lower than 725 rpm decreased albeit slightly. As an example of this, an under-prediction error of 42% was now observed at point 9 (562 rpm, 16.4% alkane volume fraction) in comparison to 38% initially.

7.2 Impact of the additional phases on hydrodynamics

Building on the above results, the possible individual and interacting influences of both the alkane and the yeast phases on the hydrodynamics of the reactor could be examined. With regards to the alkane phase, similar influences to those reported in the 3-phase case were observed. In particular, the CFD model predicted a decrease in gas hold up with an increase in alkane concentration (see Figure 7.4). The mechanism behind this was that of a higher turbulence viscosity that led to dampened mean velocities and hence reduced drag (see Chapter 6.0).

The yeast phase, on the other hand, mainly served to make the medium non-coalescing thus resulting in small air bubbles. Though the yeast phase could also promote the formation of clusters as previously hypothesised, the influence of small bubbles was expected to remain dominant. Moreover, such small bubbles could effectively follow the mean flow of the aqueous phase despite a reduction in its magnitude due to an increase in the alkane concentration. Thus, the gas phase remained effectively dispersed within the reactor. This is illustrated in Figure 7.5 which contrasts the spatially distributed gas hold up values for two 3-phase cases (bubble diameter of 3 mm) and one 4-phase case (bubble diameter of 0.7 mm). It can be observed that there was greater gas dispersion (hence gas hold up) in the 4-phase case

despite a comparison of slightly different operating conditions which was a reflection of the different experimental designs previously used (see section 4.4.3).

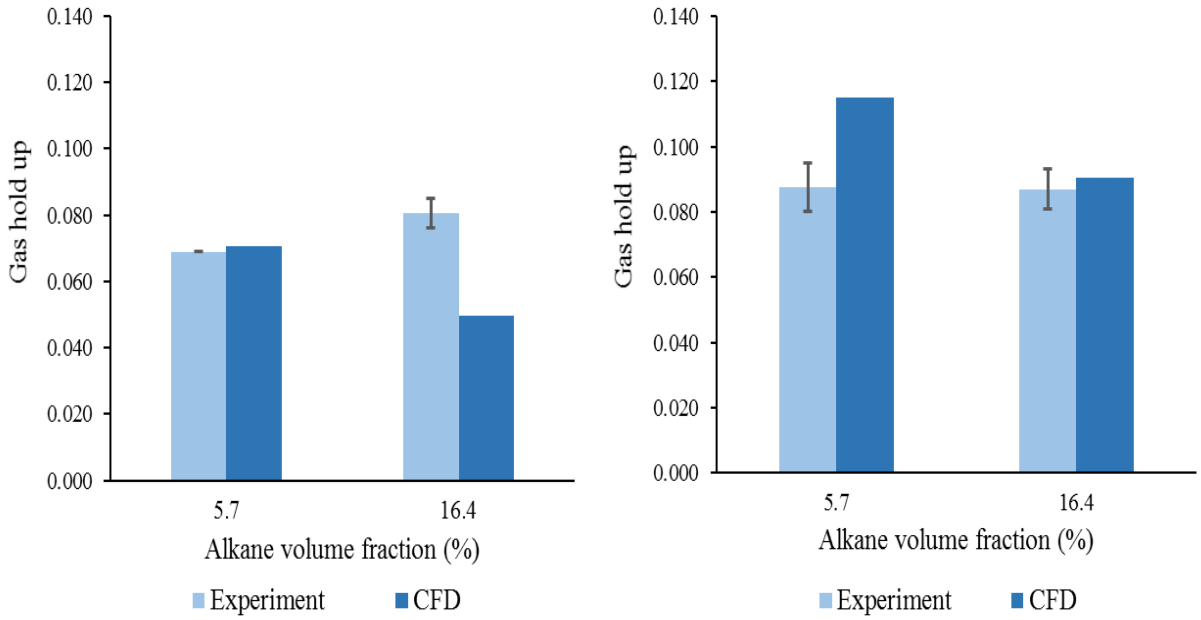

Figure 7.4: Predicted versus experimental gas hold up values at 562 rpm (left) and 888 rpm (right). Experimental values have been averaged over the yeast loading, with the error bars representing the maximum and minimum values. Adapted from Gakingo et al. [193].

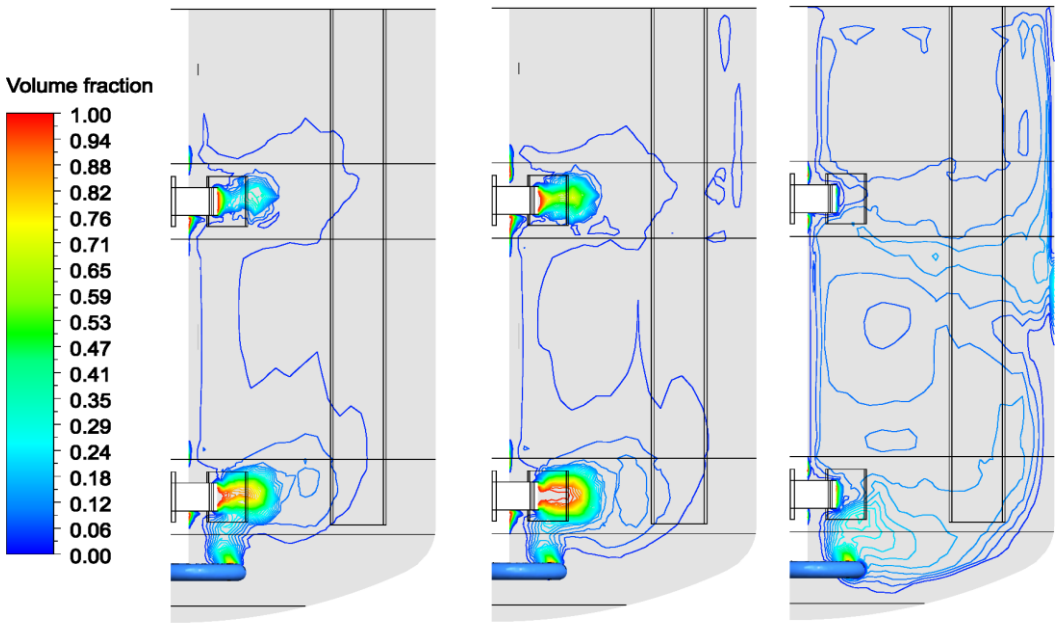

Figure 7.5: Contours of gas hold up on a mid-baffle plane. Left: 3-phase case with 600 rpm and 10% alkane volume fraction. Centre: 3-phase case with 800 rpm and 10% alkane volume fraction. Right: 4-phase case with 725 rpm and 11% alkane concentration. Reproduced from Gakingo et al. [193].

It is to be noted that the experimental trends in Figure 7.4 did not agree with the CFD-predicted trend of a decrease in gas hold up with increase in alkane concentration. Rather, an increase in gas hold up was observed at 562 rpm whereas an insignificant change in the gas hold up was observed at 888 rpm. In light of the CFD results in the same figure, these experimental observations suggested an increase in the residence time of the gas phase with increase in the alkane concentration. This led to the hypothesis that there could have been a hindrance of the motion of air bubbles by the alkane droplets themselves. This was besides the dampening effect of the alkane droplets on the mean velocities of flow as already discussed. The hindrance of motion by the alkane droplets could have been more significant in the 4-phase reactor as compared to the 3-phase reactor since the air bubbles now had a size that was comparable to that of the alkane droplets. This would especially be the case if clusters of the alkane droplets also formed as has been previously observed in a different study [162].

Baltussen et al. [224,225] have recently published findings that support the above hypothesis. Their work entailed the direct numerical simulations of a representative gas-liquid-solid system with particles of a comparable size (air bubble diameter – 2 mm, solid particle diameter – 1 mm) [224,225]. The authors illustrated that the effective drag on gas bubbles was comprised of two components; one arising from bubble-bubble interactions and the other arising from bubble-particle interactions [224,225]. As pertains the latter, they observed that the effective drag increased with increase in volume fraction of the solid phase [224,225]. Thus, it would be reasonable to expect similar occurrences between the alkane droplets and the air bubbles in the system under consideration if these particles were of a comparable size.

7.3 Oxygen transfer

Oxygen transport within the reactor was modelled on the basis of equations (4.27) and (4.28) (refer to section 4.3). In addition, several of the findings from Chapter 6.0 were incorporated into the modelling. For example, only mass transfer by the series model (MT-S) was considered since both this model and the series model with shuttling (MT-SS) were observed to predict similar $K_L a'$ values in the 3-phase reactor. Moreover, the definition of the interfacial area in equation (4.29) (repeated on next page) was set to include regions in the reactor with a gas phase volume fraction of $\alpha_g \leq 0.8$. This was in line with the findings of better $K_L a'$ predictions based on this value in the 3-phase reactor (800 rpm case).

$$K_L a' \approx E' \cdot K_L a_{\alpha_o=0} = E' \cdot \Lambda \cdot D^{0.5} \cdot \left(\frac{\epsilon}{\upsilon}\right)^{0.25} \cdot \left(\frac{6\alpha_g}{d_g}\right); \qquad \alpha_g \leq 0.8 \tag{4.29}$$

The use of equation (4.29) was based on previous studies in gas-liquid-solid systems [90,91], with the difference in this work being the incorporation of the alkane phase and its effects through the enhancement factor (E'). To account for the solid phase, Kawase & Moo-Young [90,91] considered a possible increase in effective viscosity ($\upsilon = \upsilon_{eff}$) whereas Wenmakers et al. [92] considered a possible decrease in the effective diffusivity ($D = D_{eff}$). Minimal change, however, was expected in both these properties given the yeast concentrations employed in this study [83]. This notwithstanding, particle-bubble interaction (collision, attachment and detachment) could occur thus impacting the mass transfer process.

Figure 7.6 presents a comparison of the experimental [164] and predicted $K_L a'$ values with respect to the agitation rates. These values have been averaged over the alkane concentration and the yeast loading. Furthermore, error bars have been employed to capture the spread in $K_L a'$ data due to changes in these factors.

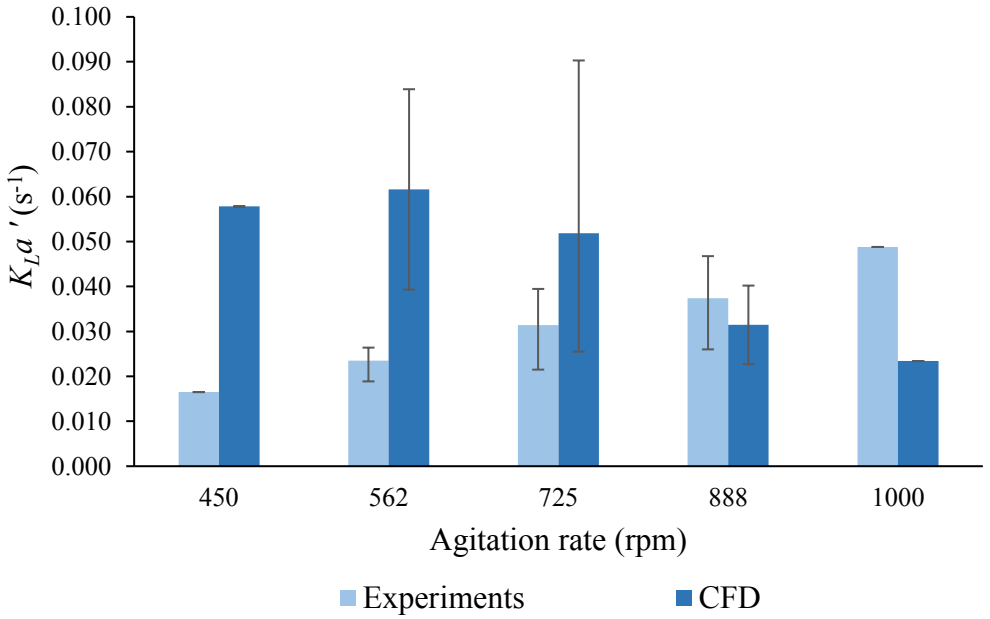

Figure 7.6: Experimental versus CFD-based $K_L a'$ values. These values have been averaged over the alkane concentration and the yeast loading, with the error bars representing the maximum and minimum values. Adapted from Gakingo et al. [193].

It can be observed from Figure 7.6 that the CFD-based $K_L a'$ values were higher than the experimental values at agitations rates of 725 rpm and below. Differences as high as 250% were noted at 450 rpm. The CFD-based $K_L a'$ values also showed a greater variation about the mean (average) thus suggesting a greater impact of the alkane concentration on $K_L a'$ than was experimentally observed. This is better resolved in Figure 7.7 and Figure 7.8 which capture the changes in $K_L a'$ due to changes in the alkane concentration at different agitation rates.

Figure 7.7 and Figure 7.8 confirm the observation that the CFD-based $K_L a'$ values were over-predicted at agitations rates of 725 rpm and below. Furthermore, the figures show that over-prediction largely occurred at low concentrations of the alkane phase. For example, over-predictions of 232% and 170% were observed at 562 rpm (5.7% alkane volume fraction) and 725 rpm (2% alkane volume fraction) respectively. This was despite the gas hold up values at these points being predicted to within 2% and 35% of the experimental values respectively. At other data points in the figures, however, more reasonable predictions of $K_L a'$ were observed. For example, at 888 rpm the predicted $K_L a'$ value at 5.7% alkane volume fraction was within 11% of the experimental value. Similarly, at 725 rpm, the predicted $K_L a'$ values at 11% and 20% alkane volume fractions were within 20% of the experimental values.

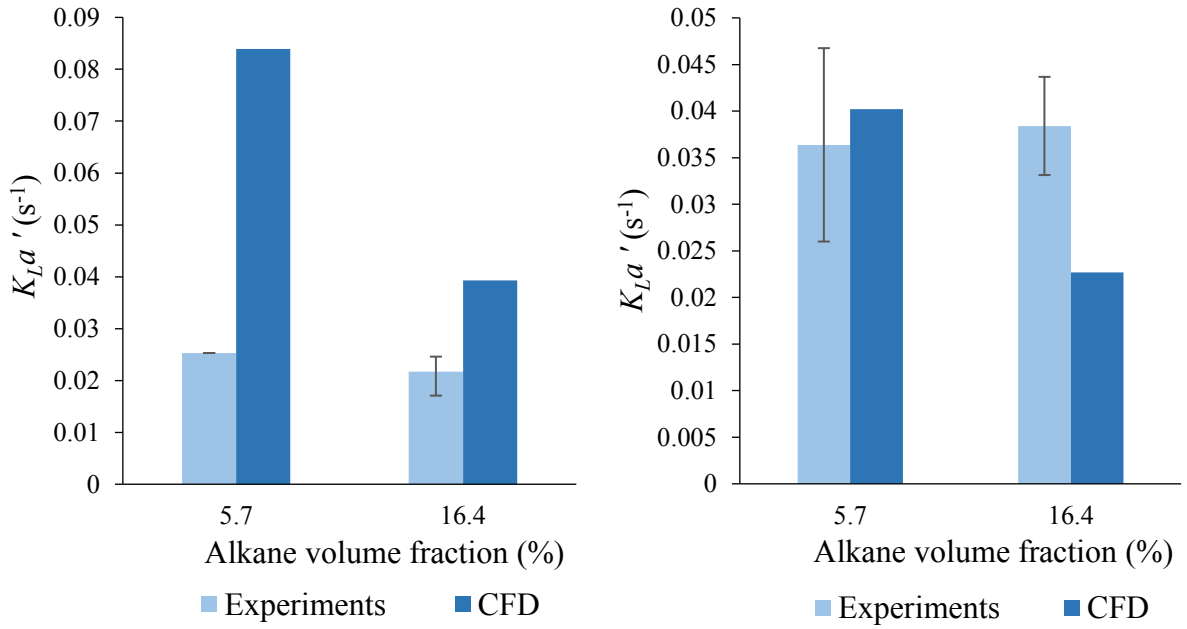

Figure 7.7: Experimental versus CFD-based $K_L a'$ values at 562 rpm (left) and 888 rpm (right). Experimental values have been averaged over the yeast loading, with the error bars representing the maximum and minimum values. Adapted from Gakingo et al. [193].

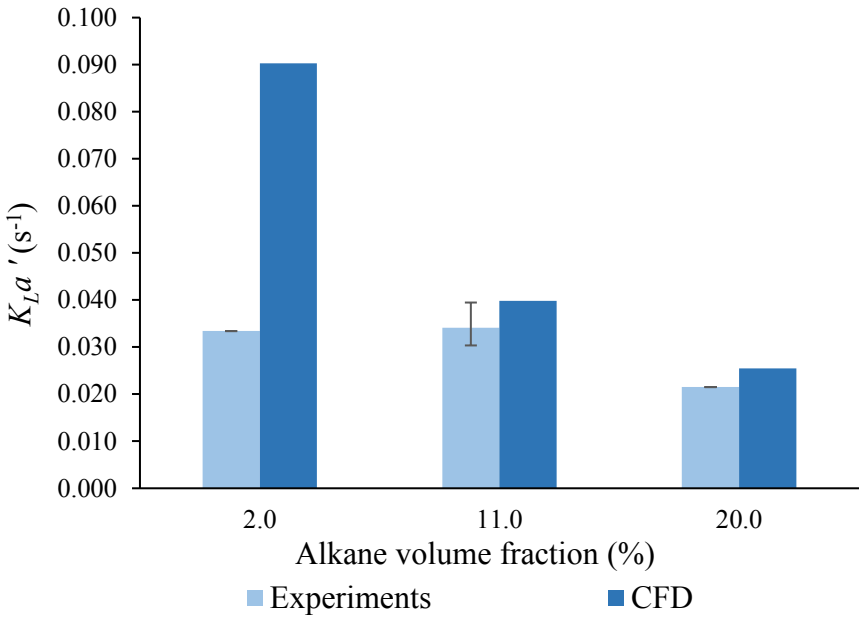

Figure 7.8: Experimental versus CFD-based K_La' values at 725 rpm. Experimental values have been averaged over the yeast loading, with the error bars representing the maximum and minimum values. Adapted from Gakingo et al. [193].

In seeking to explain the above observations, consideration was given to two factors. First was the possible under-estimation of experimental K_La' values due to their measurement using the dynamic gassing-out method (DM) in a medium that was non-coalescing [25]. As has been previously pointed out, this method is frequently used in mass transfer literature. However, it tends to under-predict K_La' values in non-coalescing media [25,42,174]. The pressure step method (PSP), on the other hand, is more accurate but it has been seldom used in studies on alkane-based systems [25,133]. Furthermore, the studies employing the PSP in alkane-based systems have considered cell-free systems [25,133] as opposed to those with cells/organisms. Thus, in an attempt to estimate the magnitude of under-prediction in the measured K_La' values, reference had to be made to a previous study comparing the DM to the PSP in a 3-phase (cell-free) alkane-based bioreactor [25]. In the particular study, under-estimation errors of up to 18% (600 – 800 rpm) and 33% (1000 rpm) were noted for the DM [25]. Assuming that similar magnitudes would apply to the 4-phase experimental K_La' values could not, however, solely explain the margins of over-prediction noted in Figure 7.6 – Figure 7.8.

The second consideration was that of particle-bubble interaction as manifested in the collision, attachment and detachment of air bubbles and yeast cells. The attachment of the non-viable yeast cells to the bubbles' surfaces could have resulted in a reduction of the

effective interfacial area (hence $K_L a'$ values) through physical blocking [65]. Moreover, a further reduction in the interfacial area could have occurred once cluster formation became significant (at high agitation rates). The mechanism behind the latter would have been the presence of air bubble clusters in the reactor with larger characteristic diameters than the individual bubbles.

In an attempt to estimate the potential reduction in interfacial area due to the above factors, reference was made to observations in mineral flotation studies. In such studies, maximum bubble surface coverage ratios of 10% to 50% have been suggested in the absence of the clustering phenomenon [80,81,226,227]. This implied that the interfacial area computed based on the CFD model could have been over-predicted by a similar magnitude or greater if the clustering phenomenon was considered.

If, for illustrative purposes, a 50% over-prediction in the interfacial area was assumed, then the predicted $K_L a'$ value at 450 rpm as an example would be 0.029 s^{-1} in comparison to an experimental value of 0.017 s^{-1}. This would represent an over-prediction of 75%, down from the initial 250% over-prediction captured in Figure 7.6. If, in addition, the experimental value was assumed to be under-predicted by 35% as an example, the predicted $K_L a'$ value (0.029 s^{-1}) would now be compared against a corrected experimental value of 0.022 s^{-1}. This would represent an over-prediction in $K_L a'$ of 30% by the CFD model which was comparable to the accuracy obtained for the predicted gas hold up values (~ 40%). Thus, accounting for these two factors provided sufficient grounds to explain the over-predictions noted in Figure 7.6 – Figure 7.8.

7.4 Summary

Despite the poor prediction of $K_L a'$ values, the investigations into the 4-phase alkane-based system done in this chapter have revealed several insights applicable to bioreactor design. Foremost, it has been shown that a model based on an Eulerian description of the air, aqueous and alkane phases but indirectly accounting for the presence of the yeast cells can give a reasonable first approximation to the hydrodynamics. The developed model was able to predict gas hold up values with an accuracy of about 40%. It has been suggested, however, that further improvement in the 4-phase model can be obtained by considering the interaction between the air bubbles and the alkane droplets and the influence of this on the total drag experienced.

Secondly, the investigations have highlighted possible mechanisms by which the additional phases can impact the hydrodynamics of the system. For example, addition of the alkane phase was predicted to lead to a decrease in magnitude of the mean flow similar to the observations in the 3-phase system. On the other hand, the yeast phase with its non-coalescing effect led to the formation of small bubbles that were effectively able to follow the mean flow despite a reduction in its magnitude. Consequently, higher gas hold up values were obtained in the 4-phase system in comparison to 3-phase system due to greater gas dispersion within the reactor (see Figure 7.5). These findings, though seemingly reasonable, call for more definitive studies in terms of experimental measurements.

Finally, the possible influence of particle-bubble interaction on oxygen transfer in the system has been highlighted. In particular, it has been shown that the latter can lead to a possible decrease in the interfacial area. The mechanisms behind this would be either physical blocking arising from the attachment of yeast cells to air bubbles or the presence of clusters in the reactor with characteristically larger diameters than individual bubbles. These effects have been hypothesised to be partly responsible for the over-predictions noted in the CFD-based $K_L a'$ values. However, further studies in terms of experimental measurements are required to validate these hypotheses.

8.0 Conclusions and recommendations

A threefold aim was set at the beginning of this study, the achievement of which was geared towards a deeper understanding of oxygen transfer in alkane-based bioprocesses as well the development of a validated CFD-based methodology that can enhance bioreactor design in such processes. The aim was underpinned by several research questions that emerged from a review of literature. These questions included:

1. What are the appropriate fundamental models that can be employed to predict oxygen transfer in alkane-based bioprocesses based on CFD output?
2. What are the main differences in the hydrodynamics and oxygen transfer of an alkane-based bioprocess in comparison to a 2-phase gas-liquid system? Can these be captured based on CFD modelling?
3. How does CFD-based prediction of oxygen transfer in a 3-phase cell-free alkane-based bioprocess compare with experimental data?
4. How does CFD-based prediction of oxygen transfer in a 4-phase alkane-based bioprocess with non-viable yeast cells compare with experimental data?

The above research questions were investigated and answered in the previous chapters. Herein, a summary of the key findings and their implications is presented. In addition, recommendations for future work have been given.

8.1 Model development and validation

Prior to the investigations carried out on the alkane-based systems, it was necessary to identify fundamental models of the overall volumetric mass transfer coefficient ($K_L a'$) that were applicable to alkane-based bioprocesses and that could be coupled to CFD-based output. Additionally, it was necessary to develop and validate CFD models capable of describing the hydrodynamics and oxygen transfer in a stirred reactor operating with both a single phase (water) and two phases (air, water). These models served as the baseline from which studies on the alkane-based systems were to be conducted. The key findings that arose from this work are enumerated on the next page.

1. It has been shown that models of $K_L a'$ applicable to alkane-based systems can be derived by considering two counteracting effects that the alkane phase introduces.

These include possible enhancement due to new mass transfer pathways and an apparent decrease in $K_L a'$ due to longer saturation times (higher absorption capacity of liquid-liquid mixture). Modelling of $K_L a'$ based on these considerations permitted for the consistent extension of fundamental 2-phase mass transfer theories to the alkane-based systems and paved way for the use of methodologies such as CFD. This represents a novel extension to mass transfer studies in alkane-based or analogous systems that would allow for the assessment of bioreactor concepts *in silico*.

2. A validated CFD-based methodology for single phase stirred tank reactors has been provided that can be used in future studies. It has been shown that the main features of flow can be adequately simulated by employing a RANS-based approach for turbulence and the MRF technique for impeller-baffle interaction. Time-averaged diverging flow patterns were observed and these were shown to be in agreement with previous findings in literature based on a comparison of several flow parameters. For example, a time-averaged power number of 11.2 was obtained in comparison to an experimentally measured value of 9.5. Additionally, a time-averaged pumping number of 0.91 was obtained for the upper impeller in comparison to experimentally reported values of 0.75 $\pm$0.15.
3. A validated CFD-based methodology for 2-phase gas-liquid stirred tank reactors has been provided that can be used in future studies. It has been shown that the main flow features can be adequately simulated by employing a RANS-based approach (turbulence), the MRF technique (impeller-baffle interaction) as well as a constant bubble size assumption. For this case, however, it was shown that the effect of turbulence on drag needs to be considered for a correct prediction of the gas hold up values. It was observed that the CFD model predicted the formation of gas cavities or regions of high gas volume fraction behind the impeller blades in line with findings in literature. This led to a decrease of about 49% in the power drawn which compared well with empirically predicted reductions of 33% – 35%. In addition, the overall (volume-averaged) gas hold up values were predicted to within 22% of the experimental values.
4. It has been shown for the first time that transient periodic variation in the mean flow patterns (macro-instabilities, MI) can be captured based on the use of the MRF technique with time-stepping. The observed MIs were noted to have a non-dimensional frequency of 0.011 which was in line with previously reported values (0.015 – 0.186). This finding was significant since previous simulations capturing MIs have relied on the sliding mesh technique. Given that the MRF technique offers a lower computational

burden than the sliding mesh technique, futures studies on MIs can be based on the former.

5. It has been shown that MIs can potentially impact mass transfer in a 2-phase gas-liquid reactor. The overall gas hold up was observed to oscillate about a mean value and this was driven by temporal fluctuations in the local (spatially distributed) gas hold up values. The latter can translate to fluctuating local concentrations of oxygen or substrate and this can potentially impact the productivity of micro-organisms present in a reactor experiencing MIs.

8.2 Gas-liquid-liquid system

The investigations into the 3-phase cell-free alkane-based system involved the identification/investigation of the mechanisms by which the alkane phase impacts the hydrodynamics of a stirred reactor. In addition, a CFD model of the alkane-based system was developed and coupled to identified models of $K_L a'$ so as to predict oxygen transfer. Finally, the predicted values were validated against experimental data. The key findings arising from the work done are enumerated below.

1. A validated CFD-based methodology for cell-free alkane-based stirred reactors has been presented and this can be used in future studies. It has been shown that it is necessary to model all the phases independently as well as to consider the interphase interactions amongst them. For the alkane phase, modelling of its interaction with the turbulence of the continuous phase has been shown to be necessary for the appropriate description of the hydrodynamics. The developed CFD model, based on the Euler-Euler-Euler (EEE) approach, was observed to predict gas hold up values that were generally accurate to within 30%. Furthermore, it was shown that the predicted gas hold up trend was not influenced by the choice of boundary condition employed to model escape of the gas phase from the top surface of the reactor. In particular, a maximum difference of 16% was observed between simulations based on the velocity-inlet boundary condition (BC1) and the pressure-outlet boundary condition (BC2).
2. It has been clearly shown that changes in the effective fluid properties (viscosity) by the alkane phase are not sufficient to alter the hydrodynamics of an alkane-based stirred reactor operating in the turbulent regime. Simulations based on the hypothesis that the liquid-liquid mixture could be treated as a pseudo-homogeneous liquid were observed to predict constant gas hold up values in contrast to the experimental trend. This was due

to the hydrodynamics of the system being governed by the turbulence levels as evidenced by larger values of the turbulence viscosity in comparison to the fluid's effective viscosity (μ_t/μ_{eff} of the order $O(10-100)$). The significance of this finding lay in the fact that this is a commonly hypothesised mechanism in literature.

3. In connection with point 2 above, the mechanism by which the alkane phase impacts the hydrodynamics and hence gas hold up has been clearly illustrated for the first time. It has been shown that the alkane phase primarily acts through the interaction of its droplets with the turbulence of the continuous phase. It was observed, based on simulations using the Euler-Euler-Euler approach, that the presence of the alkane phase resulted in higher values of the turbulent kinetic energy and its dissipation rate. This led to increased values of the turbulence viscosity which had a dampening effect on the mean velocities of the continuous aqueous phase. Consequently, the gas phase experienced reduced drag and dispersion within the reactor. This led to a quicker escape of the gas phase as evidenced by a reduction in the predicted overall gas hold up. The CFD-based gas hold up values generally agreed with the experimental trend to within 30%.
4. It has been shown that the alkane phase can have secondary effects on the hydrodynamics of a stirred reactor. These included a loss of pumping capacity due to the poorly dispersed gas phase flooding the impellers as well as a dampening of the macro-instabilities due to a higher turbulent viscosity. It was also observed that the 3-phase system had a higher power demand than a 2-phase system and this was attributed to the increased dissipation rate by the alkane phase. However, further investigations are recommended on the influence of the alkane phase on the power drawn since conflicting literature reports have been reported.
5. It has been shown that CFD-based prediction of oxygen transfer in a 3-phase alkane-based system can give results that are comparable with experimental measurements of the same. This was observed in the good accuracy (~11%) of predicted $K_L a'$ values obtained at 600 rpm and for alkane volume fractions, $\alpha_o \leq 10\%$. There is, however, room for improvement in the CFD-based modelling approach. This can be done achieved through the incorporation of population balance models so as to capture the dynamic changes in the bubble size distributions. The failure to model the latter was reasoned to be behind the over-prediction in gas hold up and $K_L a'$ at 600 rpm (20% alkane volume fraction) as well as the under-predictions in $K_L a'$ at 800 rpm.
6. It has been shown that oxygen transfer in alkane-based stirred reactors can be modelled, with reasonable accuracy, based on an assumption of series mass transfer. Minimal

sensitivity in the predicted $K_L a'$ values was observed for the different models of the gas-liquid interface tested (series mass transfer with or without shuttling). Rather, the predicted $K_L a'$ values were more sensitive to changes in the gas hold up and the turbulence levels. It would be interesting to investigate whether similar results would be observed if different assumptions were taken for the mass transfer model. These can include, for example, a lack of equilibrium in the dissolved oxygen concentration between the aqueous and alkane phases as well as parallel mass transfer. This is taken up as a recommendation for future work.

8.3 Gas-liquid-liquid-solid system

The investigations into the 4-phase alkane-based system involved the extension of the previously developed CFD model by incorporating hypothesised effects of the yeast phase. In addition, appropriate models of $K_L a'$ were employed in the prediction of oxygen transfer. Finally, the predicted values were validated against experimental data. The key findings arising from the work undertaken have been enumerated below.

1. A CFD-based methodology has been proposed for the 4-phase alkane-based system. It has been shown that a reasonable first approximation to the hydrodynamics can be obtained based on a model similar to that proposed for the 3-phase cell-free system. In this case, however, the effects of the yeast phase such as a change in the bubble diameters and a modification to the effective drag due to possible cluster formation would have to be included. It was observed that the developed CFD model had an accuracy of about 40% with regards to the gas hold up values. Proposals for the improvement of this model have also been given and these included a consideration of mutual hindrance of motion between air bubbles and alkane droplets given that they may be of a comparable size in the non-coalescing 4-phase system.
2. Possible influences of the additional phases on the hydrodynamics of the reactor have been highlighted though these require further experimental investigations. For example, addition of the alkane phase was predicted to lead to a reduction in the mean velocities of flow. However, the yeast phase with its non-coalescing effect led to the formation of small air bubbles that are able to follow the mean flow despite a reduction in its magnitude. This resulted in effective dispersion of the gas phase within the reactor of 4-phase system and consequently higher gas hold up values than those observed in the 3-phase system.

3. In connection with the above, it has also been suggested that the yeast phase can lead to secondary effects such as the formation of clusters of air bubbles arising from particle-bubble interactions. The formation of these clusters plus their subsequent escape was hypothesised to be behind the decrease in gas hold up values as the agitation rates increased beyond 725 rpm. At these agitation rates, an improvement in the floatability of the yeast cells by the air bubbles was expected. An attempt to incorporate this effect into the modelling was observed to lead to better predictions of the gas hold up values with an accuracy of about 40% achieved. All the same, further experimental investigations of this effect are recommended.
4. It has been shown that oxygen transfer in the 4-phase system is probably impacted by particle-bubble interaction. In particular, a decrease in the interfacial area is likely to occur due to physical blocking of the bubbles' surfaces by attached yeast cells or the formation of bubble clusters. These mechanisms were hypothesised to be behind the poor prediction of $K_L a'$ values by the CFD model. However, further experimental investigations are recommended to quantify their contributions.

8.4 Recommendations

Based on the findings of this research, the following recommendations for future work have been proposed:

1. The development of the CFD model for the considered systems relied on a number of significant assumptions/limitations to keep the model tractable. The resulting model was reasonably accurate as seen in the prediction of gas hold up and $K_L a'$ values. However, future investigations should look into relaxing some of the assumptions/limitations employed. These included:
    a. The treatment of turbulence in the system based on the Reynolds-averaged Navier-Stokes (RANS) equations and an eddy viscosity approach (dispersed k–ϵ model) to the exclusion of other approaches such as the Reynolds' stress model (RSM). The latter is known to better capture anisotropic effects of turbulence that exist in stirred tank reactors.
    b. The treatment of air bubbles as particles with a constant size. It has been suggested based on the 3-phase results that a modelling of the bubble size distributions with a population balance model can lead to an improvement in the oxygen transfer predictions.

c. The consideration of interphase interaction forces as primarily occurring between the continuous aqueous phase and the dispersed phases (air-aqueous or alkane-aqueous). It has been suggested based on the 4-phase results that consideration should also be given to the mutual hindrance of motion between the dispersed phases (alkane droplets and air bubbles).

d. The assumption that equilibrium in the dissolved oxygen concentration will always be maintained between the aqueous and the alkane phase as well as the prescription of the series mass transfer pathway (with or without shuttling). An investigation of different mass transfer models/scenarios would give more conclusive proof as to the exact mechanism of mass transfer in alkane-based systems.

2. The development of the CFD model also required validation at various stages such as the mesh independence study done in the single phase system. Though the validation was done based on the availability of data, future studies should look into adopting a more robust validation approach. This could entail, for example, an examination of velocity data as well as mesh independence studies using representative conditions in the 3-phase and 4-phase systems. In connection with this, oxygen transfer data used for validation should be rather obtained based on the pressure step method. This is particularly important for the non-coalescing 4-phase system.
3. The interaction of the alkane phase with the turbulence of the continuous phase has been observed to have a significant effect on the hydrodynamics of the stirred tank reactor. Though this was supported based on the trends in gas hold up, future investigations should look into making direct measurements of these effects. This should include the measurement of velocities and turbulence quantities in alkane-based systems through techniques such as particle image velocimetry that have been used for 2-phase liquid-liquid systems [139–141]. In addition, the trends in the power drawn as the alkane concentration changes should be measured.
4. The presence of the non-viable yeast cells was hypothesised to lead to physical blocking as well as to the formation of bubble clusters. Future investigations should look into experimentally quantifying these effects at different process conditions. In addition, the presence of these effects should be investigated for viable (live) yeast cells as well as for different organisms/cells. Literature studies indicate that the hydrophobicity of organisms/cells changes with the cell type and the growth phase thus suggesting a change in the degree of particle-bubble interaction.

5. Whereas this study focused on exploring the hydrodynamics and oxygen transfer in a stirred tank operating in the turbulent regime, future work should investigate whether the observations made hold true in equipment with different flow regimes such as bubble column reactors.

References

[1] M. Ayala, E. Torres, Enzymatic activation of alkanes: constraints and prospective, Appl. Catal. A Gen. 272 (2004) 1–13. doi:10.1016/J.APCATA.2004.05.046.

[2] S. Fukui, A. Tanaka, Production of useful compounds from alkane media in Japan, Adv. Biochem. Eng. 17 (1980) 1–35. doi:10.1007/3-540-09955-7_6.

[3] L. Soussan, N. Pen, M.-P. Belleville, J.S. Marcano, D. Paolucci-Jeanjean, Alkane biohydroxylation: Interests, constraints and future developments, J. Biotechnol. 222 (2016) 117–142. doi:10.1016/J.JBIOTEC.2016.02.007.

[4] World Energy Council, World Energy Resources 2013 Survey, London, 2013. www.worldenergy.org (accessed 14 August 2019).

[5] SASOL, Secunda Synfuels Operations. www.sasol.com/about-sasol/regional-operating-hubs/southern-africa-operations/secunda-synfuels-operations/overview (accessed 12 August 2019).

[6] DST-NRF Centre of Excellence in Catalysis - c*change, Paraffin Activation. www.cchange.ac.za/paraffin-activation/ (accessed 12 August 2019).

[7] B. Bühler, A. Schmid, Process implementation aspects for biocatalytic hydrocarbon oxyfunctionalization, J. Biotechnol. 113 (2004) 183–210. doi:10.1016/J.JBIOTEC.2004.03.027.

[8] M.T. Lundemo, J.M. Woodley, Guidelines for development and implementation of biocatalytic P450 processes, Appl. Microbiol. Biotechnol. 99 (2015) 2465–2483. doi:10.1007/s00253-015-6403-x.

[9] K.G. Clarke, L.D.C. Correia, Oxygen transfer in hydrocarbon-aqueous dispersions and its applicability to alkane bioprocesses: A review, Biochem. Eng. J. 39 (2008) 405–429. doi:10.1016/j.bej.2007.11.020.

[10] F. Thevenieau, A. Beopoulos, T. Desfougeres, J. Sabirova, K. Albertin, S. Zinjarde, J.-M. Nicaud, Uptake and Assimilation of Hydrophobic Substrates by the Oleaginous Yeast Yarrowia lipolytica, in: K.N. Timmis (Ed.), Handb. Hydrocarb. Lipid Microbiol., Springer, Berlin, Heidelberg, 2010: pp. 1513–1527. doi:10.1007/978-3-540-77587-4_104.

[11] P. Fickers, P.H. Benetti, Y. Waché, A. Marty, S. Mauersberger, M.S. Smit, J.M. Nicaud, Hydrophobic substrate utilisation by the yeast Yarrowia lipolytica, and its potential applications, FEMS Yeast Res. 5 (2005) 527–543. doi:10.1016/j.femsyr.2004.09.004.

[12] B.E. White, C.J. Fenner, M.S. Smit, S.T.L. Harrison, Effect of cell permeability and dehydrogenase expression on octane activation by CYP153A6-based whole cell Escherichia coli catalysts, Microb. Cell Fact. 16 (2017) 156. doi:10.1186/s12934-017-0763-0.

[13] P. Doran, Bioprocess Engineering Principles, Academic Press Ltd, London, 1995.

[14] L.D.C. Correia, C. Aldrich, K.G. Clarke, Interfacial gas-liquid transfer area in alkane-aqueous dispersions and its impact on the overall volumetric oxygen transfer coefficient, Biochem. Eng. J. 49 (2010) 133–137. doi:10.1016/j.bej.2009.12.007.

[15] K.G. Clarke, P.C. Williams, M.S. Smit, S.T.L.L. Harrison, Enhancement and repression of the volumetric oxygen transfer coefficient through hydrocarbon addition and its influence on oxygen transfer rate in stirred tank bioreactors, Biochem. Eng. J. 28 (2006) 237–242. doi:10.1016/j.bej.2005.11.007.

[16] P.G. Hollis, The overall oxygen transfer coefficient and interfacial area in aerated model hydrocarbon-based bioprocesses. Master's thesis, Stellenbosch University, South Africa, 2015.

[17] D.R. Nielsen, A.J. Daugulis, P.J. McLellan, A novel method of simulating oxygen mass transfer in two-phase partitioning bioreactors, Biotechnol. Bioeng. 83 (2003) 735–742. doi:10.1002/bit.10721.

[18] N. Gomes, M. Aguedo, J. Teixeira, I. Belo, Oxygen mass transfer in a biphasic medium: Influence on the biotransformation of methyl ricinoleate into γ-decalactone by the yeast Yarrowia lipolytica, Biochem. Eng. J. 35 (2007) 380–386. doi:10.1016/j.bej.2007.02.002.

[19] P.F.F. Amaral, M.G. Freire, M.H.M. Rocha-Leão, I.M. Marrucho, J.A.P. Coutinho, M.A.Z. Coelho, Optimization of oxygen mass transfer in a multiphase bioreactor with perfluorodecalin as a second liquid phase, Biotechnol. Bioeng. 99 (2008) 588–598. doi:10.1002/bit.21640.

[20] E. Dumont, H. Delmas, Mass transfer enhancement of gas absorption in oil-in-water systems: A review, Chem. Eng. Process. Process Intensif. 42 (2003) 419–438. doi:10.1016/S0255-2701(02)00067-3.

[21] J.B. Joshi, K. Nandakumar, Computational modelling of multiphase reactors, Annu. Rev. Chem. Biomol. Eng. 6 (2015) 347–378. doi:10.1146/annurev-chembioeng-061114-123229.

[22] J. Gimbun, C.D. Rielly, Z.K. Nagy, Modelling of mass transfer in gas-liquid stirred tanks agitated by Rushton turbine and CD-6 impeller: A scale-up study, Chem. Eng. Res. Des. 87 (2009) 437–451. doi:10.1016/j.cherd.2008.12.017.

[23] P. Ranganathan, S. Sivaraman, Investigations on hydrodynamics and mass transfer in gas-liquid stirred reactor using computational fluid dynamics, Chem. Eng. Sci. 66 (2011) 3108–3124. doi:10.1016/j.ces.2011.03.007.

[24] F. Kerdouss, A. Bannari, P. Proulx, R. Bannari, M. Skrga, Y. Labrecque, Two-phase mass transfer coefficient prediction in stirred vessel with a CFD model, Comput. Chem. Eng. 32 (2008) 1943–1955. doi:10.1016/j.compchemeng.2007.10.010.

[25] L.D.C. Correia, K.G. Clarke, Measurement of the overall volumetric oxygen transfer coefficient in alkane-aqueous dispersions, J. Chem. Technol. Biotechnol. 84 (2009) 1793–1797. doi:10.1002/jctb.2246.

[26] K. Rutherford, K.C. Lee, S.M.S. Mahmoudi, M. Yianneskis, Hydrodynamic characteristics of dual impeller stirred reactors, AIChE J. 42 (1996) 332–346. doi:10.1002/aic.690420204.

[27] V.V. Ranade, Computational flow modeling for chemical reactor engineering, Academic Press, New York, 2002.

[28] P.L. Viollet, O. Simonin, Modelling dispersed two-phase flows: closure, validation and software development, Appl. Mech. Rev. 47 (1994) 80–84. doi:10.1115/1.3124445.

[29] R.F. Mudde, O. Simonin, Two- and three-dimensional simulations of a bubble plume using a two-fluid model, Chem. Eng. Sci. 54 (1999) 5061–5069. doi:10.1016/S0009-2509(99)00234-1.

[30] R. Bel F'dhila, O. Simonin, Eulerian prediction of a turbulent bubbly flow downstream of a sudden pipe expansion, in: 6th Work. Two-Phase Flow Predict., Erlangen, Germany, 1992: pp. 264–273.

[31] O. Simonin, Eulerian formulation for particle dispersion in turbulent two-phase flows, in: 5th Work. Two-Phase Flow Predict., Erlangen, Germany, 1990: pp. 156–166.

[32] J.B. Joshi, N.K. Nere, C. V. Rane, B.N. Murthy, C.S. Mathpati, A.W. Patwardhan, V. V. Ranade, CFD simulation of stirred tanks: Comparison of turbulence models. Part I: Radial flow impellers, Can. J. Chem. Eng. 89 (2011) 23–82. doi:10.1002/cjce.20446.

[33] A.R. Khopkar, V. V. Ranade, CFD simulation of gas-liquid stirred vessel: VC, S33, and L33 flow regimes, AIChE J. 52 (2006) 1654–1672. doi:10.1002/aic.10762.

[34] A. Buffo, D.L. Marchisio, Modeling and simulation of turbulent polydisperse gas-liquid systems via the generalized population balance equation, Rev. Chem. Eng. 30 (2014) 73–126. doi:10.1515/revce-2013-0015.

[35] G.L. Lane, M.P. Schwarz, G.M. Evans, Modelling of the interaction between gas and liquid in stirred vessels, in: 10th Eur. Conf. Mix., Delft, The Netherlands, 2000: pp. 197–204. doi:10.1016/B978-044450476-0/50026-1.

[36] F. Scargiali, A. D'Orazio, F. Grisafi, A. Brucato, Modelling and simulation of gas–liquid hydrodynamics in mechanically stirred tanks, Chem. Eng. Res. Des. 85 (2007) 637–646. doi:10.1205/CHERD06243.

[37] F. Garcia-Ochoa, E. Gomez, Bioreactor scale-up and oxygen transfer rate in microbial processes: An overview, Biotechnol. Adv. 27 (2009) 153–176. doi:10.1016/j.biotechadv.2008.10.006.

[38] E.K. Nauha, O. Visuri, R. Vermasvuori, V. Alopaeus, A new simple approach for the scale-up of aerated stirred tanks, Chem. Eng. Res. Des. 95 (2015) 150–161. doi:10.1016/j.cherd.2014.10.015.

[39] D. Pinelli, Z. Liu, F. Magelli, Analysis of KLa Measurement Methods in Stirred Vessels : The Role of Experimental Techniques and Fluid Dynamic Models., Int. J. Chem. React. Eng. 8 (2010) 1–40. doi:10.2202/1542-6580.1915.

[40] C.S. Ho, L.-K. Ju, R.F. Baddour, Enhancing penicillin fermentations by increased oxygen solubility through the addition of n-hexadecane, Biotechnol. Bioeng. 36 (1990) 1110–1118. doi:10.1002/bit.260361106.

[41] B. Bandyopadhyay, A.E. Humphrey, H. Taguchi, Dynamic measurement of the volumetric oxygen transfer coefficient in fermentation systems, Biotechnol. Bioeng. 9 (1967) 533–544. doi:10.1002/bit.260090408.

[42] V. Linek, P. Benes, J. Sinkule, T. Moucha, Non-ideal pressure step method for kLa measurement, Chem. Eng. Sci. 48 (1993) 1593–1599. doi:10.1016/0009-2509(93)80119-B.

[43] K.G. Clarke, M.M. Manyuchi, Methodology for advanced measurement accuracy of the overall volumetric oxygen transfer coefficient with application to hydrocarbon-aqueous dispersions, J. Chem. Technol. Biotechnol. 87 (2012) 1615–1618. doi:10.1002/jctb.3853.

[44] C. Boyer, A.-M. Duquenne, G. Wild, Measuring techniques in gas-liquid and gas-liquid-solid reactors, Chem. Eng. Sci. 57 (2002) 3185–3215. doi:10.1016/S0009-2509(02)00193-8.

[45] M.I.I.Z. Abidin, A.A.A. Raman, M.I.M. Nor, Review on measurement techniques for drop size distribution in a stirred vessel, Ind. Eng. Chem. Res. 52 (2013) 16085–16094. doi:10.1021/ie401548z.

[46] S.S. Alves, C.I. Maia, J.M.T. Vasconcelos, A.J. Serralheiro, Bubble size in aerated stirred tanks, Chem. Eng. J. 89 (2002) 109–117. doi:10.1016/S1385-8947(02)00008-6.

[47] S.S. Alves, C.I. Maia, J.M.T. Vasconcelos, Experimental and modelling study of gas dispersion in a double turbine stirred tank, Chem. Eng. Sci. 57 (2002) 487–496. doi:10.1016/S0009-2509(01)00400-6.

[48] M. Bouaifi, M. Roustan, Bubble size and mass transfer coefficients in dual-impeller agitated reactors, Can. J. Chem. Eng. 76 (1998) 390–397. doi:10.1002/cjce.5450760307.

[49] K. Van't Riet, Review of measuring methods and results in nonviscous gas-liquid mass transfer in stirred vessels, Ind. Eng. Chem. Process Des. Dev. 18 (1979) 357–364. doi:10.1021/i260071a001.

[50] M.M. Lopes De Figueiredo, P.H. Calderbank, The scale-up of aerated mixing vessels for specified oxygen dissolution rates, Chem. Eng. Sci. 34 (1979) 1333–1338. doi:10.1016/0009-2509(79)80025-1.

[51] A. Schumpe, W.-D. Deckwer, Gas holdups, specific interfacial areas, and mass transfer coefficients of aerated Carboxymethyl Cellulose solutions in a bubble column, Ind. Eng. Chem. Process Des. Dev. 21 (1982) 706–711. doi:10.1021/i200019a028.

[52] Y. Kawase, M. Moo-Young, Mathematical models for design of bioreactors: Applications of Kolmogoroff's theory of isotropic turbulence, Chem. Eng. J. 43 (1990) B19–B41. doi:10.1016/0300-9467(90)80048-H.

[53] D.E. Leng, R. V. Calabrese, Immiscible liquid–liquid systems, in: E.L. Paul, V.A. Atiemo-Obeng, S.M. Kresta (Eds.), Handb. Ind. Mix. Sci. Pract., Wiley-Interscience, Hoboken, New Jersey, 2004: pp. 639–753.

[54] R. Clift, J.R. Grace, M.E. Weber, Bubbles, drops and particles, Academic Press, New York, 1978.

[55] J.M. Coulson, J.F. Richardson, J.R. Backhurst, J.H. Harker, Chemical Engineering, Pergamon Press, Oxford, United Kingdom, 1990.

[56] G.E. Fortescue, J.R.A. Pearson, On gas absorption into a turbulent liquid, Chem. Eng. Sci. 22 (1967) 1163–1176. doi:10.1016/0009-2509(67)80183-0.

[57] H.L. Toor, J.M. Marchello, Film-penetration model for mass and heat transfer, AIChE J. 4 (1958) 97–101. doi:10.1002/aic.690040118.

[58] Y. Kawase, B. Halard, M. Moo-Young, Liquid-phase mass transfer coefficients in bioreactors, Biotechnol. Bioeng. 39 (1992) 1133–1140. doi:10.1002/bit.260391109.

[59] J. Lamont, D. Scott, An eddy cell model of mass transfer into the surface of a turbulent liquid, AIChE J. 16 (1970) 513–519. doi:10.1002/aic.690160403.

[60] V. Linek, M. Kordaˇ, T. Moucha, Mechanism of mass transfer from bubbles in dispersions Part II : Mass transfer coefficients in stirred gas – liquid reactor and bubble column, 44 (2005) 121–130. doi:10.1016/j.cep.2004.05.009.

[61] S.S. Alves, C.I. Maia, J.M.T. Vasconcelos, Gas-liquid mass transfer coefficient in stirred tanks interpreted through bubble contamination kinetics, Chem. Eng. Process. Process Intensif. 43 (2004) 823–830. doi:10.1016/S0255-2701(03)00100-4.

[62] P.H. Calderbank, M.B. Moo-Young, The continuous phase heat and mass-transfer properties of dispersions, Chem. Eng. Sci. 16 (1961) 39–54. doi:10.1016/0009-2509(61)87005-X.

[63] V. Linek, M. Kordač, M. Fujasová, T. Moucha, Gas-liquid mass transfer coefficient in stirred tanks interpreted through models of idealized eddy structure of turbulence in the bubble vicinity, Chem. Eng. Process. Process Intensif. 43 (2004) 1511–1517. doi:10.1016/j.cep.2004.02.009.

[64] F. Garcia-Ochoa, E. Gomez, Theoretical prediction of gas-liquid mass transfer coefficient, specific area and hold-up in sparged stirred tanks, Chem. Eng. Sci. 59 (2004) 2489–2501. doi:10.1016/j.ces.2004.02.009.

[65] K.C. Ruthiya, J. van der Schaaf, B.F.M. Kuster, J.C. Schouten, Mechanisms of physical and reaction enhancement of mass transfer in a gas inducing stirred slurry reactor, Chem. Eng. J. 96 (2003) 55–69. doi:10.1016/j.cej.2003.08.005.

[66] J.H.J. Kluytmans, B.G.M. van Wachem, B.F.M. Kuster, J.C. Schouten, Mass transfer in sparged and stirred reactors: Influence of carbon particles and electrolyte, Chem. Eng. Sci. 58 (2003) 4719–4728. doi:10.1016/j.ces.2003.05.004.

[67] C. Roizard, S. Poncin, F. Lapicque, X. Py, N. Midoux, Behavior of fine particles in the vicinity of a gas bubble in a stagnant and a moving fluid, Chem. Eng. Sci. 54 (1999) 2317–2323. doi:10.1016/S0009-2509(98)00415-1.

[68] E. Alper, B. Wichtendahl, W.D. Deckwer, Gas absorption mechanism in catalytic slurry reactors, Chem. Eng. Sci. 35 (1980) 217–222. doi:10.1016/0009-2509(80)80090-X.

[69] R.L. Kars, R.J. Best, A.A.H. Drinkenburg, The sorption of propane in slurries of active carbon in water, Chem. Eng. J. 17 (1979) 201–210. doi:10.1016/0300-9467(79)85014-5.

[70] J. V. Littlejohns, A.J. Daugulis, Oxygen transfer in a gas-liquid system containing solids of varying oxygen affinity, Chem. Eng. J. 129 (2007) 67–74. doi:10.1016/j.cej.2006.11.002.

[71] A. Kaya, A. Schumpe, Surfactant adsorption rather than 'shuttle effect'?, Chem. Eng. Sci. 60 (2005) 6504–6510. doi:10.1016/j.ces.2005.03.002.

[72] A. Schumpe, A.K. Saxena, L.K. Fang, Gas/liquid mass transfer in a slurry bubble column, Chem. Eng. Sci. 42 (1987) 1787–1796. doi:10.1016/0009-2509(87)80183-5.

[73] E. Sada, H. Kumazawa, T. Iguchl, C. Lee, Gas Holdup and Mass-Transfer Characteristics in a Three-Phase Bubble Column, Ind. Eng. Chem. Process Des. Dev. 25 (1986) 472–476. doi:10.1021/i200033a020.

[74] T.S. Horozov, B.P. Binks, Particle-stabilized emulsions: A bilayer or a bridging monolayer?, Angew. Chemie - Int. Ed. 45 (2006) 773–776. doi:10.1002/anie.200503131.

[75] G. Bournival, S. Ata, E.J. Wanless, The roles of particles in multiphase processes: Particles on bubble surfaces, Adv. Colloid Interface Sci. 225 (2015) 114–133. doi:10.1016/j.cis.2015.08.008.

[76] F. Gentile, H. Oleschko, P. Veverka, V. Machon, A. Paglianti, W. Bujalski, A.W. Etchells III, A.W. Nienow, Some effects of particle wettability in agitated solid-gas-liquid systems: gas-liquid mass transfer and the dispersion of floating solids, Can. J. Chem. Eng. 81 (2003) 581–587.

[77] M. Van der Zon, P.J. Hammersma, E.K. Poels, A. Bliek, Coalescence of freely moving bubbles in water by the action of suspended hydrophobic particles, Chem. Eng. Sci. 57 (2002) 4845–4853. doi:10.1016/S0009-2509(02)00281-6.

[78] A. Schumpe, A.K. Saxena, K.D.P. Nigam, Gas/liquid mass transfer in a bubble column with suspended nonwettable solids, AIChE J. 33 (1987) 1916–1920. doi:10.1002/aic.690331122.

[79] L. Ju, A. Sundararajan, The effects of cells on oxygen transfer in bioreactors: physical presence of cells as solid particles, Chem. Eng. J. 56 (1994) B15–B21. doi:10.1016/0923-0467(94)87027-6.

[80] P.T.L. Koh, M.P. Schwarz, Modelling attachment rates of multi-sized bubbles with particles in a flotation cell, Miner. Eng. 21 (2008) 989–993. doi:10.1016/j.mineng.2008.02.021.

[81] P.T.L. Koh, M.P. Schwarz, CFD modelling of bubble – particle attachments in flotation cells, 19 (2006) 619–626. doi:10.1016/j.mineng.2005.09.013.

[82] H. Vinke, P.J. Hamersma, J.M.H. Fortuin, The enhancement of the gas-absorption rate in agitated slurry reactors due to the adhesion of gas-adsorbing particles to gas bubbles, Chem. Eng. Sci. 47 (1992) 3589–3596. doi:10.1016/0009-2509(92)85074-L.

[83] C.S. Ho, L. Ju, Effects of microorganisms on effective diffusion coefficients and solubilities in fermentation media, Biotechnol. Bioeng. 32 (1988) 313–325. doi:10.1002/bit.260320308.

[84] M. Kordač, V. Linek, Mechanism of enhanced gas absorption in presence of fine solid particles. Effect of molecular diffusivity on mass transfer coefficient in stirred cell, Chem. Eng. Sci. 61 (2006) 7125–7132. doi:10.1016/j.ces.2006.06.025.

[85] M. Rosu, A. Marlina, A. Kaya, A. Schumpe, Surfactant adsorption onto activated carbon and its effect on absorption with chemical reaction, Chem. Eng. Sci. 62 (2007) 7336–7343. doi:10.1016/j.ces.2007.08.027.

[86] V. Linek, M. Kordač, M. Soni, Mechanism of gas absorption enhancement in presence of fine solid particles in mechanically agitated gas-liquid dispersion. Effect of molecular diffusivity, Chem. Eng. Sci. 63 (2008) 5120–5128. doi:10.1016/j.ces.2008.06.023.

[87] M. Rosu, A. Schumpe, Influence of surfactants on gas absorption into aqueous suspensions of activated carbon, Chem. Eng. Sci. 62 (2007) 5458–5463. doi:10.1016/j.ces.2006.11.025.

[88] P.A. Ramachandran, Gas absorption in slurries containing fine particles: Review of models and recent advances, Ind. Eng. Chem. Res. 46 (2007) 3137–3152. doi:10.1021/ie060675w.

[89] A.A.C.M. Beenackers, W.P.M. van Swaaij, Mass transfer in gas-liquid slurry reactors, Chem. Eng. Sci. 48 (1993) 3109–3139. doi:10.1016/0009-2509(93)80199-Z.

[90] Y. Kawase, M. Moo-Young, Oxygen transfer in slurry bioreactors, Biotechnol. Bioeng. 37 (1991) 960–966. doi:10.1002/bit.260371010.

[91] Y. Kawase, M. Moo-Young, Liquid-phase mass transfer coefficient in slurry bubble column reactors: theory and experimental data in simulated fermentation media, Chem. Eng. Commun. 96 (1990) 177–192. doi:10.1080/00986449008911490.

[92] P.W.A.M. Wenmakers, J.A.A. Hoorn, J.A.M. Kuipers, N.G. Deen, Gas-liquid mass transfer enhancement by catalyst particles, a modelling study, Chem. Eng. Sci. 145 (2016) 233–244. doi:10.1016/j.ces.2016.01.043.

[93] R.D. Holstvoogd, W.P.M. van Swaaij, The influence of adsorption capacity on enhanced gas absorption in activated carbon slurries, Chem. Eng. Sci. 45 (1990) 151–162. doi:10.1016/0009-2509(90)87089-B.

[94] H. Vinke, P.J. Hamersma, J.M.H. Fortuin, Enhancement of the gas-absorption rate in agitated slurry reactors by gas-adsorbing particles adhering to gas bubbles, Chem. Eng. Sci. 48 (1993) 2197–2210. doi:10.1016/0009-2509(93)80237-K.

[95] H. Vinke, G. Bierman, P.J. Hamersma, J.M.H. Fortuin, Adhesion of small catalyst particles to gas bubbles: determination of small effective solid-liquid-gas contact angles, Chem. Eng. Sci. 46 (1991) 2497–2506. doi:10.1016/0009-2509(91)80043-X.

[96] O.J. Wimmers, J.M.H. Fortuin, The use of adhesion of catalyst particles to gas bubbles to achieve enhancement of gas absorption in slurry reactors-I. Investigation of particle-to-bubble adhesion using the bubble pick-up method, Chem. Eng. Sci. 43 (1988) 303–312. doi:10.1016/0009-2509(88)85042-5.

[97] O.J. Wimmers, J.M.H. Fortuin, The use of adhesion of catalyst particles to gas bubbles to achieve enhancement of gas absorption in slurry reactors - II. Determination of the enhancement in a bubble-containing slurry reactor, Chem. Eng. Sci. 43 (1988) 313–319. doi:10.1016/0009-2509(88)85043-7.

[98] M. Van der Zon, P.J. Hamersma, E.K. Poels, A. Bliek, Gas-solid adhesion and solid-solid agglomeration of carbon supported catalysts in three phase slurry reactors, Catal. Today. 48 (1999) 131–138. doi:10.1016/S0920-5861(98)00367-8.

[99] F. Omota, A.C. Dimian, A. Bliek, Adhesion of solid particles to gas bubbles. Part 1: Modelling, Chem. Eng. Sci. 61 (2006) 823–834. doi:10.1016/j.ces.2005.07.005.

[100] K.C. Ruthiya, J. Van Der Schaaf, B.F.M. Kuster, J.C. Schouten, Model to describe mass-transfer enhancement by catalyst particles adhering to a gas-liquid interface, Ind. Eng. Chem. Res. 44 (2005) 6123–6140. doi:10.1021/ie049167h.

[101] H.K. Versteeg, W. Malalasekera, An introduction to computational fluid dynamics: the finite volume method, 2nd ed., Pearson Education, Essex, England, 2007.

[102] D.A. Deglon, C.J. Meyer, CFD modelling of stirred tanks: Numerical considerations, Miner. Eng. 19 (2006) 1059–1068. doi:10.1016/j.mineng.2006.04.001.

[103] G.L. Lane, Improving the accuracy of CFD predictions of turbulence in a tank stirred by a hydrofoil impeller, Chem. Eng. Sci. 169 (2017) 188–211. doi:10.1016/j.ces.2017.03.061.

[104] G.L. Lane, M.P. Schwarz, G.M. Evans, Development of improved methods for computational modelling of gas dispersion in stirred tanks, in: 3rd Int. Conf. CFD Miner. Process Ind., Melbourne, Australia, 2003: pp. 281–286.

[105] J.B. Joshi, N.K. Nere, C. V. Rane, B.N. Murthy, C.S. Mathpati, A.W. Patwardhan, V. V. Ranade, CFD simulation of stirred tanks: Comparison of turbulence models (Part II: Axial flow impellers, multiple impellers and multiphase dispersions), Can. J. Chem. Eng. 89 (2011) 754–816. doi:10.1002/cjce.20465.

[106] Y. Liao, D. Lucas, A literature review of theoretical models for drop and bubble breakup in turbulent dispersions, Chem. Eng. Sci. 64 (2009) 3389–3406. doi:doi.org/10.1016/j.ces.2009.04.026.

[107] Y. Liao, D. Lucas, A literature review on mechanisms and models for the coalescence process of fluid particles, Chem. Eng. Sci. 65 (2010) 2851–2864. doi:10.1016/j.ces.2010.02.020.

[108] J.B. Joshi, K. Nandakumar, G.M. Evans, V.K. Pareek, M.M. Gumulya, M.J. Sathe, M.A. Khanwale, Bubble generated turbulence and direct numerical simulations, Chem. Eng. Sci. 157 (2017) 26–75. doi:10.1016/j.ces.2016.03.041.

[109] R. Rzehak, E. Krepper, CFD modeling of bubble-induced turbulence, Int. J. Multiph. Flow. 55 (2013) 138–155. doi:10.1016/j.ijmultiphaseflow.2013.04.007.

[110] G.L. Lane, M.P. Schwarz, G.M. Evans, Numerical modelling of gas–liquid flow in stirred tanks, Chem. Eng. Sci. 60 (2005) 2203–2214. doi:10.1016/j.ces.2004.11.046.

[111] F. Kerdouss, A. Bannari, P. Proulx, CFD modeling of gas dispersion and bubble size in a double turbine stirred tank, Chem. Eng. Sci. 61 (2006) 3313–3322. doi:10.1016/j.ces.2005.11.061.

[112] L. Lei, J. Ni, Three-dimensional three-phase model for simulation of hydrodynamics, oxygen mass transfer, carbon oxidation, nitrification and denitrification in an oxidation ditch, Water Res. 53 (2014) 200–214. doi:10.1016/j.watres.2014.01.021.

[113] H. Azargoshasb, S.M. Mousavi, O. Jamialahmadi, S.A. Shojaosadati, S.B. Mousavi, Experiments and a three-phase computational fluid dynamics (CFD) simulation coupled with population balance equations of a stirred tank bioreactor for high cell density cultivation, Can. J. Chem. Eng. 94 (2016) 20–32. doi:10.1002/cjce.22352.

[114] L. Yu, Y. Chao, P. Wensel, S. Chen, Hydrodynamic and kinetic study of cellulase production by Trichoderma reesei with pellet morphology, Biotechnol. Bioeng. 109 (2012) 1755–1768. doi:10.1002/bit.24433.

[115] P.T.L. Koh, M.P. Schwarz, CFD modelling of bubble-particle collision rates and efficiencies in a flotation cell, Miner. Eng. 16 (2003) 1055–1059. doi:10.1016/j.mineng.2003.05.005.

[116] G. Wang, L. Ge, S. Mitra, G.M. Evans, J.B. Joshi, S. Chen, A review of CFD modelling studies on the flotation process, Miner. Eng. 127 (2018) 153–177. doi:10.1016/j.mineng.2018.08.019.

[117] P. Moilanen, M. Laakkonen, O. Visuri, J. Aittamaa, Modeling local gas-liquid mass transfer in agitated viscous shear-thinning dispersions with CFD, Ind. Eng. Chem. Res. 46 (2007) 7289–7299. doi:10.1021/ie070566x.

[118] T. Wang, J. Wang, Numerical simulations of gas-liquid mass transfer in bubble columns with a CFD-PBM coupled model, Chem. Eng. Sci. 62 (2007) 7107–7118. doi:10.1016/j.ces.2007.08.033.

[119] T. Wang, J. Wang, Y. Jin, A CFD-PBM coupled model for gas-liquid flows, AIChE J. 52 (2006) 125–140. doi:10.1002/aic.10611.

[120] H. Zhang, A. Sayyar, Y. Wang, T. Wang, Generality of the CFD-PBM coupled model for bubble column simulation, Chem. Eng. Sci. 219 (2020). doi:10.1016/j.ces.2020.115514.

[121] R. Muñoz, A.J. Daugulis, M. Hernández, G. Quijano, Recent advances in two-phase partitioning bioreactors for the treatment of volatile organic compounds, Biotechnol. Adv. 30 (2012) 1707–1720. doi:10.1016/j.biotechadv.2012.08.009.

[122] J.L. Rols, G. Goma, Enhancement of oxygen transfer rates in fermentation using oxygen-vectors, Biotechnol. Adv. 7 (1989) 1–14. doi:10.1016/0734-9750(89)90900-2.

[123] G.K. Gakingo, T.M. Louw, K.G. Clarke, Modelling of the overall volumetric mass transfer coefficient measured by the dynamic method in gas-liquid-liquid systems, in: 13th Int. Conf. Heat Transf. Fluid Mech. Thermodyn., Portoroz, Slovenia, 2017: pp. 662–666.

[124] E. Dumont, Y. Andrès, Styrene absorption in water/silicone oil mixtures, Chem. Eng. J. 200–202 (2012) 81–90. doi:10.1016/j.cej.2012.06.028.

[125] E. Dumont, Y. Andrès, P. Le Cloirec, Mass transfer coefficients of styrene into water/silicone oil mixtures: New interpretation using the ‘equivalent absorption capacity’ concept, Chem. Eng. J. 237 (2014) 236–241. doi:10.1016/j.cej.2013.10.021.

[126] G. Quijano, R. Chávez-Avila, R. Muñoz, F. Thalasso, A. Ordaz, KLa measurement in two-phase partitioning bioreactors: new insights on potential errors at low power input, J. Chem. Technol. Biotechnol. 85 (2010) 1407–1412. doi:10.1002/jctb.2460.

[127] I.T.M. Hassan, C.W. Robinson, Oxygen transfer in mechanically agitated aqueous systems containing dispersed hydrocarbon, Biotechnol. Bioeng. 19 (1977) 661–682. doi:10.1002/bit.260190505.

[128] V. Linek, P. Beneš, A study of the mechanism of gas absorption into oil-water emulsions, Chem. Eng. Sci. 31 (1976) 1037–1046. doi:10.1016/0009-2509(76)87024-8.

[129] M.T. Cesário, W.A. Beverloo, J. Tramper, H.H. Beeftink, Enhancement of gas-liquid mass transfer rate of apolar pollutants in the biological waste gas treatment by a dispersed organic solvent, Enzyme Microb. Technol. 21 (1997) 578–588. doi:10.1016/S0141-0229(97)00069-0.

[130] J.L. Rols, J.S. Condoret, C. Fonade, G. Goma, Mechanism of enhanced oxygen transfer in fermentation using emulsified oxygen-vectors, Biotechnol. Bioeng. 35 (1990) 427–435. doi:10.1002/bit.260350410.

[131] E. Dumont, Y. Andrès, P. Le Cloirec, Effect of organic solvents on oxygen mass transfer in multiphase systems: Application to bioreactors in environmental protection, Biochem. Eng. J. 30 (2006) 245–252. doi:10.1016/j.bej.2006.05.003.

[132] T.H. Ngo, A. Schumpe, Oxygen absorption into stirred emulsions of n-alkanes, Int. J. Chem. Eng. 2012 (2012) 1–7. doi:10.1155/2012/265603.

[133] S.S. Alves, H.J.O. Pinho, Gas absorption in stirred gas-liquid-liquid systems: effect of transferred solute solubility and oil phase spreading characteristics, Chem. Eng. Commun. 200 (2013) 1425–1442. doi:10.1080/00986445.2012.751377.

[134] A. Kundu, E. Dumont, A.-M. Duquenne, H. Delmas, Mass transfer characteristics in gas-liquid-liquid system, Can. J. Chem. Eng. 81 (2003) 640–646. doi:10.1002/cjce.5450810341.

[135] E. Dumont, Y. Andrès, P. Le Cloirec, Mass transfer coefficients of styrene and oxygen into silicone oil emulsions in a bubble reactor, Chem. Eng. Sci. 61 (2006) 5612–5619. doi:10.1016/j.ces.2006.04.026.

[136] F. Yoshida, T. Yamane, Y. Miyamoto, Oxygen Absorption into Oil-in-Water Emulsions A Study on Hydrocarbon Fermentors, Ind. Eng. Chem. Process Des. Dev. 9 (1970) 570–577. doi:10.1021/i260036a013.

[137] J.D. Mcmillan, D.I.C. Wang, Mechanisms of oxygen transfer enhancement during submerged cultivation in perfluorochemical-in-water dispersions, Ann. N. Y. Acad. Sci. 589 (1990) 283–300. doi:10.1111/j.1749-6632.1990.tb24253.x.

[138] W.J. Bruining, G.E.H. Joosten, A.A.C.M. Beenackers, H. Hofman, Enhancement of gas-liquid mass transfer by a dispersed second liquid phase, Chem. Eng. Sci. 41 (1986) 1873–1877. doi:10.1016/0009-2509(86)87066-X.

[139] F. Laurenzi, M. Coroneo, G. Montante, A. Paglianti, F. Magelli, Experimental and computational analysis of immiscible liquid-liquid dispersions in stirred vessels, Chem. Eng. Res. Des. 87 (2009) 507–514. doi:10.1016/j.cherd.2008.12.007.

[140] F.J.E. Svensson, A. Rasmuson, PIV measurements in a liquid-liquid system at volume percentages up to 10% dispersed phase, Exp. Fluids. 41 (2006) 917–931. doi:10.1007/s00348-006-0211-0.

[141] F.J.E. Svensson, A. Rasmuson, LDA-measurements in a stirred tank with a liquid-liquid system at high volume percentage dispersed phase, Chem. Eng. Technol. 27 (2004) 335–339. doi:10.1002/ceat.200401981.

[142] R.A. Gore, C.T. Crowe, Effect of particle size on modulating turbulent intensity, Int. J. Multiph. Flow. 15 (1989) 279–285. doi:10.1016/0301-9322(89)90076-1.

[143] G. Hetsroni, Particles-turbulence interaction, Int. J. Multiph. Flow. 15 (1989) 735–746. doi:10.1016/0301-9322(89)90037-2.

[144] K. Hadinoto, E.N. Jones, C. Yurteri, J.S. Curtis, Reynolds number dependence of gas-phase turbulence in gas-particle flows, Int. J. Multiph. Flow. 31 (2005) 416–434. doi:10.1016/j.ijmultiphaseflow.2004.11.009.

[145] S. Balachandar, J.K. Eaton, Turbulent Dispersed Multiphase Flow, Annu. Rev. Fluid Mech. 42 (2010) 111–133. doi:10.1146/annurev.fluid.010908.165243.

[146] G. Montante, A. Paglianti, F. Magelli, Analysis of dilute solid-liquid suspensions in turbulent stirred tanks, Chem. Eng. Res. Des. 90 (2012) 1448–1456. doi:10.1016/j.cherd.2012.01.009.

[147] M. Colombo, M. Fairweather, Multiphase turbulence in bubbly flows: RANS simulations, Int. J. Multiph. Flow. 77 (2015) 222–243. doi:10.1016/j.ijmultiphaseflow.2015.09.003.

[148] C.J. Van Ede, R. Van Houten, A.A.C.M. Beenackers, Enhancement of gas to water mass transfer rates by a dispersed organic phase, Chem. Eng. Sci. 50 (1995) 2911–2922. doi:10.1016/0009-2509(95)00133-P.

[149] R.J. Littel, G.F. Versteeg, W.P.M. Van Swaaij, Physical absorption of CO2 and propene into toluene/water emulsions, AIChe J. 40 (1994) 1629–1638.

[150] A. Mehra, M.M. Sharma, Absorption with reaction: effect of emulsified second liquid phase, Chem. Eng. Sci. 40 (1985) 2382–2385. doi:10.1016/0009-2509(85)85144-7.

[151] A. Mehra, Intensification of multiphase reactions through the use of a microphase-I. Theoretical, Chem. Eng. Sci. 43 (1988) 899–912. doi:10.1016/0009-2509(88)80086-1.

[152] E. Nagy, A. Moser, Three-phase mass transfer: improved pseudo-homogeneous model, AIChE J. 41 (1995) 23–34. doi:10.1002/aic.690410104.

[153] H. Chawla, R. Khanna, K.D.P. Nigam, A.A. Adesina, A homogeneous model for mass transfer enhancement in gas-liquid-liquid systems, Chem. Eng. Commun. 195 (2008) 622–643. doi:10.1080/00986440701555431.

[154] H.J.O. Pinho, S.S. Alves, Semi-empirical modeling of gas–liquid mass transfer in gas–liquid–liquid systems in stirred tanks, Chem. Eng. Commun. 203 (2016) 94–102. doi:10.1080/00986445.2014.929575.

[155] G.D. Zhang, W.F. Cai, C.J. Xu, M. Zhou, A general enhancement factor model of the physical absorption of gases in multiphase systems, Chem. Eng. Sci. 61 (2006) 558–568. doi:10.1016/j.ces.2005.07.035.

[156] S. Jia, M. Wang, P. Kahar, Y. Park, M. Okabe, Enhancement of yeast fermentation by addition of oxygen vectors in air-lift bioreactor, J. Ferment. Bioeng. 84 (1997) 176–178. doi:10.1016/S0922-338X(97)82552-4.

[157] S. Jia, P. Li, Y.S. Park, M. Okabe, Enhanced oxygen transfer in tower bioreactor on addition of liquid hydrocarbons, J. Ferment. Bioeng. 82 (1996) 191–193. doi:10.1016/0922-338X(96)85049-5.

[158] J.D. McMillan, D.I.C. Wang, Enhanced oxygen transfer using oil-in-water dispersions, Ann. N. Y. Acad. Sci. 506 (1987) 569–582. doi:10.1111/j.1749-6632.1987.tb23851.x.

[159] J.L. Rols, G. Goma, Enhanced oxygen transfer rates in fermentation using soybean oil-in-water dispersions, Biotechnol. Lett. 13 (1991) 7–12. doi:10.1007/BF01033508.

[160] M. Hernández, G. Quijano, R. Muñoz, Key role of microbial characteristics on the performance of VOC biodegradation in two-liquid phase bioreactors, Environ. Sci. Technol. 46 (2012) 4059–4066. doi:10.1021/es204144c.

[161] F. Garcia-Ochoa, E. Gomez, Bioreactor scale-up and oxygen transfer rate in microbial processes: An overview, Biotechnol. Adv. 27 (2009) 153–176. doi:10.1016/j.biotechadv.2008.10.006.

[162] T. Yoshida, K. Yokoyama, K.-C. Chen, T. Sunouchi, H. Taguchi, Oxygen transfer in hydrocarbon fermentation by Candida rugosa, J. Ferment. Technol. 55 (1977) 76–83.

[163] M.T. Cesário, M. Turtoi, S.F.M. Sewalt, H.H. Beeftink, J. Tramper, Enhancement of the gas-to-water ethene transfer coefficient by a dispersed water-immiscible solvent: effect of the cells, Appl. Microbiol. Biotechnol. 46 (1996) 497–502. doi:10.1007/s002530050850.

[164] P.G. Hollis, K.G. Clarke, A systematic quantification and correlation of oxygen transfer coefficients and interfacial area in simulated model hydrocarbon-based bioprocesses in stirred tank reactors, J. Chem. Technol. Biotechnol. 91 (2016) 2720–2728. doi:10.1002/jctb.4897.

[165] A.I. Galaction, D. Cascaval, M. Turnea, E. Folescu, Enhancement of oxygen mass transfer in stirred bioreactors using oxygen-vectors 2. Propionibacterium shermanii broths, Bioprocess Biosyst. Eng. 27 (2005) 263–271. doi:10.1007/s00449-005-0416-2.

[166] D. Cascaval, A.I. Galaction, E. Folescu, M. Turnea, Comparative study on the effects of n-dodecane addition on oxygen transfer in stirred bioreactors for simulated, bacterial and yeasts broths, Biochem. Eng. J. 31 (2006) 56–66. doi:10.1016/j.bej.2006.05.019.

[167] V.M. Rajesh, V. V. Buwa, Volume-of-fluid simulations of gas-liquid-liquid flows in minichannels, Chem. Eng. J. 345 (2018) 688–705. doi:10.1016/j.cej.2018.01.050.

[168] A. Hoffmann, I. Ausner, J.U. Repke, G. Wozny, Detailed investigation of multiphase (gas-liquid and gas-liquid-liquid) flow behaviour on inclined plates, Chem. Eng. Res. Des. 84 (2006) 142–154. doi:10.1205/cherd.05110.

[169] S. Li, W. Duan, J. Chen, J. Wang, CFD simulation of gas-liquid-liquid three-phase flow in an annular centrifugal contactor, Ind. Eng. Chem. Res. 51 (2012) 11245–11253. doi:10.1021/ie300821t.

[170] D. Cheng, J. Cheng, X. Li, X. Wang, C. Yang, Z. Mao, Experimental study on gas-liquid-liquid macro-mixing in a stirred tank, Chem. Eng. Sci. 75 (2012) 256–266. doi:10.1016/j.ces.2012.03.035.

[171] D. Cheng, S. Wang, C. Yang, Z. Mao, Numerical simulation of turbulent flow and mixing in gas–liquid–liquid stirred tanks, Ind. Eng. Chem. Res. (2017) 13050–13063. doi:10.1021/acs.iecr.7b01327.

[172] H. Moradkhani, N.A. Kouchehbagh, M.-S. Izadkhah, Experimental and CFD–PBM approach coupled with a simplified dynamic analysis of mass transfer in phenol biodegradation in a three phase system of an aerated two‐phase partitioning bioreactor for environmental applications, Heat Mass Transf. 53 (2017) 1073–1091. doi:10.1007/s00231-016-1876-4.

[173] R.S. Juang, H.C. Kao, K.J. Tseng, Kinetics of phenol removal from saline solutions by solvent extraction coupled with degradation in a two-phase partitioning bioreactor, Sep. Purif. Technol. 71 (2010) 285–292. doi:10.1016/j.seppur.2009.12.008.

[174] V. Linek, V. Vacek, P. Benes, A critical review and experimental verification of the correct use of the dynamic method for the determination of oxygen transfer in aerated agitated vessels to water, electrolyte solutions and viscous liquids, Chem. Eng. J. 34 (1987) 11–34. doi:10.1016/0300-9467(87)85003-7.

[175] L. Ju, C.S. Ho, Oxygen diffusion coefficient and solubility in n-hexadecane, Biotechnol. Bioeng. 34 (1989) 1221–1224. doi:10.1002/bit.260340914.

[176] D. Lathouwers, Modelling and simulation of turbulent bubbly flow. Doctoral thesis, Delft University of Technology, The Netherlands, 1999.

[177] G.L. Lane, Computational modelling of gas-liquid flow in stirred tanks. Doctoral thesis, The University of Newcastle, Australia, 2006.

[178] P.R. Gogate, A.A.C.M. Beenackers, A.B. Pandit, Multiple-impeller systems with a special emphasis on bioreactors: A critical review, Biochem. Eng. J. 6 (2000) 109–144. doi:10.1016/S1369-703X(00)00081-4.

[179] H. Wu, G.K. Patterson, Laser-Doppler measurements of turbulent-flow parameters in a stirred mixer, Chem. Eng. Sci. 44 (1989) 2207–2221. doi:10.1016/0009-2509(89)85155-3.

[180] ANSYS Academic Research Mechanical and CFD, Release 17.2, Theory Guide, (2016).

[181] S.E. Elghobashi, T.W. Abou-Arab, A two-equation turbulence model for two phase flows, Phys. Fluids. 26 (1983) 931–938. doi:10.1063/1.864243.

[182] A. Behzadi, R.I. Issa, H. Rusche, Modelling of dispersed bubble and droplet flow at high phase fractions, Chem. Eng. Sci. 59 (2004) 759–770. doi:10.1016/j.ces.2003.11.018.

[183] S.M. Bhavaraju, T.W.F. Russell, H.W. Blanch, The design of gas sparged devices for viscous liquid systems, AIChE J. 24 (1978) 454–466. doi:10.1002/aic.690240310.

[184] M. Ishii, N. Zuber, Drag coefficient and relative velocity in bubbly, droplet or particulate flows, AIChE J. 25 (1979) 843–855. doi:10.1002/aic.690250513.

[185] A. Brucato, F. Grisafi, G. Montante, Particle drag coefficients in turbulent fluids, Chem. Eng. Sci. 53 (1998) 3295–3314. doi:10.1016/S0009-2509(98)00114-6.

[186] F. Magelli, D. Fajner, M. Nocentini, G. Pasquali, Solid distribution in vessels stirred with multiple impellers, Chem. Eng. Sci. 45 (1990) 615–625. doi:10.1016/0009-2509(90)87005-D.

[187] R.E.G. Poorte, A. Biesheuvel, Experiments on the motion of gas bubbles in turbulence generated by an active grid, J. Fluid Mech. 461 (2002) 127–154. doi:10.1017/S0022112002008273.

[188] D. Fajner, D. Pinelli, R.S. Ghadge, G. Montante, A. Paglianti, F. Magelli, Solids distribution and rising velocity of buoyant solid particles in a vessel stirred with multiple impellers, Chem. Eng. Sci. 63 (2008) 5876–5882. doi:10.1016/J.CES.2008.08.033.

[189] E. Doroodchi, G.M. Evans, M.P. Schwarz, G.L. Lane, N. Shah, A. Nguyen, Influence of turbulence intensity on particle drag coefficients, Chem. Eng. J. 135 (2008) 129–134. doi:10.1016/J.CEJ.2007.03.026.

[190] A. Bakker, Hydrodynamics of stirred gas liquid dispersions. Doctoral thesis, Delft University of Technology, The Netherlands, 1992.

[191] G.K. Gakingo, K.G. Clarke, T.M. Louw, A numerical investigation of the hydrodynamics and mass transfer in a three-phase gas-liquid-liquid stirred tank reactor, Biochem. Eng. J. 157 (2020). doi:10.1016/j.bej.2020.107522.

[192] A.A. Abufalgha, K.G. Clarke, R.W. Pott, The liquid–liquid homogeneity of a four-phase simulated hydrocarbon-based bioprocess in a bubble column reactor, J. Chem. Technol. Biotechnol. 94 (2019) 2034–2039. doi:10.1002/jctb.5989.

[193] G.K. Gakingo, K.G. Clarke, T.M. Louw, Hydrodynamics and oxygen transfer in a gas-liquid-liquid-solid stirred reactor: numerical modelling and investigation. Working paper, 2021.

[194] H. Rusche, R.I. Issa, The effect of voidage on the drag force on particles in dispersed two-phase flow, in: Japanese Eur. Two-Phase Flow Meet., Tsukuba, Japan, 2000.

[195] M. Simonnet, C. Gentric, E. Olmos, N. Midoux, Experimental determination of the drag coefficient in a swarm of bubbles, Chem. Eng. Sci. 62 (2007) 858–866. doi:10.1016/j.ces.2006.10.012.

[196] K. Tsuchiya, A. Furumoto, L.S. Fan, J. Zhang, Suspension viscosity and bubble rise velocity in liquid-solid fluidized beds, Chem. Eng. Sci. 52 (1997) 3053–3066. doi:10.1016/S0009-2509(97)00127-9.

[197] M. Laakkonen, P. Moilanen, V. Alopaeus, J. Aittamaa, Modelling local bubble size distributions in agitated vessels, Chem. Eng. Sci. 62 (2007) 721–740. doi:10.1016/j.ces.2006.10.006.

[198] V. V. Ranade, V.R. Deshpande, Gas-liquid flow in stirred reactors: Trailing vortices and gas accumulation behind impeller blades, Chem. Eng. Sci. 54 (1999) 2305–2315. doi:10.1016/S0009-2509(98)00301-7.

[199] C.L. Yaws, Transport properties of chemicals and hydrocarbons viscosity, thermal conductivity, and diffusivity of C_1 to C_{100} organics and Ac to Zr inorganics, Norwich, NY : William Andrew, Norwich, NY, 2009.

[200] C.L. Yaws, Thermophysical properties of chemicals and hydrocarbons, Norwich, NY : William Andrew, Norwich, NY, 2008.

[201] L. Nikiforaki, G. Montante, K.C. Lee, M. Yianneskis, On the origin, frequency and magnitude of macro-instabilities of the flows in stirred vessels, Chem. Eng. Sci. 58 (2003) 2937–2949. doi:10.1016/S0009-2509(03)00152-0.

[202] S.M. Kresta, V.T. Roussinova, Comments to "On the origin, frequency and magnitude of macro-instabilities of the flows in stirred vessels by Nikiforaki et al., Chem. Eng. Sci. 59 (2004) 951–953. doi:10.1016/j.ces.2003.12.006.

[203] M. Yianneskis, Reply to the Comments by Kresta to ‘On the origin, frequency and magnitude of macroinstabilities in stirred vessels’, Chem. Eng. Sci. 59 (2004) 955–956. doi:10.1016/j.ces.2003.12.007.

[204] A. Bakker, Modeling flow fields in stirred tanks. http://www.bakker.org/dartmouth06/engs199/07-flow.pdf (accessed 1 January 2017).

[205] HPC1 (Rhasatsha). http://www.sun.ac.za/hpc (accessed 29 April 2019).

[206] M. Coroneo, G. Montante, A. Paglianti, F. Magelli, CFD prediction of fluid flow and mixing in stirred tanks: Numerical issues about the RANS simulations, Comput. Chem. Eng. 35 (2011) 1959–1968. doi:10.1016/j.compchemeng.2010.12.007.

[207] C. Haringa, R. Vandewijer, R.F. Mudde, Inter-compartment interaction in multi-impeller mixing: Part I. Experiments and multiple reference frame CFD, Chem. Eng. Res. Des. 136 (2018) 870–885. doi:10.1016/j.cherd.2018.06.005.

[208] C. Haringa, R. Vandewijer, R.F. Mudde, Inter-compartment interaction in multi-impeller mixing. Part II. Experiments, sliding mesh and large Eddy simulations, Chem. Eng. Res. Des. 136 (2018) 886–899. doi:10.1016/j.cherd.2018.06.007.

[209] V.T. Roussinova, S.M. Kresta, R. Weetman, Resonant geometries for circulation pattern macroinstabilities in a stirred tank, Fluid Mech. Transp. Phenom. 50 (2004) 2986–3005. doi:10.1002/aic.10275.

[210] V. Roussinova, S.M. Kresta, R. Weetman, Low frequency macroinstabilities in a stirred tank: scale-up and prediction based on large eddy simulations, Chem. Eng. Sci. 58 (2003) 2297–2311. doi:10.1016/S0009-2509(03)00097-6.

[211] P.M. Armenante, G.M. Chang, Power consumption in agitated vessels provided with multiple-disk turbines, Ind. Eng. Chem. Res. 37 (1998) 284–291. doi:10.1021/ie970583u.

[212] W. Bujalski, A.W. Nienow, S. Chatwin, M. Cooke, The dependency on scale of power numbers of Rushton disc turbines, Chem. Eng. Sci. 42 (1987) 317–326. doi:10.1016/0009-2509(87)85061-3.

[213] M.M.C.G. Warmoeskerken, J.M. Smith, Flooding of disc turbines in gas-liquid dispersions: A new description of the phenomenon, Chem. Eng. Sci. 40 (1985) 2063–2071. doi:10.1016/0009-2509(85)87023-8.

[214] G.A. Hughmark, Power Requirements and Interfacial Area in Gas-Liquid Turbine Agitated Systems, Ind. Eng. Chem. Process Des. Dev. 19 (1980) 638–641. doi:10.1021/i260076a023.

[215] D. Cheng, X. Feng, J. Cheng, C. Yang, Numerical simulation of macro-mixing in liquid-liquid stirred tanks, Chem. Eng. Sci. 101 (2013) 272–282. doi:10.1016/j.ces.2013.06.026.

[216] R. Bubbico, S. Di Cave, B. Mazzarotta, Agitation power for solid-liquid suspensions containing large particles, Can. J. Chem. Eng. 76 (1998) 428–432. doi:10.1002/cjce.5450760312.

[217] Y. Zhao, X. Li, J. Cheng, C. Yang, Z.S. Mao, Experimental study on liquid-liquid macromixing in a stirred tank, Ind. Eng. Chem. Res. 50 (2011) 5952–5958. doi:10.1021/ie102270p.

[218] Z. Chen, S. Ata, G.J. Jameson, Behaviour of bubble clusters in a turbulent flotation cell, Powder Technol. 269 (2015) 337–344. doi:10.1016/j.powtec.2014.09.025.

[219] Z. Chen, S. Ata, G.J. Jameson, Breakup and re-formation of bubble clusters in a flotation cell, Miner. Eng. 71 (2015) 16–20. doi:10.1016/j.mineng.2014.11.002.

[220] S. Ata, G.J. Jameson, The formation of bubble clusters in flotation cells, Int. J. Miner. Process. 76 (2005) 123–139. doi:10.1016/j.minpro.2004.12.007.

[221] G. Wang, L. Ge, S. Mitra, G.M. Evans, J.B. Joshi, S. Chen, A review of CFD modelling studies on the flotation process, Miner. Eng. 127 (2018) 153–177. doi:10.1016/j.mineng.2018.08.019.

[222] M. Van Der Zon, H. Thoolen, P.J. Hamersma, E.K. Poels, A. Bliek, Agglomeration and adhesion of catalyst particles in gas-liquid reactors, Catal. Today. 66 (2001) 263–270. doi:10.1016/S0920-5861(00)00643-X.

[223] A.I. Galaction, D. Cascaval, C. Oniscu, M. Turnea, Prediction of oxygen mass transfer coefficients in stirred bioreactors for bacteria, yeasts and fungus broths, Biochem. Eng. J. 20 (2004) 85–94. doi:10.1016/j.bej.2004.02.005.

[224] M.W. Baltussen, L.J.H. Seelen, J.A.M. Kuipers, N.G. Deen, Direct Numerical Simulations of gas – liquid – solid three phase flows, Chem. Eng. Sci. 100 (2013) 293–299. doi:10.1016/j.ces.2013.02.052.

[225] M.W. Baltussen, J.A.M. Kuipers, N.G. Deen, Direct numerical simulation of effective drag in dense gas-liquid-solid three-phase flows, Chem. Eng. Sci. 158 (2017) 561–568. doi:10.1016/j.ces.2016.11.013.

[226] H. Li, R. Del Villar, C.O. Gomez, Reviewing the experimental procedure to determine the carrying capacity in flotation columns, Can. Metall. Q. 43 (2004) 513–520. doi:10.1179/cmq.2004.43.4.513.

[227] P.T.L. Koh, M.P. Schwarz, CFD model of a self-aerating flotation cell, Int. J. Miner. Process. 85 (2007) 16–24. doi:10.1016/j.minpro.2007.08.006.